SEARS FOUNDATION FOR MARINE RESEARCH
BINGHAM OCEANOGRAPHIC LABORATORY, YALE UNIVERSITY

JOURNAL OF
MARINE RESEARCH

VOLUME 16 1958 NUMBER 2

EFFECTS OF A NONRIGID, IMPERMEABLE BOTTOM ON PLANE SURFACE WAVES IN SHALLOW WATER[1]

By

HERMAN G. GADE[2]

ABSTRACT

Mutual effects of progressive wave motion in shallow water and in underlaying uid sediments are discussed, with emphasis on modification of the surface wave. The mathematical model is a layer of inviscid fluid overlaying a viscous fluid of greater ensity and bounded by a horizontal rigid plane. Solutions for locally periodic, imple harmonic disturbances indicate that wave height decays exponentially with ravelled distance. It is found that the rate of decay has a maximum value when the imensionless parameter $h_0 \sqrt{\sigma/2\nu}$ has a value of 1.2, σ being the angular frequency, the viscosity, and h_0 the thickness of the lower layer.

The rate of dissipation of energy in the lower layer is found to be proportional to (a) he wave energy, (b) the ratio of amplitudes at the interface and the surface, and (c) he sine of an angle closely related to the phase difference between profiles at the free urface and the interface. Comparison is made between typical values of wave decay ue to dissipation in a fluid bottom and that due to friction loss over a rigid sand ottom. Even in a relatively thin layer of mud the dissipation exceeds by far the nergy loss due to bottom friction.

LIST OF SYMBOLS

A	amplitude of surface wave at reference point, $x = 0$
B, C, D	complex factors
D_f	dissipated energy per unit area and unit time by friction over a rigid bottom

[1] Research performed at Dept. of Oceanography, Texas A & M College, College tation.

[2] Oceanografisk Institutt, University of Oslo.

E	total wave energy in water per unit area
$\mathfrak{F}, f$	function symbols
G, G_0	wave height, generally, and at reference point
$\mathcal{G}$	function symbol
g	force of gravity per unit mass
H, H_0	distance from surface to interface, generally, and a still water conditions
h, h_0	instantaneous, and equilibrium distances from interfac to rigid bottom
i	$\sqrt{-1}$
K_f	friction coefficient for rigid bottom
k	complex coefficient $k_r + k_i i$
k_r	wave number
k_i	decay coefficient
L	wave length
M_1, M_2, m	complex constants
P	magnitude of complex function $iZ(z)\ \sigma/\nu$
p, p_a, p_h	pressure, atmospheric pressure, pressure at interfac under equilibrium conditions
R	magnitude of complex function
S	magnitude of complex function C/A
T	period of wave
t	time
U	magnitude of complex function
u	horizontal particle velocity
W	work
x	horizontal coordinate
Z	complex function of z
z	vertical coordinate
β	angle, argument of $iZ(z)\ \sigma/\nu$
Γ	complex function of $h_0\sqrt{\sigma/2\nu}$
γ	$1 - \rho_1/\rho_2$
η_1, η_2	amplitudes on upper and lower layer, respectively
θ	angle, argument of $(1 - H_0 gRe^{i\phi})$
ϕ	angle, argument of $(k/\sigma)^2$
ρ	density
σ	$2\pi/T$
ν	viscosity of lower layer
ξ	horizontal displacement
ϕ'	angle, argument of C
ϕ''	angle, $\phi/2 + \theta + \beta$

Index 1 refers to upper layer, index 2 to the lower layer.

INTRODUCTION

It has been reported (Ewing and Press, 1949) that a kind of wave motion in soft sediments is likely to occur under intermediate and shallow water conditions. These soft sediments can be classified as clay or mud. No qualitative measurements of this motion have been made, consequently our knowledge of the phenomenon to date has been inadequate.

Since most clays can be regarded as practically impermeable to water, considering the time of a wave period, there is likely to be little, if any, dissipation of energy due to percolation. However, there can be dissipation of energy due to internal friction in the sediment.

The effect of a nonrigid bottom on pressure and on particle velocities in the water has been discussed by several authors. Seiwell (1947) related computed wave heights to measured heights at Bermuda, assuming the bottom rigid; he found that the ratio of computed to observed wave heights was too high by a factor between 1.18 and 1.35 for 8 to 9 second waves. Ewing and Press (1949) suggest that this discrepancy may be due to a liquid bottom; they applied a theory given by Lamb (1932), treating the bottom as a perfect nonviscous fluid. The Seiwell effect, as we may call it, was actually less than the effect computed by Ewing and Press; this may be explained qualitatively by taking the viscosity of the sediments into account.

There are evidently two possible ways in which the nonrigid bottom can participate in wave motion. One is an elastic deformation which may have a fairly deep penetration in the sediment; this is by far the most common. The other is a motion in which the sediment behaves like a viscous fluid; the penetration of this motion does not have to be deeper than a few inches, although it may also extend several feet down in the soft mud. Among the few examples of such motion, the Mud Hole located near shore at about 92° 30′ W on the Louisiana coast is well known. Here the fluid bottom has such a pronounced calming effect on the sea in rough weather that the local fishing boats use it as an emergency harbor.

The present paper is an attempt to discuss the effects of a nonrigid bottom of the latter type discussed above. The author has limited himself to the case of relatively shallow water, *i.e.*, $H/L \leq 1/20$, where H is the depth of water, L the wave length.

PART I. THEORY

1. *Bottom Conditions.* Bottom conditions vary from place to plac in regions where sediments have the character of a viscous fluid; the depend also upon the state of the sea and are therefore subject to varia tions with time. In some places we find only a thin layer (less tha six inches deep) of fluid sediment on top of relatively hard deposits in other places the soft sediments extend many feet down, usually wit the viscosity apparently increasing with depth. Sometimes sediment have a fairly constant coefficient of viscosity in the upper few feet below which a slow increase in viscosity may occur until the sedimen no longer has the character of a fluid with respect to the period an dimensions of an ordinary surface wave. The viscosity will also de pend upon the velocity gradient in the sediment; especially, it is found that when the sediment is at rest, the forces needed to cause a dis turbance have to exceed a certain threshold value. The effect of thi characteristic threshold value for initiation of motion will be such tha at some depth in the sediments the pressure forces will not be sufficien to cause any motion. The resulting effect is the same as if we had a rigid bottom at this depth. In the case of a continuously varyin coefficient of viscosity, we should have the same situation: a layer o fluid sediment overlaying an apparently rigid bottom.

As typical of the quantitative values of viscosity of bottom sedi ments, we may cite measurements done on top layer sediments outsid the Mississippi Delta which showed kinematical coefficients o $1 < \nu < 10$ ft^2/sec, with densities (specific gravity) of $1.6 < \rho < 2.0$

2. *A Mathematical Model.* In the case of a nonrigid bottom, th shallow water criterium has to be modified to $H'/L \leq 1/20$, where H denotes the effective depth: *i.e.*, the depth of water necessary to brin about the same wave length over a rigid bottom as is observed in th case of a nonrigid bottom when the period remains fixed. The effec tive depth is equal to the actual depth in the case of a rigid bottom but it will be somewhat larger when the bottom is fluid.

For simplicity we choose as a mathematical model a two-layer systen subject to a long-wave disturbance; the upper layer will be treated a frictionless while the lower layer is assumed to be homogeneous and o finite thickness, resting on a rigid horizontal strata *at which no motio exists.* The lower layer, representing the sediment, is not capable o supporting a shear stress while at rest. In addition, the followin assumptions will be employed:

a. The wave is of sinusoidal form;
b. Disturbance of the *upper* fluid is not associated with any driv ing or dissipative shearing forces;

c. Motions of both fluids are incapable of divergence;
d. Only plane waves are considered;
e. Variations of surface pressure are neglected;
f. The mean current is assumed to be nil;
g. The wave amplitude is considered small compared with depth;
h. The fluid layers are considered to be of infinite horizontal extent; geostrophic acceleration and curvature of the earth are neglected.
i. Vertical accelerations are neglected.

Furthermore, we shall consider only periodic disturbances, *i.e.*, those in which wave height varies periodically at a fixed point but decays with distance in the directions of propagation such that the distribution of wave heights is steady.

3. *Analysis.* For equations expressing continuity of mass and momentum for the upper fluid, we shall adopt:

$$\frac{\partial u_1}{\partial t} + g\frac{\partial (h + H)}{\partial x} = 0, \tag{I-1}$$

$$\frac{\partial H}{\partial t} + H_0\frac{\partial u_1}{\partial x} = 0; \tag{I-2}$$

here u_1, horizontal velocity in the direction of the x-coordinate, is presumed independent of depth; H and h are distance from interface to surface and from rigid bottom to interface respectively; z is the vertical coordinate measured positive from the rigid bottom toward the surface; and t denotes time. The quantities h_0 and H_0 are the thicknesses of the two layers under equilibrium conditions.

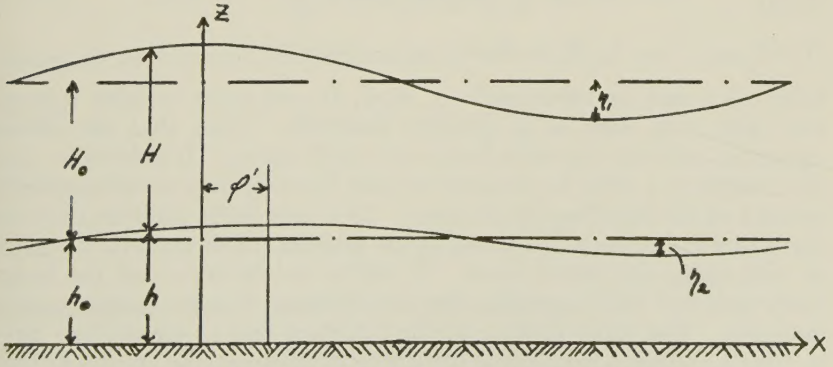

Figure 1. Schematic presentation of the wave and various parameters.

For the lower fluid the equations of motion and continuity are as follows:

$$\frac{\partial u_2}{\partial t} + \gamma g \frac{\partial h}{\partial x} + (1 - \gamma) g \frac{\partial (h + H)}{\partial x} = \nu \frac{\partial^2 u_2}{\partial z^2} \tag{I-3}$$

$$\int_0^h \frac{\partial u_2}{\partial x} dz + \frac{\partial h}{\partial t} = 0. \tag{I-4}$$

Here the horizontal velocity u_2 is dependent on x, z, and t. The parameter γg, the apparent force of gravity per unit mass, is related to the force of gravity g, as follows:

$$\gamma g = \frac{\rho_2 - \rho_1}{\rho_2} g, \tag{I-5}$$

where ρ_1 and ρ_2 are the densities of the upper and lower layers respectively. The boundary conditions adopted are:

$$u_1, u_2, H - H_0, h - h_0, \rightarrow 0 \text{ as } x \rightarrow \infty, \tag{I-6}$$

$$h + H = h_0 + H_0 + A \cos \sigma t \text{ at } x = 0, \tag{I-7}$$

$$u_2 = 0 \text{ at } z = 0, \tag{I-8}$$

$$\frac{\partial u_2}{\partial z} = 0 \text{ at } z = h_0 \ . \tag{I-9}$$

We shall try solutions of the following forms:

$$h + H = h_0 + H_0 + Ae^{i(kx - \sigma t)} \tag{I-10}$$

$$u_1 = Be^{i(kx - \sigma t)}, \tag{I-11}$$

$$h = h_0 + Ce^{i(kx - \sigma t)}, \tag{I-12}$$

$$u_2 = D\, Z(z) e^{i(kx - \sigma t)}, \tag{I-13}$$

$$H = H_0 + (A - C) e^{i(kx - \sigma t)}. \tag{I-14}$$

Here σ is a real quantity, while A, B, C, D, and k are complex quantities; $Z(z)$ may also be a complex function. Note that the above equations indicate the same k and σ for both layers. It is obvious that the frequency σ must be common to both layers if they are to remain in contact at the interface at all times. It is also fairly obvious that the wave length (expressed in terms of the real part of k) must be the same in both upper and lower layer. It will be shown later that the imaginary part of k will determine the rate of decay of wave heights versus distance. The wave heights at the interface and at the surface have to bear a constant ratio since our differential equations are linear (Assumption g). It follows that rates of decay in the upper and lower layer have to be the same in order to give a constant ratio for wave heights at the interface and at the surface.

Equation (I-1) is satisfied provided that

$$B = g\frac{k}{\sigma}A. \tag{I-15}$$

Equation (I-2) is satisfied if $kBH_0 + (C - A)\sigma = 0$ or by using (I-15)

$$\left[H_0\left(\frac{k}{\sigma}\right)^2 g - 1\right]A + C = 0. \tag{I-16}$$

From (I-3) we find that $Z(z)$ must satisfy the following condition:

$$\begin{aligned} D[\nu Z''(z) + i\sigma Z(z)] &= igk[\gamma C + (1 - \gamma)A] \\ &= igk\left[1 - \gamma H_0\left(\frac{k}{\sigma}\right)^2 g\right]A; \end{aligned} \tag{I-17}$$

here $Z''(z)$ is the second derivative with respect to z of the function $Z(z)$. The constant D can be chosen arbitrarily. For convenience, let

$$D = ig\frac{k}{\sigma}\frac{\sigma}{\nu}\left[1 - \gamma g H_0\left(\frac{k}{\sigma}\right)^2\right]A; \tag{I-18}$$

then from (I-17)

$$Z''(z) + i\frac{\sigma}{\nu}Z(z) = 1, \tag{I-19}$$

of which a solution is

$$Z(z) = -i\frac{\nu}{\sigma} + M_1 \cosh mz + M_2 \sinh mz, \tag{I-20}$$

where M_1 and M_2 are two constants to be evaluated and where

$$m = (1 - i)\sqrt{\frac{\sigma}{2\nu}}. \tag{I-21}$$

From (I-8),

$$D\left[\frac{\nu}{i\sigma} + M_1\right] = 0, \text{whence } M_1 = i\frac{\nu}{\sigma} \tag{I-22}$$

(except for the trivial solution $D = 0$), and from (I-9)

$$M_2 = -M_1 \tanh mh_0 . \tag{I-23}$$

Inserting the results in (I-20), we have:

$$Z(z) = -i\frac{\nu}{\sigma}[1 + \tanh mh_0 \sinh mz - \cosh mz]. \tag{I-24}$$

Finally, equation (I-4) will be satisfied provided that

$$\int_0^h Z(z)\, dz = \frac{C}{D}\frac{\sigma}{k},$$

which leads to the following quartic equation in the parameter k:

$$\text{(I-25)} \qquad 1 - \frac{\tanh mh_0}{mh_0} = \frac{1}{gh_0(k/\sigma)^2}\left\{\frac{1 - gH_0(k/\sigma)^2}{1 - gH_0(k/\sigma)^2}\right\}.$$

Now it is necessary to solve for (k/σ); formally we must have $k/\sigma = (h_0, H_0, \gamma, \nu, \sigma)$, which is our complex Hamilton function.

Equation (I-25) is biquadratic in k/σ, hence there are four different Hamiltonian functions which are roots of (I-25). These are

$$\text{(I-26)} \quad \frac{k}{\sigma} = \pm\left\{\frac{(H_0 + \Gamma h_0) \pm \sqrt{(H_0 + \Gamma h_0)^2 - 4\gamma\Gamma H_0 h_0}}{2\gamma g H_0 \Gamma h_0}\right\}^{\frac{1}{2}},$$

where $\Gamma = 1 - \dfrac{\tanh mh_0}{mh_0}$ (complex function of $\sigma h_0^2/\nu$).

We are interested in only the positive solution of k/σ which contains the reciprocal of the wave velocity; negative values of k/σ indicate waves travelling in the opposite direction. We still have a choice between the signs of the square root. Those familiar with internal wave theory will recognize that use of the positive sign gives a solution with the larger amplitudes at the interface while the negative sign gives us one which has the larger amplitudes at the surface. This is merely the ordinary surface wave, the effects of which extend down to the interface and cause a smaller disturbance in the lower layer. It is this part of the solution in which we are interested, so far as the present analysis is concerned.

Multiplication of (I-26) by $H_0 g$ renders it in the following convenient form:

$$\text{(I-27)} \quad \left(\frac{k}{\sigma}\right)^2 H_0 g = \frac{(1 + \Gamma h_0/H_0) - \sqrt{(1 - \Gamma h_0/H_0)^2 - 4\gamma\Gamma h_0/H_0}}{2\gamma\Gamma h_0/H_0}.$$

This solution is in a dimensionless form from which $(k/\sigma)^2 H_0 g$ can be interpreted as a function of the dimensionless parameters γ and $\Gamma h_0/H_0$; *i.e.*,

$$\text{(I-28)} \qquad \left(\frac{k}{\sigma}\right)^2 H_0 g = f\left(\Gamma\frac{h_0}{H_0}, \gamma\right).$$

However, a detailed discussion of this form is not feasible since $\Gamma h_0/H_0$ is a complex function of the dimensionless parameters $h_0\sqrt{\sigma/2\nu}$ and

h_0/H_0. The first of these represents an effective Reynolds number for the disturbance. Thus, in terms of real arguments we can write

$$\left(\frac{k}{\sigma}\right)^2 H_0 g = \mathcal{G}\left(\sqrt{\frac{\sigma}{2\nu}}\, h_0, \frac{h_0}{H_0}, \gamma\right) \tag{I-29}$$

or

$$\left(\frac{k}{\sigma}\right)^2 H_0 g = \mathcal{F}\left(\sqrt{\frac{\sigma}{2\nu}}\, h_0, \sqrt{\frac{\sigma}{2\nu}}\, H_0, \gamma\right), \tag{I-30}$$

where $\mathcal{G}$ and $\mathcal{F}$ are complex functions of the real arguments indicated.

In the following discussion and in all the figures, the following values have been adopted as applicable to a wave of 8 seconds period:

$$\sigma = 2\pi/8 \text{ sec}^{-1},\ \nu = 5 \text{ ft}^2 \text{ sec}^{-1},\ H_0 = 4 \text{ feet, and } \gamma = 0.4287.$$

Since the whole discussion is based upon shallow water, we shall be concerned only with values of h_0 less than 6 feet, because the *effective* depth for values of h_0 larger than 6 feet becomes larger than 1/20 of the wave length. This limit gives for the corresponding dimensionless parameter $\sqrt{\sigma/2}\, h_0 < 1.6815$.

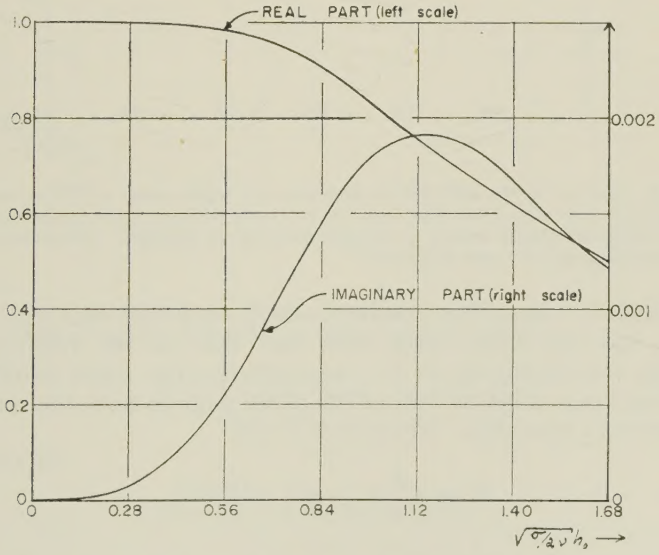

Figure 2. Real and imaginary parts of the dimensionless parameter $(k/\sigma)^2 H_0 g$ versus $\sqrt{\sigma/2\nu}\, h_0$. $(k/\sigma)^2 g H_0$ is the square of the ratio between the phase velocity of the pure water and the complex phase velocity of the water-sediment wave; $\sqrt{\sigma/2\nu}\, h_0$ represents an effective Reynolds number for the disturbance of the sediment.

The curves in Fig. 2 give the real and imaginary parts of $(k/\sigma)^2 H_0 g$ as functions of $\sqrt{\sigma/2\nu}\, h_0$ or h_0, as calculated from equation (I-27). The curves in Figs. 3 and 4 show the calculated real and imaginary parts of $k/\sigma \sqrt{H_0 g}$ respectively. The outstanding feature of these figures is the maximum value of the imaginary part of k, which controls the role of decay of wave amplitude.

In order to evaluate numerically the results pertinent to solutions given by (I-10) through (I-14), we must determine the coefficients A,

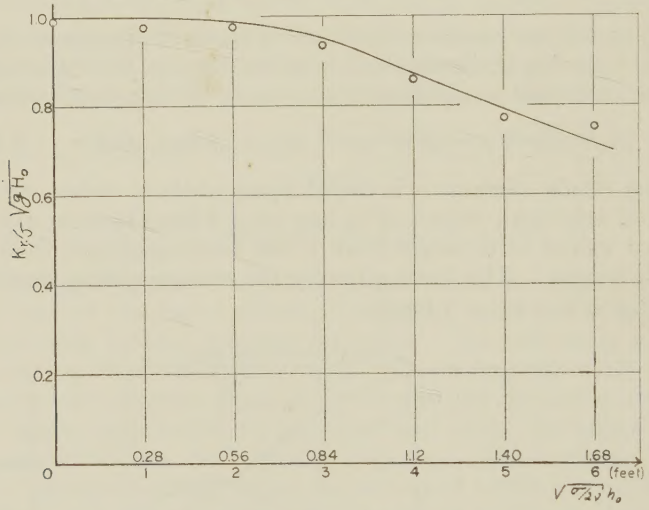

Figure 3. Real part of the dimensionless parameter $k/\sigma \sqrt{gH_0}$ versus $\sqrt{\sigma/2\nu}\, h_0$ and h_0 in feet. $k/\sigma \sqrt{gH_0}$ is the ratio of the phase velocities of the pure water to that of the composite water-sediment wave; $\sqrt{\sigma/2\nu}\, h_0$ is Reynolds number for the disturbance of the sediment. The circled points show results from a separate wave tank experiment.

B, C, and D. Boundary-condition (I-7) says that our wave at the surface has the phase angle zero and that at the reference point ($x = 0$) the amplitude is A. Accordingly, the wave amplitude in (I-10) has been called A. Since the phase angle is zero, the constant A is a pure real quantity. Then from (I-15)

$$B = g\frac{k}{\sigma}A = gA\sqrt{R}e^{i\varphi/2}, \tag{I-31}$$

where

$$Re^{i\varphi} = \left(\frac{k}{\sigma}\right)^2; \tag{I-32}$$

here R is the modulus of the complex quantity and φ its argument. It is also convenient to bring the coefficients C and D [(I-16) and (I-17)] to a polar form. Let

$$C = (1 - H_0 gRe^{i\varphi})\, A = SAe^{i\varphi'}, \tag{I-33}$$

where SA is the modulus of this complex quantity and φ' its argument; and let

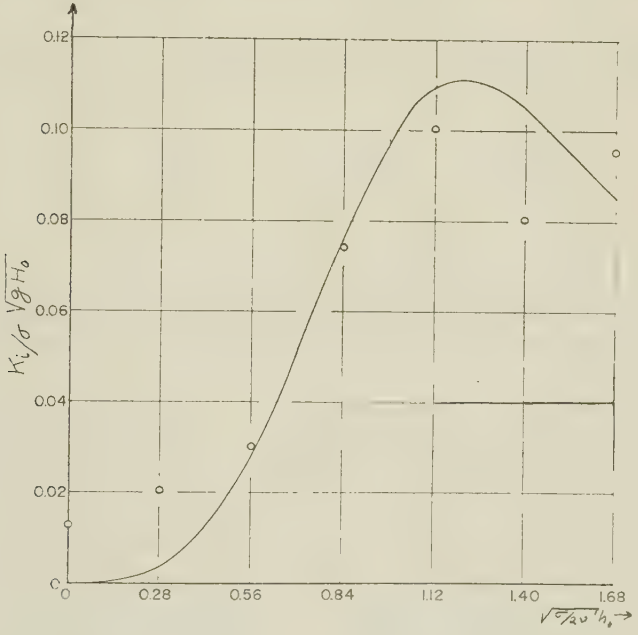

Figure 4. Imaginary part of the dimensionless parameter $k/\sigma\sqrt{gH_0}$ versus the Reynolds number $\sqrt{\sigma/2\nu}\,h_0$. The circled points are results from a separate wave tank experiment.

$$D = ig\frac{\sigma}{\nu} A \sqrt{R}e^{i\varphi/2}(1 - \gamma gH_0 Re^{i\varphi}) \tag{I-34}$$

be written as

$$D = ig\frac{\sigma}{\nu} A \sqrt{R}Ue^{i(\varphi/2+\theta)}, \tag{I-34b}$$

where U is the modulus and θ the argument of the complex quantity $(1 - \gamma gH_0 Re^{i\varphi})$ in (I-34).

From now on we shall use the more instructive form of the complex quantity k where its real (index r) and imaginary (index i) parts are

separated: $k = k_r + ik_i$. Equations (I-10) through (I-13) will then take the forms:

$$h + H = h_0 + H_0 + Ae^{i(k_r x - \sigma t)} e^{-k_i x}, \tag{I-35}$$

$$u_1 = gA\sqrt{R} e^{i(k_r x - \sigma t + \varphi/2)} e^{-k_i x}, \tag{I-36}$$

$$h = h_0 + SAe^{i(k_r x - \sigma t + \varphi')} e^{-k_i x}, \tag{I-37}$$

$$u_2 = gA\sqrt{R} UPe^{i(k_r x - \sigma t + \varphi'')} e^{-k_i x}, \tag{I-38}$$

where we have introduced the real quantities P and β defined by the complex equation:

$$Pe^{i\beta} = i\frac{\sigma}{\nu} Z(z) = 1 + \tanh mh_0 \sinh mz - \cosh mz \tag{I-39}$$

and

$$\varphi'' = \varphi/2 + \theta + \beta. \tag{I-40}$$

Now, both the real and the imaginary parts of these solutions will satisfy the differential equations and the boundary conditions. In order to get a cosine wave profile for the free surface, we must choose the real parts.

4. *General Discussion Of The Solutions.* Solutions (I-34) through (I-37) for the surface displacements and particle velocities are all characterized by the exponential factor $e^{-k_i x}$. For a positive value of k_r, k_i will always be positive. The size of the exponential factor is discussed in Part II. The most outstanding features are the different phase angles. From (I-36), velocities in the upper fluid are out of phase by an angle $+ \varphi/2$ relative to the surface profile, which means that the wave crest is preceding the maximum velocity by the angle $\varphi/2$!

The wave profile of the interface (I-37) is displaced by the angle φ' in relation to the surface profile. This angle is always negative since

$$\tan \varphi' = \frac{-H_0 gR \sin \varphi}{1 - gH_0 R \cos \varphi}, \tag{I-41}$$

where $\varphi' \gtrless \pi/2$ and $gH_0 R \gtrless 1$; the only choice is $|\varphi| < \pi/2$. The last condition means that there is always an energy transport from the upper to the lower layer.[3] The curve in Fig. 5 shows φ' versus $\sqrt{\sigma/2\nu}\, h_0$.

The phase situation in the lower layer, regarding the horizontal

[3] Discussed in Part II.

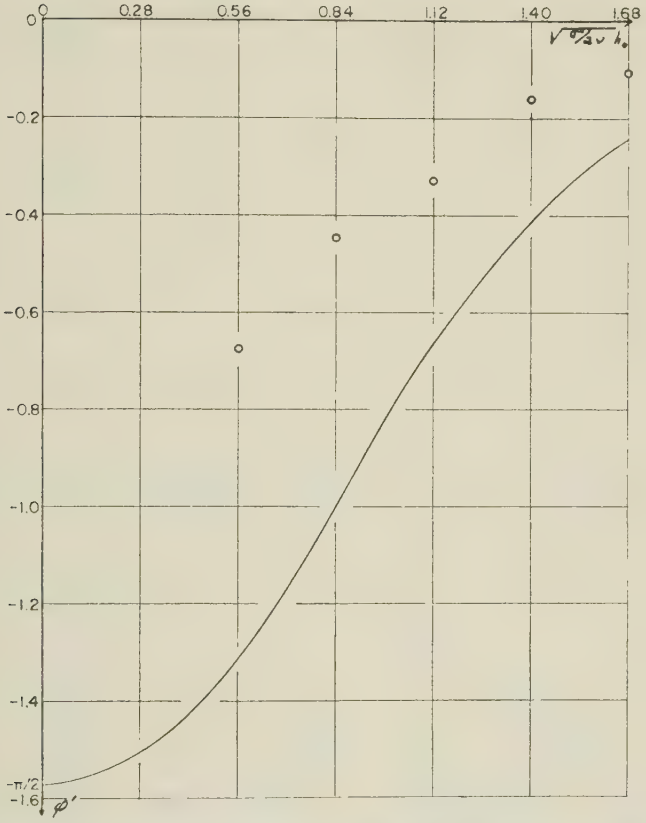

Figure 5. Theoretically determined values of the phase displacement φ' of the interface profile to the surface profile versus the Reynolds number $\sqrt{\sigma/2\nu}\, h_0$. The circled points are results from a separate wave tank experiment.

velocities, is of a rather complicated nature. The behavior of φ'' depends on the three angles $\varphi/2$, θ, and β. The first two are functions of $\sqrt{\sigma/2\nu}\, h_0$ only, while β is also a function of z. The angle θ is given by [see (I-34)]

$$\tan\theta = \frac{-\gamma g H_0 R \sin\varphi}{1 - \gamma g H_0 R \cos\varphi}. \tag{I-42}$$

The same arguments as those used for φ' can be applied to θ to show that this also is always negative (γ is less than unity).

Though not immediately apparent, it can be shown that the angle β is always negative and that its magnitude increases to a finite limit as z

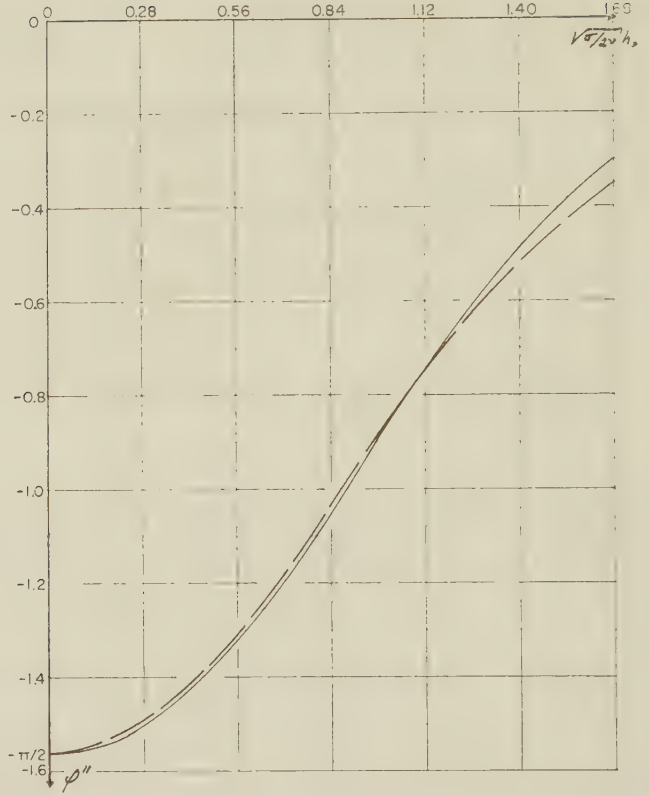

Figure 6. The smooth curve shows that φ'', the phase displacement of the velocity in the lower laye for $z = h_0$ in relation to the surface profile, is primarily dominated by β, defined by (I-39), as shown b the dashed curve.

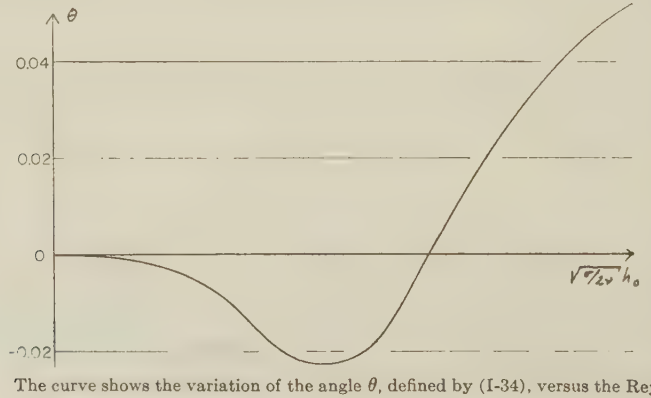

Figure 7. The curve shows the variation of the angle θ, defined by (I-34), versus the Reynolds num ber $\sqrt{\sigma/2\nu}\,h_0$. Angles in radians.

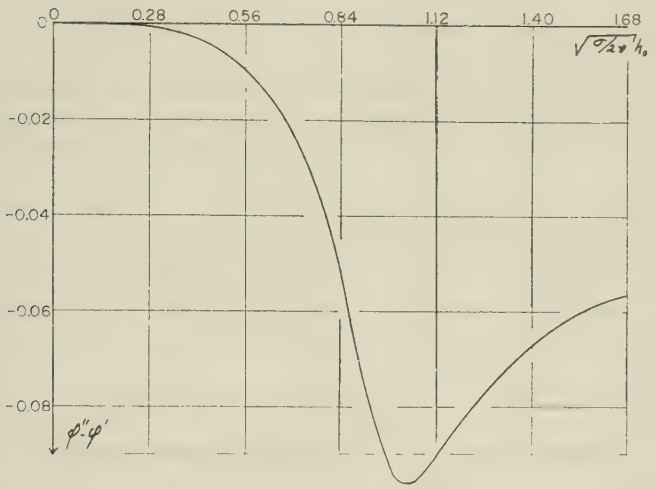

Figure 8. The curve shows the phase displacement of the velocity in the lower layer for $z = h_0$ in relation to the profile at the interface versus Reynolds number $\sqrt{\sigma/2\nu}\,h_0$. Angles in radians.

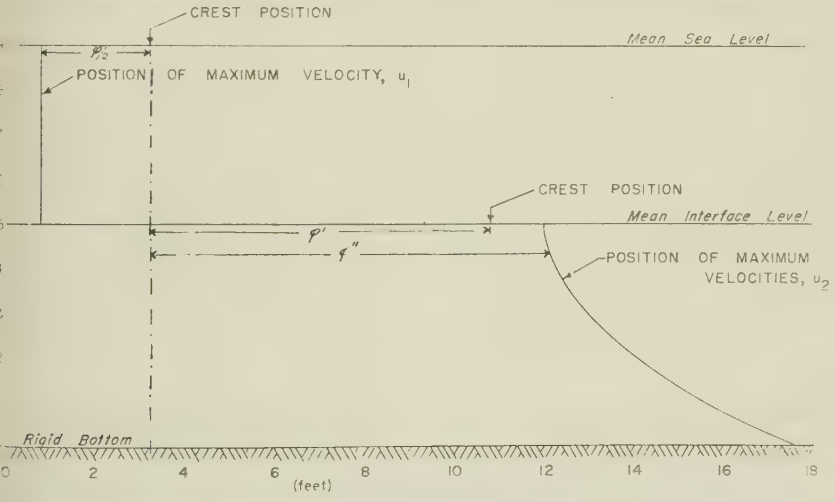

Figure 9. The figure presents the various phase angles in a schematic form showing their relative size when the Reynolds number = 1.4. ($h_0 = 5$ feet)

goes to zero. $\beta_{z=h_0}$ is shown in Fig. 6, the typical behavior of $\theta + \varphi/2$ in Fig. 7. The phase angle $\varphi''_{z=h_0}$ is primarily dominated by $\beta_{z=h_0}$ as is seen in Fig. 6, where the smooth and dashed curves represent $\varphi''_{z=h_0}$ and $\beta_{z=h_0}$ respectively. Calculation has shown that $\varphi''_{z=h_0}$ is always negative and greater than φ' in magnitude. An interesting minimum value for $(\varphi'' - \varphi')$ was found at $\sqrt{\sigma/2\nu'}\,h_0 \doteq 1$, as shown in Fig. 8.

This means that the wave form, while at the surface, is preceding the maximum velocity, whereas in the lower layer it will be lagging. Thus, relative to maximum velocities, the resulting effect is a phase shift of the wave profiles towards each other. A picture of the situation where $\sqrt{\sigma/2\nu}\, h_0 = 1.4$ ($h_0 = 5$ feet) is shown in Fig. 9.

5. *Horizontal Velocities And Displacements.* The horizontal velocities are expressed by (I-36) and (I-38). However, we are more interested in the ratio of velocities in the upper and the lower layer than in their absolute values. Thus the ratio between the velocity at any

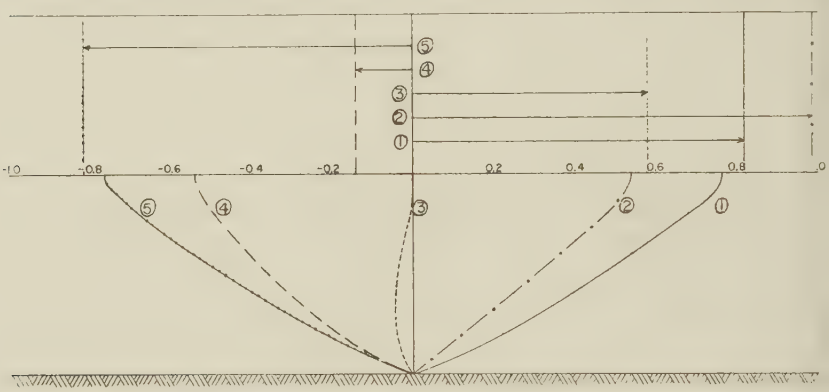

Figure 10. The curves in the lower layer and the corresponding vertical lines in the upper layer represent the velocity profiles for values of $(\varphi'' - \sigma t) = 0, \pi/4, \pi/2, 3\pi/4, \pi$, numbered 1, 2, 3, 4, 5, respectively. The example refers to a thickness of the lower layer of 5 feet, or $\sqrt{\sigma/2\nu}\, h_0 = 1.4$.

point in the lower layer and the velocity in the upper layer for the same abscissa, at the same time, is

$$P\sqrt{(1 - \gamma g H_0 R \cos\varphi)^2 + (\gamma g H_0 R \sin\varphi)^2}\,\frac{\cos(k_r x - \sigma t + \varphi'')}{\cos(k_r x - \sigma t + \varphi/2)}. \tag{I-43}$$

To examine the velocity distribution versus z in the lower layer we shall study the velocities for a given value of x, for different times within a half period. The velocities are expressed as fractions of the maximum velocity in the upper layer. For $x = 0$, these are

$$P\sqrt{(1 - \gamma g H_0 R \cos\varphi)^2 + (\gamma g H_0 R \sin\varphi)^2}\,\cos(\varphi'' - \sigma t). \tag{I-44}$$

A picture of the situation for five values of $(\varphi'' - \sigma t)$ is shown in Fig. 10, where the corresponding velocities in the upper layer are drawn in

also. The example refers to a thickness of the lower layer, $h_0 = 5$ feet, or $\sqrt{\sigma/2\nu}\, h_0 = 1.4$.

The situation for horizontal displacements is similar to that for velocities. The displacements are easily obtained by integrating the velocities with respect to time. For the upper layer, this gives horizontal displacements of

$$\text{(I-45)} \qquad \xi_1 = -\frac{gA\sqrt{R}e^{-k_i x}}{\sigma} \sin(k_r x - \sigma t + \varphi/2),$$

and, for the lower layer,

$$\text{(I-46)} \qquad \xi_2 = -\frac{gPUA\sqrt{R}e^{-k_i x}}{\sigma} \sin(k_r x - \sigma t + \varphi'').$$

From the equations above we conclude that the ratio of magnitudes is

$$\text{(I-47)} \qquad \frac{\xi_2}{\xi_1} = PU\frac{\sin(k_r x - \sigma t + \varphi'')}{\sin(k_r x - \sigma t + \varphi/2)}.$$

We are especially interested in the ratio between the maximum horizontal displacements in the lower and the upper fluid. This is, from (I-44),

$$\text{(I-48)} \qquad \frac{\xi_2 \max}{\xi_1 \max} = P\sqrt{(1 - \gamma g H_0 R\cos\varphi)^2 + (\gamma g H_0 R \sin\varphi)^2} = PU;$$

it is shown for different thicknesses of the lower layer in Fig. 11.

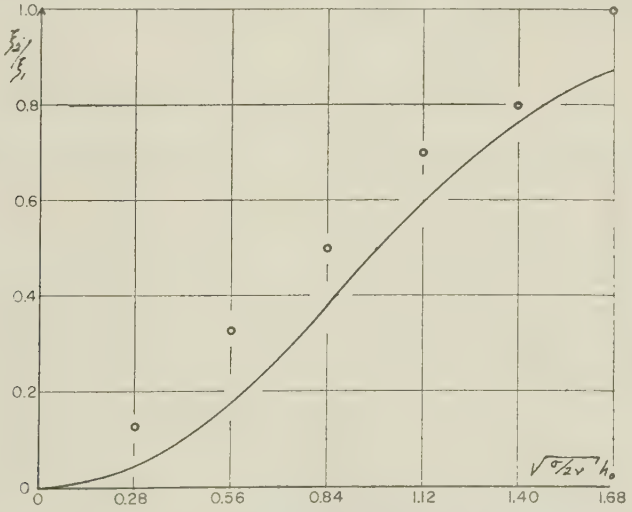

Figure 11. The curve shows the ratio between the horizontal displacements in the lower and the upper fluid versus Reynolds number $\sqrt{\sigma/2\nu}\, h_0$. The circled points show results from a separate wave tank experiment.

6. *The Ratio Between Amplitudes At The Interface And At The Surface.* The amplitude η_1 at any place at the surface is $Ae^{-k_i x}$, when A is the amplitude at $x = 0$.

The amplitude at the interface for the same value of x is, from (I-37),

(I-49) $$\eta_2 = ASe^{-k_i x},$$

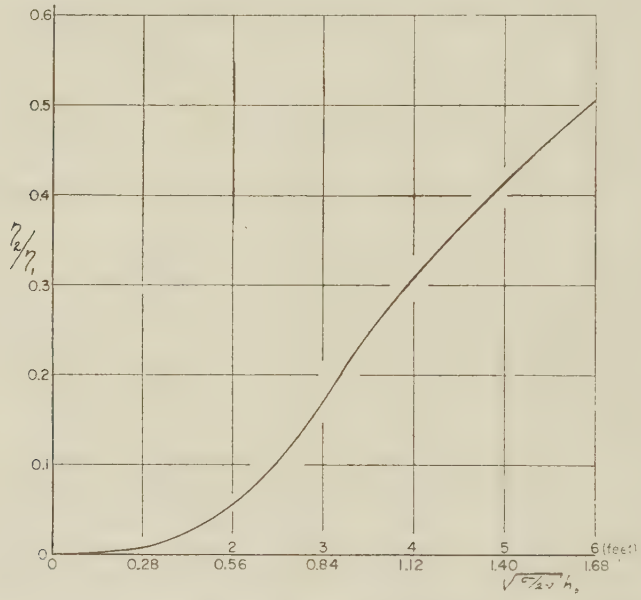

Figure 12. The curve shows the ratio between the wave amplitudes at the interface and at the surface versus the Reynolds number $\sqrt{\sigma/2\nu}\, h_0$.

where S, defined by (I-33), is given by

$$S = \sqrt{(1 - gH_0 R \cos\varphi)^2 + (gH_0 R \sin\varphi)^2}.$$

Therefore, at any place the ratio between the amplitude at the interface and at the surface is

(I-50) $$\frac{\eta_2}{\eta_1} = S.$$

Fig. 12 shows this ratio versus $\sqrt{\sigma/2\nu}\, h_0$.

PART II. ENERGY CONSIDERATIONS

I. *Energy Transport Through The Interface.* In the following section the energy dissipation of a surface wave is discussed. Also, an estimate of the probable size of the decay parameter $e^{-k_i x}$ under natural conditions is given.

The following development is based upon the same restrictions and assumptions as those used in Part I.

Consider the average energy transport P through the interface per unit area and unit time. The work dW done per unit area in time dt on the lower layer at a given abscissa is

$$dW = -p\frac{dn}{dt}dt, \tag{II-1}$$

where p is the pressure and dn is the infinitesimal displacement normal to the interface of an element of the interface. Because of Assumption (g) in Part I and because the ratio between the amplitudes on the interface and on the surface is always less than one (I-50), the slopes of the interface at any point will be very small and we can make the approximation in (II-1): $dn = dh$, where dh refers to an infinitesimal increase in the height of the interface. During a whole period T at a particular point, the total work done per unit area is found by integration of (II-1), hence the average energy transmitted through the interface per unit area and time during a whole cycle is

$$P = -\frac{1}{T}\int_0^T p\frac{dh}{dt}dt, \tag{II-2}$$

In (II-2) both h and p are functions of time t:

$$h = h_0 + ASe^{-k_i x}\cos(k_r x - \sigma t + \varphi') \tag{II-3}$$

$$dh = AS\sigma e^{-k_i x}\sin(k_r x - \sigma t + \varphi')\,dt \tag{II-4}$$

and

$$p = p_a + \rho g H, \tag{II-5}$$

where p_a is the atmospheric pressure and ρ the density of sea water. From (I-14) and (I-16) it follows that

$$\begin{aligned} H &= H_0 B\frac{k}{\sigma}\cos(k_r x - \sigma t)e^{-k_i x} + H_0 \\ &= H_0 gA\left(\frac{k}{\sigma}\right)^2\cos(k_r x - \sigma t)e^{-k_i x} + H_0 \\ &= H_0 gA\,R\cos(k_r x - \sigma t + \varphi)e^{-k_i x} + H_0\ . \end{aligned} \tag{II-6}$$

Inserting the above results in (II-2) we get

$$P = \frac{1}{T}\int_0^T [-(p_a + \rho g H_0) - \rho g^2 H_0 R A e^{-k_i x} \cos(k_r x - \sigma t + \varphi)] \frac{dh}{dt}\, dt. \tag{II-7}$$

By using (II-4) this integral can be evaluated. The two first terms do not contribute to the integral. Evaluation gives

$$P = \frac{-1}{2} S A^2 e^{-k_i x 2} \rho g^2 H_0 R \sin(\varphi' - \varphi). \tag{II-8}$$

Substituting in (II-8) the result from (I-50), we get

$$P = -\rho g \frac{1}{2} (A e^{-k_i x})^2 g H_0 R \frac{\eta_2}{\eta_1} \sin(\varphi' - \varphi). \tag{II-9}$$

Equation (II-9) is interesting because it allows us to give an approximate estimate of the energy loss due to a nonrigid bottom from observations at a single station. If we assume that the amount of energy in transport in the lower layer is negligible compared with that of the upper layer, we can approximate the total average energy in the wave per unit area by

$$E = \frac{1}{2} \rho g (A e^{-k_i x})^2. \tag{II-10}$$

With the help of (II-10) we can now express the mean *relative* energy loss per unit area and unit time:

$$\frac{P}{E} = g H_0 R \frac{\eta_2}{\eta_1} \sin(\varphi - \varphi'). \tag{II-11}$$

We note here that the dimensionless parameter $gH_0 R$ is likely to be found in the vicinity of unity, though always less. Furthermore, the angle φ is small compared to φ'; as stated previously, the latter is always negative, making the ratio P/E positive. Thus, if it is possible to measure simultaneously the wave heights at the surface and at the interface and to measure also the phase angle φ' between the wave profiles, by making use of (II-11) with $gH_0 R = 1$ and $\varphi = 0$ we can get a useful estimate of the energy loss due to a nonrigid bottom and thereby of the corresponding rate of decay.

2. *Energy Loss In Case Of Bottom Friction Only Over A Rigid Bottom.* For comparison we give the energy loss over a rigid sand bottom due to bottom friction only. It has been shown previously by Lamb (1932),

Putnam and Johnson (1949), that for sinusoidal waves of small amplitude the amount of energy D_f, dissipated per unit area at a horizontal bottom per unit time, is given by

(II-12) $$D_f = \frac{4}{3} \frac{\pi^2 G^3 f \rho}{T^3 \left(\sinh \frac{2H}{L} \right)} ;$$

ere ρ is the density of water, G the wave height, L the wave length, H he still water height, and f a dimensionless parameter representing the iction coefficient for the bottom.

In case of relatively shallow water, equation (II-12) can be approxiated by

(II-13) $$D_f = \frac{\rho (GL)^2 f}{6\pi (TH)^3} ,$$

here T is the period of the wave.

3. *Modification Of The Surface Wave Height.* Usually, modification f a wave due to bottom friction is expressed by the friction coefficient K_f defined by

(II-14) $$G = G_0 K_f ,$$

here G_0 is the wave height at an arbitrary reference point and G the ave height at some other position, assuming steady state conditions. he friction coefficient K_f is related to f in (II-13) by the following xpression (Bretschneider and Reid, 1954):

(II-15) $$K_f = \frac{1}{1 + \frac{2fG_0}{3\pi} \frac{(x - x_0)}{H^2}} ,$$

here index refers to a reference point, x being the horizontal coordinte. Note that the expression is not in an exponential form.

In the following, an 8 second period wave will be discussed on four et of water. For example, let the wave height be two feet, and reard the wave as decaying over a distance of 1000 feet. A typical alue for f is 0.01. In this case K_f will be 0.79, which means that the ave height is reduced to 79% of the initial value over a distance of 00 feet.

Let us now look at the decay over a region with a soft bottom where e coefficient of viscosity $\nu = 5$ ft^2/sec. The water depth and the ave period will be the same as previously. From Fig. 4, the maxium value of $k_i = 0.0078$, while $k_i = 0.004$ would be more probable.

Over 1000 feet, this will correspond to a decay amounting to less tha
2% of the initial value; even if we consider $k_i = 0.001$, we should fin
that over 1000 feet the remaining wave height would be less than 37%
of the initial wave height. The situation $k_i = 0.001$ would exist with
layer of mud or clay roughly 1.5 feet thick.

ACKNOWLEDGEMENT

The author wishes to thank Mr. Robert O. Reid for the initiation o
this study and for his constructive suggestions and to express gratitud
to Dr. Basil W. Wilson for his stimulating criticism.

REFERENCES

Bretschneider, C. L. and R. O. Reid
1954. Modification of wave height due to bottom friction, percolation and refrac
tion. Tech. Memo. U. S. Beach Erosion Bd. Corps Engrs., *45*.

Ewing, Maurice and Frank Press
1949. Notes on surface waves. Ann. N. Y. Acad. Sci., *51:* 3, 453.

Lamb, Horace
1932. Hydrodynamics. Cambridge University Press. 738 pp.

Purnam, J. L. and J. W. Johnson
1949. The dissipation of wave energy by bottom friction. Trans. Amer. geophys
Un., *30:* 67–74.

Seiwell, H. R.
1947. Investigation of underwater pressure records and simultaneous sea surfac
patterns. Trans. Amer. geophys. Un., *28:* 722.

THE EFFECT OF PRESSURE ON THE ELECTRICAL CONDUCTIVITY OF SEA-WATER

By

B. V. HAMON

Division of Fisheries and Oceanography, C.S.I.R.O. Cronulla, New South Wales, Australia

ABSTRACT

Values of the pressure coefficient of electrical conductivity of sea-water (chlorinity 9.7‰) at different temperatures are presented. The pressure coefficients vary from $.50 \times 10^{-5}$ decibar^{-1} at 0.5°C to 0.82×10^{-5} decibar^{-1} at 19.5°C. The accuracy is stimated to be ±5%. The results have been confirmed by tests at sea.

INTRODUCTION

For measurement *in situ* of the chlorinity of sea water by means of lectrical conductivity, it is necessary to allow for the effect of pressure n conductivity. This report presents results of some measurements of his effect. The measurements were made during the development of a emperature-chlorinity-depth recorder (Hamon, 1955), details of which re published elsewhere. The accuracy of the measurements was limited y the design requirements of the recorder, and it is realized that a more horough investigation will be required if the technique of *in situ* chlorin-y measurements is further refined and if its practice becomes more ommon. The present results are therefore tentative only.

LABORATORY MEASUREMENTS

Apparatus. Laboratory measurements of the effect of pressure on onductivity were made on a single sample of sea water of chlorinity 9.7‰. The sample was placed in a stainless steel pressure vessel (500 c capacity). A glass conductivity cell with platinised platinum elec-rodes, of the same type as that used in the portable temperature-hlorinity bridge previously described (Hamon, 1956), was attached to thermometer socket protruding downwards from the lid of the pressure essel. The two outer electrodes were connected electrically to the hermometer socket while an insulated lead from the centre electrode was rought out through a spark plug. Before sealing the vessel but after he cell had been covered by the sea water, a small amount of pure light etroleum was floated onto the surface of the water to prevent con-

tamination of the pressure control valves as the pressure was being re duced.

The conductivity cell was connected into a bridge circuit with 100 c/s supply and cathode-ray oscilloscope detector. The bridge wa balanced by means of a resistance box in an arm of the bridge adjacen to the cell so that the box resistance is directly proportional to the con ductivity of the sample, assuming that the cell constant is fixed. Th sensitivity was such that a change of less than 0.01% could be detected but for most tests the balance was adjusted to about $\pm 0.03\%$.

Adiabatic Tests. Since the deep water in the sea is always cold, it wa necessary to measure the pressure effect at temperatures appreciabl below ambient. Since there was no thermostatically controlled bat available in which the pressure vessel could be maintained at fixed tem peratures long enough to come to equilibrium at each pressure, the lo temperature tests were made under adiabatic conditions and a correc tion was applied for adiabatic temperature rise.

For the adiabatic tests, the pressure vessel was immersed in a bucket o water, or of ice and water, until the temperature inside the vessel, meas ured by a thermometer in the thermometer socket, was nearly equal t the temperature outside. The pressure in the vessel was then increase to approximately 1500 lb/in^2 by admitting nitrogen from a cylinde The pressure was increased in three steps, the bridge balance being note at each step. The pressure changes and bridge balances were carried ou quickly so that conditions would be nearly adiabatic. A complete ru at one temperature, including readings with increasing and decreasin pressure, was completed in about one minute.

Table I shows the temperature, pressures (corrected for gauge calibra tion) and resistance box readings obtained.

The resistances were plotted against pressure at each temperatur and straight lines passing through the zero pressure reading were fitte

TABLE I. Adiabatic Pressure Tests

Temperature (°C)	*Pressure* (*lb/in*^{2})	*Resistance* (*ohm*)	*Temperature* (°C)	*Pressure* (*lb/in*^{2})	*Resistance* (*ohm*)
19.5	0	3278	6.6	0	2423
	460	3290		460	2435
	960	3305		960	2446
	1460	3319		1390	2457
11.0	0	2707	0.5	0	2035
	470	2718		460	2046
	970	2731		910	2056
	1370	2741		1450	2069

y eye. There was no indication of appreciable departure from linearity, ithin the accuracy of measurements. The slope of each line was meas-red and expressed as a fractional increase in resistance (or conductivity) r 1 decibar (10^5 dyne cm^{-2}) increase in pressure. The results are given column (2) of Table II.

ABLE II. The Pressure Coefficient of Electrical Conductivity of Sea-Water (Chlorinity 19.7‰)

(1)	(2)	(3)	(4)	(5)
Temperature (°C)	*Apparent pressure coefficient* (10^{-5} *decibar*$^{-1}$)	*Adiabatic temperature rise* (10^{-4} °C *decibar*$^{-1}$)	*Adiabatic correction to pressure coefficient* (10^{-5} *decibar*$^{-1}$)	*Corrected pressure coefficient* (10^{-5} *decibar*$^{-1}$)
19.5	1.23	1.91	0.41	0.82
11.0	1.32	1.33	0.32	1.00
6.6	1.42	1.00	0.26	1.16
0.5	1.65	0.50	0.15	1.50

TABLE III. Measurements At Sea

(1)	(2)	(3)	(4)	(5)	(6)	(7)
			Decrease in Chlorinity			
Station	*Depth* (m)	*Temperature* (°C)	*Nansen bottle* (‰)	*T.C.D. recorder* (‰)	*Difference* (‰)	*Calculated pressure correction* (‰ *Chlorinity*)
49	560	10.5	0.42	0.25	0.17	0.12_5
	770	7.4	0.57	0.38	0.19	0.19
51	705	7.4	0.56	0.39	0.17	0.17_5
	895	5.8	0.60	0.36	0.24	0.23_5
56	675	7.75	0.55	0.39	0.16	0.16_5
	890	5.8	0.60	0.38	0.22	0.23_5
59	710	7.75	0.55	0.36	0.19	0.17_5
	960	5.65	0.59	0.35	0.24	0.25_5
64	750	8.1	0.56	0.39	0.17	0.18
	1000	5.5	0.63	0.37	0.26	0.26_5

The adiabatic temperature rise at each temperature, obtained by erpolation from Sverdrup, *et al.* (1942: table 13), is given in column) of Table II. The corresponding fractional changes in conductivity, ven in column (4), are based on temperature coefficients of conductivity each temperature obtained from the tables of Thomas, *et al.* (1934).

These coefficients were assumed independent of pressure. Column (5 of Table II, which gives the pressure coefficient of conductivity corrected for adiabatic temperature rise, is the difference between columns (2 and (4). Since there must be some heat exchange between the water and the walls of the cell, the calculated adiabatic corrections are probably too large and the pressure coefficients too small. This effect, if significant at all, is relatively less so at low temperatures, where the greatest accuracy is required.

Isothermal Tests. To check the validity of the correction for adiabatic temperature rise, tests were carried out under isothermal conditions a

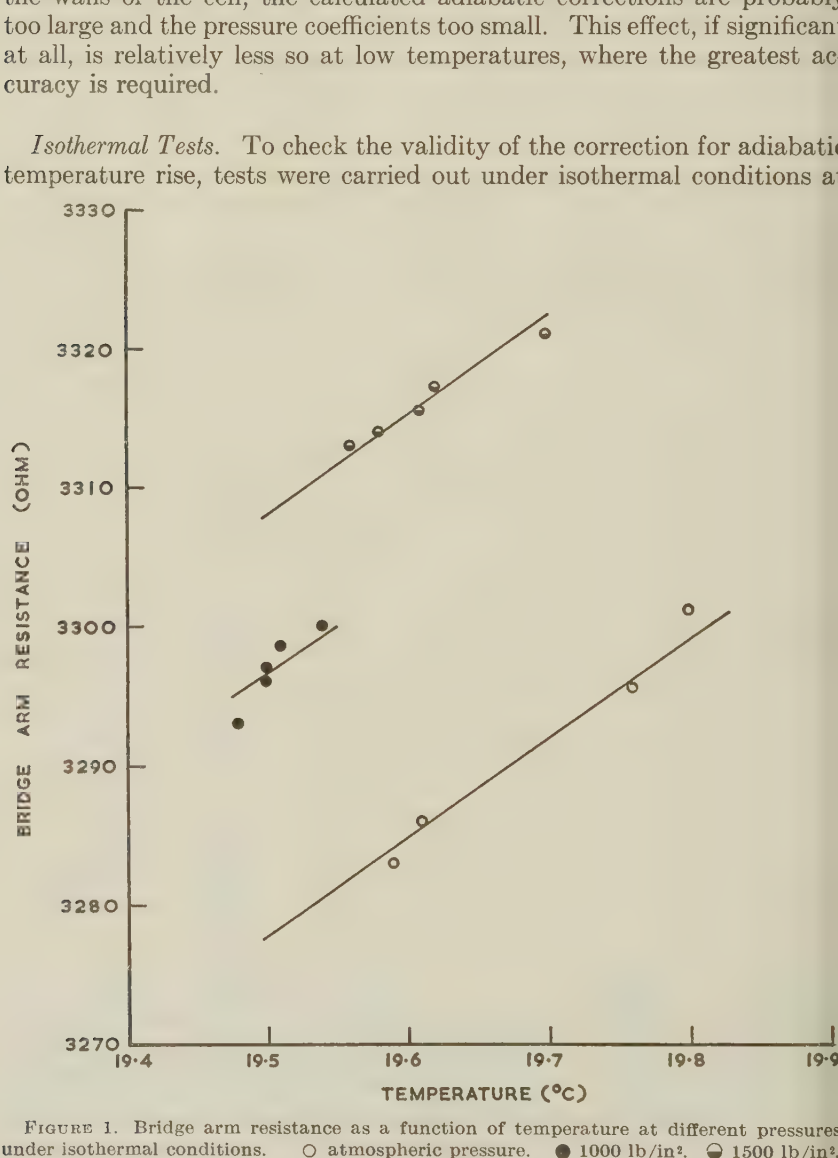

FIGURE 1. Bridge arm resistance as a function of temperature at different pressures under isothermal conditions. ○ atmospheric pressure. ● 1000 lb/in². ◒ 1500 lb/in².

oom temperature. Each pressure was held constant until stable condi-ions were reached, when simultaneous readings of temperature and re-istance were made. Fig. I shows the results obtained. The straight nes were drawn with a slope determined from the tables of Thomas, *t al.* (1934) but were positioned by eye. From the intercepts of the lines ith the 19.5°C ordinate, a mean pressure coefficient of 0.89×10^{-5} cibar^{-1} was deduced. This agrees with the value 0.82×10^{-5} decibar^{-1} iven in Table II, within the accuracy of the tests.

MEASUREMENTS AT SEA

The temperature-chlorinity-depth recorder was tested in the Tasman ea in April 1956. At five stations, the recorder was lowered either just ore or just after the usual water-bottle casts were made so that the sults could be compared. The change in chlorinity from its surface alue was computed for the two deepest water-bottle samples that came ithin the depth range of the recorder. These values are given in column 4) of Table III. The chlorinity differences determined for the same epths from the recorder are given in column (5). These differences, erived from laboratory calibrations of the recorder, include a small orrection for lack of exact compensation for the effects of temperature n conductivity. The difference between columns (4) and (5) shown in olumn (6) represents the effect of pressure. Column (7) shows for com-arison the pressure correction calculated from the laboratory tests for ne depths and temperatures shown. These figures are based on the sual approximation of 1 decibar = 1 metre and on a conductivity ange of 4.6% for 1‰ change in chlorinity (Thomas, *et al.*, 1934).

The agreement between columns (6) and (7) is very satisfactory for l except the first pair of values. It is thought that this large discrepancy due to an error in Nansen bottle depth, since the stray angle was very rge on this cast and since only two unprotected thermometers were in se.

CONCLUSION

Fig. 2 summarizes the results obtained. The curve represents the diabatic test results of Table II. It is considered that the ordinates of is curve are accurate to ±5%. This is adequate for determining lorinity at depths up to 1000 m to an accuracy of about ±0.01‰; r greater depths or more precise chlorinity determinations, more ac-urate measurements of the pressure coefficient will be necessary.

The results of the isothermal test and the measurements at sea are cluded in Fig. 2. A pressure coefficient for 2.865% sodium chloride lution at 25°C, obtained by interpolation from the results published Adams and Hall (1931), has also been plotted. This value is lower an would be expected by extrapolation of the curve. Results given by

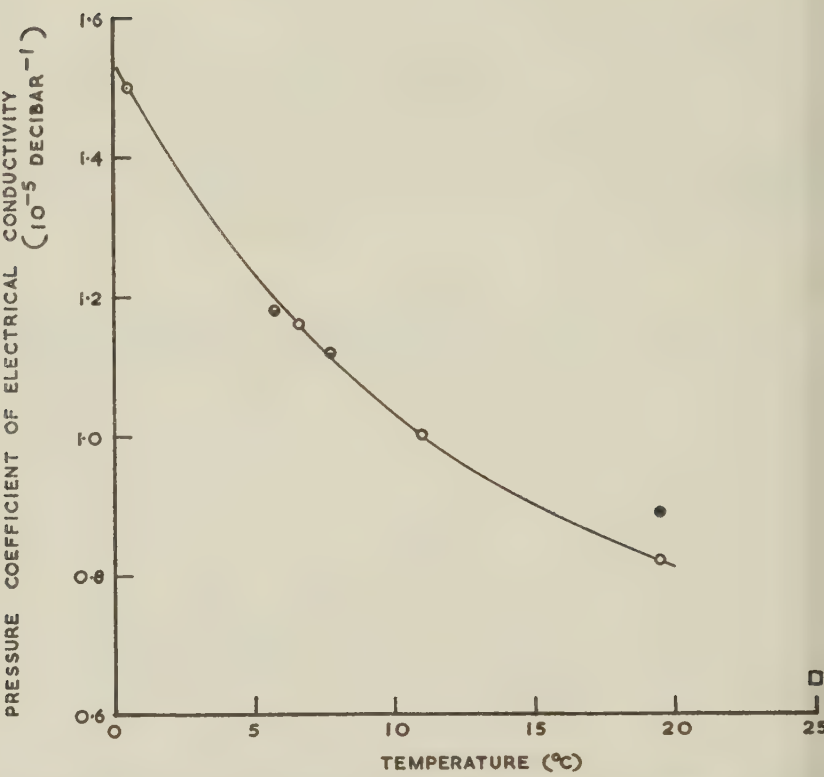

FIGURE 2. The pressure coefficient of electrical conductivity as a function of tempera ture. ○ adiabatic tests on sea water of chlorinity 19.7‰. ● isothermal tests on th same sample. ◒ measurements at sea (results in Table III, excluding the first, divide into two groups according to depth, and averaged separately). □ 2.865% sodium chl ride solution (Adams and Hall, 1931).

Adams and Hall (1931) for other concentrations indicate that the dis crepancy is not of the sign to be expected from the difference in concen tration.

ACKNOWLEDGMENTS

The laboratory experiments reported here were carried out in th Division of Electrotechnology, C.S.I.R.O.

REFERENCES

Adams, L. H. and R. E. Hall

1931. The effect of pressure on electrical conductivity. J. phys. Chem., *35:* 2145.

Hamon, B. V.

1955. A temperature-salinity-depth recorder. J. Cons. int. Explor. Mer, *21:* 72–73.

1956. A portable temperature-chlorinity bridge for estuarine investigations and sea-water analysis. J. sci. Instrum., *33:* 329–333.

Sverdrup, H. U., M. W. Johnson, and R. H. Fleming

1942. The Oceans. Prentice-Hall, Inc., New York. 1087 pp.

Thomas B. D., T. G. Thompson and C. L. Utterback

1934. The electrical conductivity of sea-water. J. Cons. int. Explor. Mer, *9:* 28–35.

SPECTRAL ANALYSIS OF A SEA-SURFACE TEMPERATURE AND ATMOSPHERIC PRESSURE RECORD OFF SOUTHERN CALIFORNIA[1]

By

GUNNAR I. RODEN

ABSTRACT

Sea-surface temperature and atmospheric pressure records during the past 40 years indicate that an inverse relation exists between the temperature at La Jolla, California, and the pressure difference at Lat. 30N, Long. 110–130W. A spectral analysis of these records is made and the energy density, autocorrelation, coherence and phase relations are investigated.

Introduction. During the last 40 years, records have been made of the temperature of the sea surface at the end of Scripps Pier, La Jolla, California. These records, if plotted against time, show seasonal as well as nonseasonal variations. These nonseasonal variations are not understood at the present time, though in many cases it has been possible to relate them to large scale changes in the atmospheric circulation (Roden and Reid, MS.). In order to eliminate seasonal variations of temperature and wind, anomalies are used in the present investigation. The term "anomaly," here defined as the monthly mean minus the mean monthly mean, has been applied to all points of the record. The wind anomaly is expressed in the form of a pressure difference anomaly, taken between Long. 110W to 130W at Lat. 30N (U. S. Weather Bureau, 1917–1956). The variation of the pressure difference and temperature anomalies with time is shown in Fig. 1. A positive pressure difference anomaly means an increased geostrophic wind from the north. It is seen that anomalies of considerable magnitude exist and that there appears to be an inverse relation between the pressure difference and temperature. The latter is consistent with the idea that north wind gives upwelling and advection of cold water. Some of the anomalies seem to be persistent over a long time. It is the purpose of this paper to subject these records to spectral analysis and to investigate whether the impressions gained visually are substantiated.

Spectral Analysis. The method used is that developed by Tukey (1949) and further described by Munk, Snodgrass and Tucker (MS.); it involves the auto- and cross-correlations, from which the energy

[1] Contribution from the Scripps Institution of Oceanography, New Series.

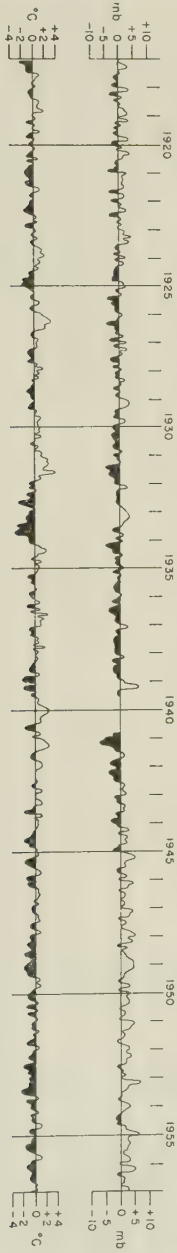

FIGURE 1. (top) Pressure difference anomaly at Lat. 30N between Long. 110W–130W; (bottom) Temperature anomaly, LaJolla Pier.

densities, coherence and phase relationships can be obtained. A definition of these quantities is given in the last mentioned paper and no recourse into the theory will therefore be attempted here. In the present case the analysis of the anomaly records was carried out by a Remington 1103 digital computer at the Convair plant in San Diego, California, for $n = 480$ (number of serial values) and $m = 62$ (number of spectral lines). The results are shown in Figs. 2 and 3. The energy spectrum of the pressure difference anomaly (Fig. 2a) shows that most of the energy is contained in the low frequency part of the spectrum, *viz.*, between zero and 1.6 cycles per year. The total energy amounts to $4.62(\text{mb})^2$. The peak at about one cycle per year is quite pronounced; however, it is an artificial feature due to the incomplete elimination of the annual term and therefore it is of no significance. The high frequency part of the spectrum contains relatively little energy

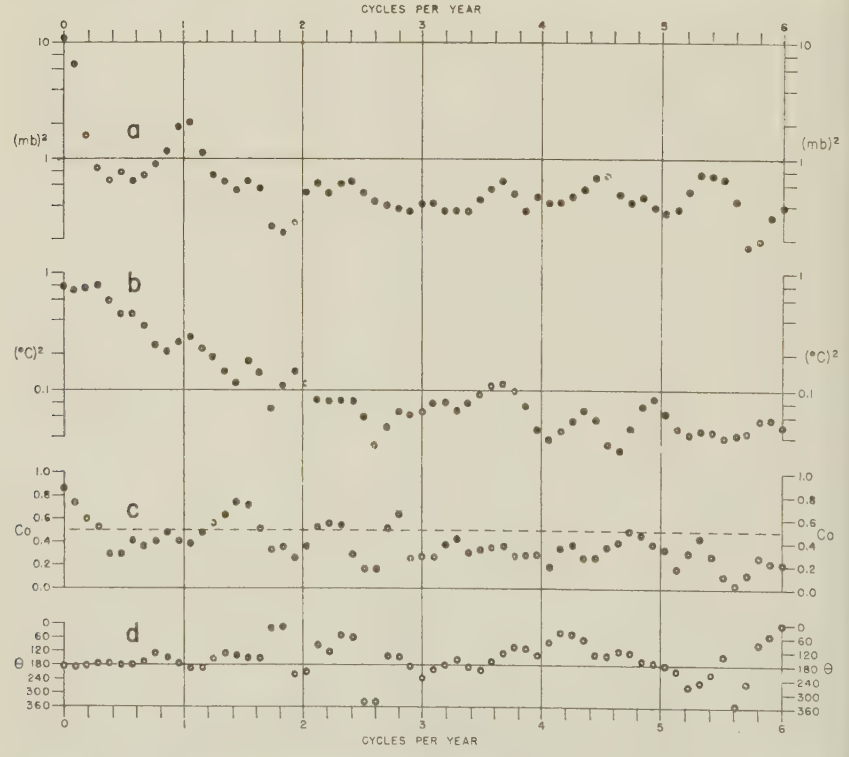

FIGURE 2. *a*, Energy spectrum of pressure difference anomaly; *b*, Energy spectrum of temperature anomaly; *c*, Coherence between pressure difference and temperature anomaly; *d*, Phase lead of pressure difference anomaly over temperature anomaly.

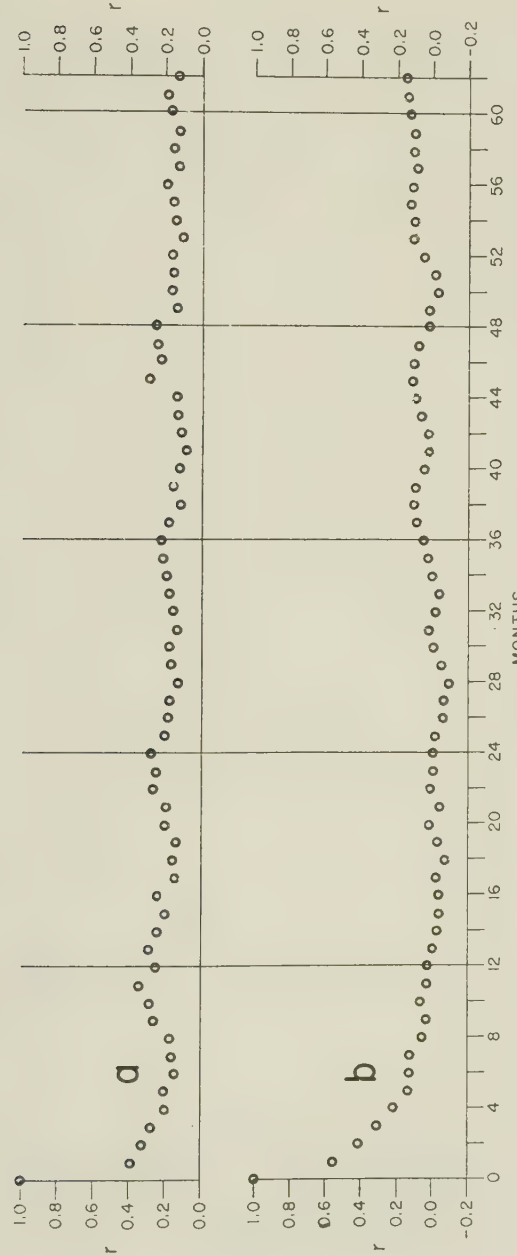

FIGURE 3. *a*, Autocorrelation of pressure anomaly; *b*, Autocorrelation of temperature anomaly.

and its features are probably insignificant. The energy spectrum of the temperature anomaly (Fig. 2b) is similar to the pressure difference anomaly in that the largest part of the energy is contained in the low frequency part of the spectrum. The total energy is 0.87 $(°C)^2$. The coherence between the pressure difference and temperature anomalies is shown in Fig. 2c. The 95% confidence limit (for discussion, consult Munk, Snodgrass and Tucker, MS.) lies at 0.51 (dashed line). From this it is seen that the coherence is significant for low frequencies only. Prominent peaks occur at approximately 1.5, 2.3 and 2.8 cycles per year, but their meaning is not readily understood. The phase (Fig. 2d) represents the phase lead of the pressure difference anomaly over the temperature anomaly. The outstanding feature is the 180 degree phase difference, indicating that an inverse relation exists between both. This confirms the visual impression shown in Fig. 1. The inverse relationship is particularly pronounced for frequencies between 0 and 1.7, and again between 2.6 and 3.4 cycles per year. The autocorrelation of the pressure and temperature anomalies is shown in Figs. 3a and 3b, respectively. The 95% confidence limits lie at $r = \pm 0.1$. The interesting feature is that the autocorrelation of the pressure anomaly remains positive for more than 62 months and that the function decreases very little with time after the sharp drop during the first month. The autocorrelation of the temperature anomaly reaches the 95% confidence limit after six months. The slight increase of function with time at the end of the record is probably insignificant.

Summing up the spectral analysis of the records has yielded the following results: a) there exists an inverse relation between the anomalies of temperature at La Jolla Pier and the pressure difference (*i.e.*, the northerly wind component) at Lat. 30N, Long. 110–130W; b) the coherence between pressure difference and temperature anomalies is better for low frequencies (long periods) than for high frequencies (short periods); c) the pressure difference anomalies are persistent over a longer time than are the temperature anomalies.

Acknowledgment. The author is indebted to Walter H. Munk, Gordon W. Groves and Gaylord Miller for valuable discussion and suggestions.

REFERENCES

Munk, W. H., F. E. Snodgrass and M. J. Tucker
Spectra of low frequency ocean waves. (Unpublished manuscript).

Roden, G. I., and J. L. Reid, Jr.
On a relation between atmospheric pressure and sea surface temperatures in the North Pacific Ocean. (Unpublished manuscript).

Tukey, G. W.
1949. A sampling theory of power spectrum estimates. Symp. Appl. Autocorrelation Analysis of Phys. Probl. ONR. Woods Hole, Mass. pp. 47–62.
U. S. Weather Bureau
1917–1956. Monthly mean sea level pressure for the northern hemisphere. Published monthly by the Extended Forecasting Section of the U. S. Weather Bureau, Washington, D. C.

COMPARISON OF LIGHT DISTRIBUTION ABOVE AND BELOW WATER[1]

By

JOHN E. TYLER

Scripps Institution of Oceanography, University of California
La Jolla, California

ABSTRACT

Recent measurements of natural light distribution in homogeneous lake water have revealed interesting and heretofore unrecorded optical effects in the near-surface layers. These effects are graphically described and explained.

From 1935 to 1945, studies of the angular distribution of natural light underwater revealed many interesting features of the underwater light field (1, 2, 4, 5, 7, 8). Concurrently, instrumentation in this field advanced with the development of the "shadowing-screen" photometer, described by Pettersson (1) and by Johnson and Liljequist (2), and of the Gershun (3) tube photometer, which directly limited the solid angle of acceptance. However, the work was performed at depths below five meters, and the instruments were limited to a low resolving power (15 to 20°). Consequently, no information was obtained on the distribution of light in the near-surface layers.

It is clear that, from a point just below the calm surface of a large body of water, the directional distribution of natural light overhead will be a compressed version of the scene above the surface. This is in keeping with Snell's law of refraction. As the depth of observation is increased, the light field will change from this complex structure; image detail will be lost and the shape of the radiance distribution solid will become smooth; with increasing depth the brightest spot in the field will move toward the zenith and the shape of the radiance distribution solid will become more symmetrical around the vertical axis. Finally, at some unknown depth, the radiance distribution solid becomes substantially fixed in shape.

Because of the exponential nature of the attenuation of light in water, these changes in light distribution will take place most rapidly in the surface layers. Thus the upper layers are at once the most interesting, the most complex, and the most difficult to explore.

[1] Contribution from Scripps Institution of Oceanography, University of California, New Series. This work has been supported by the Bureau of Ships and by the Bureau of Aeronautics under Contract NObs-72092.

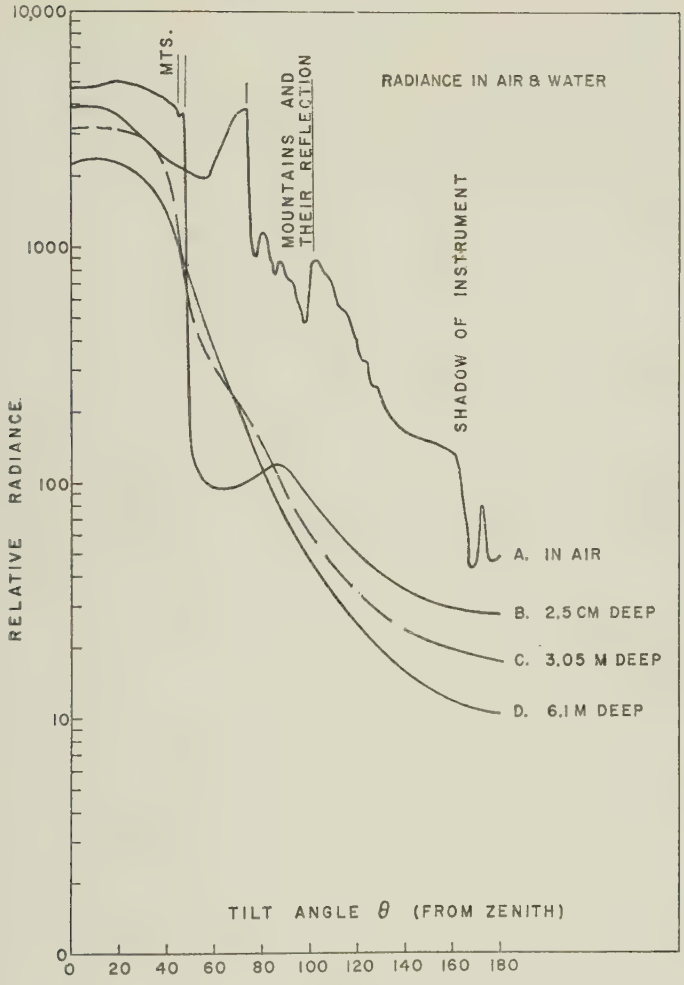

Figure 1

During recent field work at Lake Pend Oreille, Idaho, details of some of the optical effects that occur in these upper layers were explored with an underwater photometer having a resolving power of 6.6°; this underwater photometer was first described in 1955 (6). Measurements of the radiance distribution in a single vertical plane were made on an overcast day,[2] first in air and then from different depths beneath the surface. The fully corrected data are shown in Fig. 1.

[2] The sun was not visible. Its position was approximately 45° west of the instrument heading and at an altitude of 61.0°.

Curve A shows results of observations taken in air. From $\theta = 0°$ to $\theta = 74°$ the curve reports the radiance of the overcast sky; at $\theta = 74°$ the dark mountainous skyline is recorded, and this is followed by detail representing patches of dark rock or snow. From $\theta = 90°$ to $\theta = 102°$ the reflection of the mountains is recorded and this is then followed by reflection of the sky disturbed by slight wave action. At 162° the instrument's own shadow image is recorded.

Curve B shows the radiance distribution in the same direction as that in curve A but from a depth of 2.5 cm below the water surface. In the zenith direction, B shows higher radiance than A because the space light contributed by 2.5 cm of water is greater than the absorption of this same path. (It is also possible that some change took place in the zenith overcast during the short time interval between curves A and B.) Optical compression of the sky tends to keep the radiance at a high level for the first 40°. The skyline itself is very much compressed and can no longer be resolved, but the edge of the Snell circle of light appears sharp and distinct at 48°. Beyond 48° the instrument measures the radiance of the short path to the surface plus a longer reflected path that looks down into the water at an angle equal to $(180° - \theta)$. This accounts for the changes in slope of the curve between 48 and 88°. Beyond 88° the path radiance is due entirely to space light from one direction only, which decreases steadily as the tilt angle increases to 180°.

Curve C shows the radiance distribution in the same direction as curves A and B but from a depth of 3.05 m. Some detail can still be observed. The steep slope between 40 and 48° is the remaining radiance change at the edge of the Snell circle of light. The dark band at 60° exhibited in B is nearly obscured by space light; in C, between 50 and 80°, it can just be seen together with its brighter rim.

Curve D shows the radiance distribution in the same direction as the other curves but from a depth of 6.1 m. At this depth all fine detail is lost, leaving only the gross changes in radiance between zenith and nadir settings.

Between 90 and 180° the underwater curves for various depths can be approximately predicted from the equation

$$N_D = N_0 e^{-CD},$$

where N_D is the radiance at depth D, N_0 is the radiance at depth 0 and $C = f(\theta)$. Below 6.1 m the coefficient C tends to become independent of θ, approaching an asymptotic value which is characteristic of the hydrosol.

REFERENCES

(1) Pettersson, Hans
1938. Measurements of the angular distribution of submarine light. Rapp. Cons. Explor. Mer, *108* (2): 9.

(2) Johnson N. G. and G. Liljequist
1938. On the angular distributions of submarine daylight and on the total submarine illumination. Svenska hydrogr.-biol. Komm. Skr., Hydrogr. *14:* 3.

(3) Gershun, A. (Translated by Parry Moon)
1939. The Light-Field. J. Math. Phys., *18:* 51–151.

(4) Poole, H. N.
1945. The angular distribution of submarine daylight in deep water. Sci. Proc. R. Dublin Soc., *24* (4): 29–42.

(5) Whitney, L. V.
1941. The angular distribution of characteristic diffuse light in natural waters. J. mar. Res., *4* (2): 122–131; J. opt. Soc. Amer., *31:* 714–722.

(6) Duntley, S. Q., *et al.*
1955. An underwater photometer. J. opt. Soc. Amer., *45:* 904(A).

(7) Takenouti, Yositada
1940. Angular distribution of submarine solar radiations and the effect of altitude of the sun upon the vertical extinctions coefficient. Bull. Jap. Soc. sci. Fish., *8:* 213–219.

(8) Jerlov, N. G. (Johnson)
1951. Optical studies of ocean waters. Reports of the Swedish Deep-sea Expedition, 1947–1948. *3*, Physics and Chemistry #1: 1–59.

PROFILES OF WIND-CREATED WATER WAVES IN THE CAPILLARY-GRAVITY TRANSITION REGION

By

ALLEN H. SCHOOLEY

U. S. Naval Research Laboratory
Washington 25, D. C.

ABSTRACT

Crapper (1957) has theoretically predicted that pure capillary waves have profiles that peak downward, which is the reverse of the gravity wave case. This paper confirms Crapper's theory and shows enlarged profiles of capillary waves that were photographed with a high-speed motion picture camera in a small water-wind tunnel. Under the conditions of measurements, the maximum vertical distance between trough and crest for the capillary waves observed was about 0.5 wavelength. This is roughly 70% of Crapper's theoretical figure of 0.73 and is about 3.5 times the maximum of 0.14 for gravity waves. Wave profile pictures in the transition region from capillary to gravity waves are also shown. Examples are given where capillary waves having the same velocity as the gravity waves tend to ride just in front of the start of the crests of the gravity waves.

INTRODUCTION

Large water waves having gravity as a restoring force have long been studied because of their effects on ships, breakwaters, docks, and beaches. Capillary water waves having surface tension as a restoring force have become of considerable interest in recent years because of their effect on the reflection and scattering of light and microwave radar waves from the wind-swept surface of the sea.

The trochoidal shape of single wavelength gravity waves in deep water is well known. However, only recently has an exact solution been found for the shape of pure capillary waves. Crapper (1957) has calculated the wave shapes shown graphically in Fig. 1. Each wave shape has an associated amplitude divided by wavelength (a/λ) number. If any particular wave shape is taken as the water surface, the lines below it are streamlines. The wave form of greatest height occurs when the crest-to-trough distance or amplitude is 0.73 wavelength. Higher waves are not expected to occur because the sides of adjacent waves would touch. The maximum a/λ number for gravity waves is 0.14.

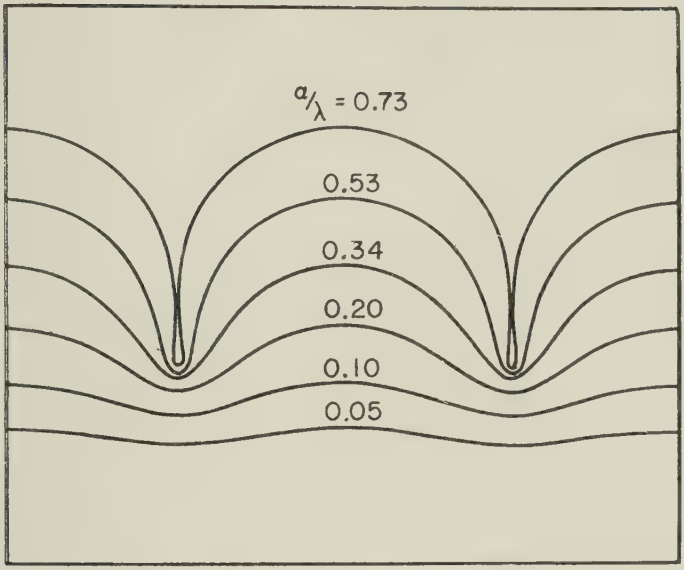

Figure 1. Crapper's theoretical capillary wave profiles for various amplitude-to-wavelength (a/λ) ratios.

Crapper's capillary wave shapes are peaked downward whereas the trochoidal shape of gravity waves are peaked upward. On the basis of pictures of wind-generated waves in a transparent channel, it is the purpose of this paper to present evidence that confirms Crapper's prediction of the shape of capillary waves and to show that under some circumstances gravity and capillary waves of the same velocity tend to propagate together.

EXPERIMENTAL PROCEDURE

The small transparent water channel shown in Fig. 2 has a provision for drawing air at various measured velocities over the water surface; this apparatus has been described previously (Schooley, 1955). Close-up pictures were taken for various wind velocities by means of a 16-mm motion picture camera operating at 72 frames per second and having a shutter speed of about 1/900 second per frame. The camera was focused on the central portion of the channel wall so as to show the water-air boundary. The view subtended slightly over 4 cm in width. A 2 cm scale was included for reference in wave length and wave height measurements. The velocity of the waves was measured by the distance they traveled between one frame and the next on the motion

picture film. To provide accurate timing, the frame rate of the camera was calibrated to better than 3% accuracy under the conditions used in taking the pictures.

RESULTS

Figs. 3 through 9 are enlargements of selected frames taken with the 16-mm motion picture camera. The light area below is the illuminated water and the dark area above is the air. The independent variable in the pictures is wind speed. The range of wind speeds was from 10 to 20 knots and the direction of air flow was from left to right.

Fig. 3 shows the starting of wave formation. Here the amplitude is about 0.07 cm and the wavelength about 1.4 cm, giving an a/λ ratio of 0.05. This wave was traveling at about the minimum velocity, corresponding to the transition region between gravity and capillary waves. The wind velocity for Fig. 3 is approximately 10 knots, which indicates that wave formation starts at a wind velocity slightly below this value. This is considerably higher than that experienced for the initiation of wave formation on open bodies of water (Schooley, 1954). The high threshold velocity, observed previously (Schooley, 1955), was attributed to possible inaccurate wind velocity measurements and to the possibility that water contamination lowered the surface tension. In the present experiments the wind velocity measurements were carefully checked and appear to be consistent with the earlier results. As will be evident later in this paper, the surface tension of the water channel appears not to be appreciably depressed by contaminants. Thus, it is believed that low air turbulence due to the short fetch may have an effect on the threshold wind velocity at which waves form.

Figs. 4–6 are presented for a 12 knot wind because Crapper's wave shapes are most clearly evident at this velocity. The waves are not of a single frequency and amplitude because the driving force of the wind tends to generate a spectrum of waves. However, the peaked downward shape is shown in portions of these figures. The maximum value of a/λ for Figs. 4–6 is about 0.23, 0.30, and 0.29, respectively. These values of a/λ would place the wave profiles in the central region of Fig. 1. However, the sharp troughs shown in Figs. 5 and 6 appear to match more nearly the region between $a/\lambda = 0.53$ and $a/\lambda = 0.73$. Actually it is difficult to measure precisely a/λ in the pictures because of the thin water film that tends to cling to the transparent wall of the channel along the average water-level mark. Due to this film, the profile of waves that are below the average water mark are emphasized by a dark band while the profile of waves above the average water line are suppressed, except for large gravity waves at high wind velocities.

Figure 2 (upper left); water channel with provision for controlled wind over the water surface. Figure 3 (upper right); water channel wave profile for 10 knot wind; (scale, 2 cm long). Figure 4 (lower left); 12 knot wind shows Crapper's wave profiles best. Figure 5 (lower right); another 12 knot wind sample.

Figure 6 (upper left); still an other 12 knot sample. Figure 7 (upper right); 14 knot wind. Figure 8 (lower left); 16 knot wind. Figure 9 (lower right); 20 knot wind.

Fig. 7 is representative of a transition region where the wavelength spectrum excited by the wind starts to show the characteristics of both long gravity waves and short capillary waves. In this case the capillary waves are about 0.7 cm long, the gravity wave about 4.6 cm. From a study of the motion picture record it is not apparent that there is a consistent phase relationship between the capillary and gravity waves.

The left side of Figs. 8 and 9 show the start of crests of gravity waves that have wavelengths of about 8 cm. It is evident that the crests are above the water film that clings to the channel wall; the troughs in the center and on the right side of the pictures are below. Preceding the start of the crests in both Figs. 8 and 9 are capillary waves having wavelengths in the general region of 0.3 cm. There is evidence that gravity waves and capillary waves travel at the same velocity because the type of phenomena shown in these figures was more or less typical of many frames of the motion picture film that was examined. In other words, there was a distinct tendency for capillary waves to ride at the start of the crest of the gravity waves, with the wavelength of each adjusted so that the velocities are identical.

It is interesting to note the train of capillary waves in front of the gravity wave in Fig. 9. The maximum a/λ in this train is slightly over 0.5, which is the largest observed in all measurements that were made. It is quite evident, however, that the film of water clinging to the side of the channel may affect the apparent shape of the waves and the accuracy to which amplitude and wavelength measurements can be made. The apparent tipping back of the crests of the capillary waves may be due to the presence of the film of water, and it also may be due to forward movement of the water in this region.

The solid curves in Fig. 10 show the relationship between wavelength and wave velocity for water waves as defined by the approximate equation

$$v = \left(\frac{2\pi T}{\lambda \rho} + \frac{g\lambda}{2\pi}\right)^{1/2}$$

where v is the water wave velocity in cm per sec, T surface tension in dynes per cm, ρ water density in gm per cm^2, and λ wavelength in cm. In plotting the curves in Fig. 10, it was assumed that ρ equaled unity, g equaled 980, and T equaled 70 and 35. The handbook value of T for pure water at room temperature is listed between 70 and 75 by various references. Since the presence of organic impurities at a water surface markedly decreases the surface tension, a curve for T equal 35 is also shown. It was originally thought that fresh Washington tap water, when placed in the water channel, would have appreciable contamina-

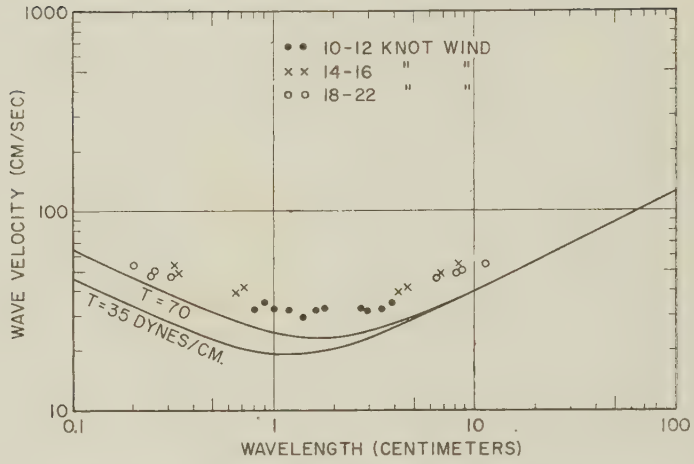

Figure 10. Theoretical curve and experimental points relating wavelength with wave propagation velocity.

tion and would thus depress the surface tension. This proved not to be the case, as will be explained below.

The experimental points in Fig. 10 were derived from pictures such as those shown in Figs. 3 through 9. Wave velocity was measured by noting the wave movement on successive frames of the motion picture film and multiplying this distance by the frame-rate of taking the pictures. Wavelength was measured directly from the pictures for the capillary waves. Since the gravity waves were longer than the picture width, it was necessary to note the number of frames for a given wave to pass a given point and multiply this by the distance traveled per frame in order to obtain the wavelength.

The experimental points in Fig. 10 appear on the average to be about 30% higher in velocity than would be expected from the upper theoretical curve. Except for this displacement they appear to follow the general shape of the $T = 70$ curve. This indicates that the surface tension of the water in the channel was not appreciably depressed by organic contaminants.

The 30% higher velocity at all wavelengths is believed to be significantly greater than the measuring errors. It may be expected that the phase velocity of the waves in the four-inch wide channel may be greater than that for an infinite surface. This would be particularly significant if the channel width was on the order of one half-wavelength or less. Actually, the channel width was about twice the longest half-wavelength measured, which would indicate a phase velocity down the

channel of about 10% above the wave velocity on a large surface; for shorter wavelengths the phase velocities should approach nearer and nearer the large surface velocity. Thus, some other interpretation is needed to explain why the experimental points in Fig. 10 are significantly above the theoretical curve.

The distribution of points with wind velocity in Fig. 10 is particularly interesting. At the low wind velocities, waves start to form at the minimum wave velocity transition region between gravity and capillary waves. As the wind velocity increases, both gravity and capillary waves having substantially the same velocities are formed. The measurements covered a range of wavelengths between about 0.2 and 11 cm. Assuming that Crapper's a/λ maximum of 0.73 for capillary waves is correct, it can be expected that the amplitude of capillary waves directly associated with long gravity waves will become small. For example, for a gravity wave of 100 cm wavelength, the maximum amplitude of an equal velocity capillary wave would be about 0.02 cm. Similarly, a 1000 cm gravity wave could only have associated with it a capillary wave of about 0.002 cm amplitude.

CONCLUSIONS

On the basis of this investigation, it can be stated:

(a) Crapper's theoretical description of capillary wave profiles with troughs peaked downward can be observed on capillary waves created by the wind.

(b) For a 13 inch fetch in a water channel with controlled velocity air drawn across the surface, the clearest evidence of Crapper's waves is experienced with a 12 knot wind.

(c) Under the circumstances of the experiments, waves started to form when the wind velocity was just under 10 knots. This is high compared to open water measurements and may indicate that low air turbulence due to short fetch is a factor in the minimum air velocity for wave formation.

(d) The wavelength of wind generated waves that first form is in the 1 to 2 cm region corresponding to the minimum velocity in the gravity-capillary transition region.

(e) As the wind velocity is increased, both gravity and capillary waves having substantially the same velocity are formed simultaneously.

(f) At wind velocities between 16 and 20 knots it is common for capillary waves having the same velocity as the gravity waves to ride just at the beginning of the crest of the gravity waves.

(g) Crapper's prediction for the maximum ratio of amplitude to wavelength of 0.73 for capillary waves was approached closely enough to give confidence in its correctness.

(h) Assuming the 0.73 figure to be correct, the maximum amplitude of capillary waves that can be associated with the starting of the crest of gravity waves becomes very small as the gravity wave wavelength is increased beyond 100 cm.

ACKNOWLEDGMENT

The author wishes to thank Prof. Willard Pierson, Jr., for bringing the work of Dr. Crapper to his attention.

REFERENCES

Crapper, G. D.

1957. An exact solution for progressive capillary of arbitrary amplitude. J. fluid Mech., *2:* 532–539.

Schooley, A. H.

1954. A simple optical method for measuring the statistical distribution of water surface slopes. J. opt. Soc. Amer., *44:* 37–40.

1955. Curvature distributions of wind-created water waves. Trans. Amer. geophys. Un., *36:* 273–278.

EFFECT OF CORIOLIS FORCE ON EDGE WAVES (I) INVESTIGATION OF THE NORMAL MODES[1]

By

ROBERT O. REID

Department of Oceanography and Meteorology
Agricultural and Mechanical College of Texas

ABSTRACT

Essentially two classes of free edge waves can exist on a sloping continental shelf in the presence of Coriolis force. For small longshore wave length, fundamental waves of the first class behave like Stokes edge waves. However, for great wave lengths (of several hundred kilometers or more) the characteristics of the first class are significantly altered. In the northern hemisphere the phase speed for waves moving to the right (facing shore from the sea) exceeds the speed for waves which move to the left. Also, the group velocity for a given edge wave mode has a finite upper limit. Waves of the second class are essentially quasigeostrophic boundary waves with very low frequency and, like Kelvin waves, move only to the left (again facing shore from the sea). Unlike Stokes edge waves, those of the quasigeostrophic class are associated with large vorticity. Examination of the formal solution for forced edge waves indicates that those of the second class may be excited significantly by a wind stress vortex. Also, in contrast to the conclusion of Greenspan (1956), it is proposed that a hurricane can effectively excite the higher order edge wave modes[2] in addition to the fundamental if wind stress is considered.

INTRODUCTION

It was shown by Stokes (1846) that a sloping beach or continental shelf can act as a wave guide such as to allow for the possibility of surface gravity waves which travel along shore with an amplitude which decays exponentially with distance from shore (Fig. 1). Ursell (1952) has shown that the Stokes wave is the fundamental mode of a discrete spectrum of edge wave modes which are possible. The higher order modes are characterized by an integer number of nodal lines parallel to shore.

In the Stokes-Ursell theory, no restrictions are imposed upon the vertical pressure gradient, and results are therefore applicable for a beach of any uniform slope adjacent to a straight coastline. For suitably small bottom slope, Eckart (1951) has shown that it is possible to introduce the hydrostatic pressure approximation (as is usually

[1] Contribution from Department of Oceanography and Meteorology, A. & M. College of Texas, Oceanography and Meteorology Series No. 120.

[2] Following common usage, "higher order" here implies higher than the fundamental or first order.

done in the theory of long waves). This approximation considerably simplifies the mathematical treatment, and Greenspan (1956) has applied this long wave theory in a detailed investigation of pressure-induced edge waves on the continental shelf. In the development undertaken by Greenspan, the influence of the earth's rotation is ignored as an understandable first approximation. It is probable, however, that resurgences investigated by Greenspan as well as by Munk, *et al.* (1956) represent waves of such lengths that Coriolis force should play a significant role.

The primary object of the present paper is to investigate the role of Coriolis force in respect to the characteristics of free edge waves. However, some consideration is given to the problem of *generation* of edge waves. The theory is confined to the case of small slope for which the hydrostatic pressure approximation is applicable. Furthermore, as in previous papers on this subject, the influence of bottom friction is ignored.

It is found that characteristics of the conventional edge waves, in the presence of the earth's rotation, are significantly modified for very long waves, particularly for the fundamental mode. In addition, a quasigeostrophic class of edge waves with relatively large vorticity is possible and bears some resemblance to the Kelvin boundary wave. The quasigeostrophic edge waves are evidently the counterpart of

Figure 1. Schematic of the fundamental edge wave mode showing contours of water level (full lines for positive η, dashed lines for negative η).

the steady vortex flow which could exist in the absence of the earth's rotation.

The question of excitation of the different modes is discussed from a general point of view in an attempt to arrive at some useful criteria. In another paper (Kajiura, 1958), the particular case of excitation of the fundamental edge wave mode on a rotating earth is discussed in detail, and numerical examples are given to illustrate the influence of Coriolis force.

LIST OF SYMBOLS

The symbols which are listed below occur frequently in the discussion; other symbols are introduced in the text as required:

A	amplitude at $x = 0$
$A_{jn}(k, t)$	complex amplitude spectrum, eq. (68) or (101); dimension $[L^2]$
$C_{jn}(k)$	longshore phase velocity $(-\omega_{jn}/k)$
$D_{jn}(x, y, t; k)$	horizontal divergence of the normal mode currents
$\overline{D}_{jn}(k)$	amplitude of D_{jn} at $x = 0$
e	2.71828. . .
F_x, F_y	x and y components of the vector-forcing function $\mathbf{F}(x, y, t)$.
f	Coriolis parameter $2\Omega \sin \phi$, where Ω is the angular speed of the earth, ϕ the latitude.
$G_{jn}(k)$	longshore group velocity $(-d\omega_{jn}/dk)$
g	acceleration due to gravity
$H_{jn}(x, y, t; k)$	normal mode elevation function for $A = 1$
h	still-water depth (sx)
i	$\sqrt{-1}$
j	denotes mode: 1, 2, 3
k	longshore wave number $(2\pi/\lambda)$
$L_n(z)$	Laguerre polynomial, eq. (26)
$L'_n(z)$	$dL_n(z)/dz$
$M_{jn}(k, t)$	amplitude excitation, $dA_{jn}(k, t)/dt$
$N_{jn}(k)$	norm of the eigenfunctions, eq. (64); dimension $[L]$
n	order designation: 0, 1, 2, 3 . . . (number of nodal lines parallel to shore)
$P(x, y, t)$	atmospheric pressure at sea level
$P'(x, y, t)$	departure of P from normal
$p_{jn}(k)$	weight function, $[2 \lvert k \rvert N_{jn}(k)]^{-1}$
$Q_x(x, y, t)$	x component of volume transport per unit width
$Q_y(x, y, t)$	y component of volume transport per unit width
$q_n(z)$	Laguerre orthonormal function, eq. (25)

$S_{jn}(k, t)$	energy spectrum, Eq. (74)
s	bottom slope ($s \ll 1$)
$T_{jn}(k)$	normal mode periods ($2\pi/\lvert\omega_{jn}\rvert$)
t	time
$U_{jn}(x, y, t; k)$	normal mode equivalent of Q_x for $A = 1$
$V_{jn}(x, y, t; k)$	normal mode equivalent of Q_y for $A = 1$
$X_{jn}(kx)$	eigenfunction amplitude of U_{jn}
x	horizontal distance from shore
$Y_{jn}(kx)$	eigenfunction amplitude of V_{jn}
y	distance along shore (x, y form a right-hand system)
$Z_n(kx)$	eigenfunction amplitude of H_{jn}; $Z_n(kx) = q_n(2\lvert k\rvert x)$
z	argument of $L_n(z)$ or $q_n(z)$; dimensionless
$\eta(x, y, t)$	elevation of the sea surface above still-water level
κ	a parameter with dimension of k, eq. (23)
λ	longshore wave length ($2\pi/k$)
π	3.14159 . . .
ρ	density of sea water (assumed constant)
$\tau(x, y, t)$	surface wind stress vector
$\Phi(x, y, t)$	potential function for the divergent part of τ
$\Psi(x, y, t)$	potential function for the rotational part of τ
$\omega_{jn}(k)$	characteristic frequencies of normal modes
$\zeta_{jn}(x, y, t; k)$	vertical component of relative vorticity of normal modes
$\bar{\zeta}_{jn}(k)$	amplitude of ζ_{jn} at $x = 0$

The superscript * is employed to denote the complex conjugate of the function indicated. The formal designation of functional dependence is omitted in those cases where clarity is not imperiled. In the first part of the development the subscripts $_{j,\ n}$ do not appear in respect to the normal mode functions.

FORMULATION OF THE PROBLEM

1. The Basic Equations. We will confine our attention to undamped waves of small amplitude and of sufficient length such that linearized equations of motion with the hydrostatic pressure approximation are applicable. It will be assumed also that the density of the water is uniform. The vertically integrated, linearized equations of motion for a forced, barotropic inertiogravitational disturbance are then

$$\frac{\partial Q_x}{\partial t} - fQ_y + gh\frac{\partial \eta}{\partial x} = F_x, \tag{1}$$

$$fQ_x + \frac{\partial Q_y}{\partial t} + gh\frac{\partial \eta}{\partial y} = F_y, \tag{2}$$

and the equation of continuity is

$$\frac{\partial Q_x}{\partial x} + \frac{\partial Q_y}{\partial y} + \frac{\partial \eta}{\partial t} = 0, \tag{3}$$

neglecting precipitation or evaporation at the sea surface. The Coriolis parameter f (positive in the northern hemisphere) will be considered as a constant in the present analysis, hence planetary type waves are excluded from the analysis. The forcing functions F_x and F_y are presumed to be specified in terms of space and time variables. They are physically determined by the horizontal gradient of the atmospheric pressure at sea level, the surface wind stress, and the depth of water [see relation (79)]. It is recognized that omission of bottom stress may be a rather severe restriction in view of (4) and may deserve further attention.

The x, y-axes constitute a right-hand coordinate system, with the x-axis directed seaward and the y-axis directed along shore and coincident with the undisturbed position of the water's edge (presumed straight). It is assumed that the increase in depth is directly proportional to the distance from shore and that the sea is considered semi-infinite; thus

$$h = sx, \tag{4}$$

the bottom slope s being considered very small ($s \ll 1$). This simplification places definite restrictions on the applicability of the theory to waves whose effective length normal to shore is very large (greater than the actual width of the continental shelf).

To complete the formulation of the problem we suppose that η, Q_x and Q_y are specified as functions of x and y at $t = 0$. Finally as boundary conditions, we take η as finite at shore and

$$Q_x = 0 \qquad \text{at } x = 0 \text{ for all } y \text{ and } t; \tag{5}$$

and

$$Q_x, Q_y, \eta \to 0 \qquad \text{as } x, |y| \to \infty \text{ for all finite } t. \tag{6}$$

Condition (6) is possible only if the vector-forcing function $\mathbf{F}$ is localized in the vicinity of the coastline, such that $\mathbf{F} \to 0$ as $x, |y| \to \infty$, and if no initial disturbance exists at infinity. The periodic tides and the steady oceanic-scale circulation are therefore excluded at the outset. For a transient atmospheric disturbance in which $\mathbf{F} \to 0$ as $t \to \infty$, presumably a finite amount of energy is added to the water for $t > 0$,

and this energy is ultimately transferred to infinite y by radiation as $t \to \infty$. However, for finite t we will consider that (6) holds.

The condition of finite η at shore automatically excludes a certain class of solutions which have logarithmic singularities at $x = 0$ (Stoker, 1957: 71–72). This is certainly reasonable in view of the linearized nature of the problem. However, despite the lack of physical significance of such solutions, one is tempted to regard these as the linear approximation of unstable disturbances at the water's edge. Stoker points out that exclusion of such solutions precludes the possibility of an energy sink at shore; consequently it excludes the possibility of wave energy progressing towards shore at $x = \infty$. From a practical standpoint this implies that ordinary sea and swell are neglected in the present problem, the attention being directed entirely to the question of long edge waves.

2. Associated Normal Mode Problem. The expressions for Q_x, Q_y and η which satisfy the above relations with F_x and F_y set equal to zero will be designated as U, V and H respectively. These free wave functions therefore must satisfy the differential equations

$$\frac{\partial U}{\partial t} - fV + gsx \frac{\partial H}{\partial x} = 0, \tag{7}$$

$$fU + \frac{\partial V}{\partial t} + gsx \frac{\partial H}{\partial y} = 0, \tag{8}$$

$$\frac{\partial U}{\partial x} + \frac{\partial V}{\partial y} + \frac{\partial H}{\partial t} = 0, \tag{9}$$

subject to the conditions that H is finite at shore and that

$$U = 0 \qquad \text{at } x = 0, \tag{10}$$

$$U, V, H \to 0 \qquad \text{as } x \to \infty. \tag{11}$$

However, we make no stipulation in regard to initial conditions or to the condition for $|y| \to \infty$.

In order to establish the normal mode functions, we first introduce the transformations

$$U = X(x; k, \omega) \exp [i(ky + \omega t)], \tag{12}$$

$$V = Y(x; k, \omega) \exp [i(ky + \omega t)], \tag{13}$$

$$H = Z(x; k, \omega) \exp [i(ky + \omega t)]. \tag{14}$$

These expressions will satisfy (7) to (11) provided that the functions X, Y and Z satisfy the relations

$$i\omega X - fY + gsx\frac{dZ}{dx} = 0, \tag{15}$$

$$fX + i\omega Y + igsxkZ = 0, \tag{16}$$

$$\frac{dX}{dx} + ikY + i\omega Z = 0, \tag{17}$$

and

$$X = 0 \qquad \text{at } x = 0, \tag{18}$$

$$X, Y, Z \to 0 \qquad \text{as } x \to \infty, \tag{19}$$

where Z is finite at shore.

The elementary free waves defined by (12) to (19) are simple harmonic progressive waves of longshore length $2\pi/k$, period $2\pi/\omega$, and longshore phase speed $-\omega/k$. The wave number k is to be regarded as real but is otherwise arbitrary; consequently there exists a continuous spectrum of normal mode solutions in respect to k. However, for a given k, there are only certain admissible functions X, Y, Z which in turn are associated with particular values of ω. These represent respectively the eigenfunctions and characteristic frequencies of the system (15) to (19) for a given k.

From (15) and (16) we find that

$$X = \frac{igsx}{(\omega^2 - f^2)}\left[\omega\frac{dZ}{dx} + fkZ\right], \tag{20}$$

$$Y = \frac{-gsx}{(\omega^2 - f^2)}\left[f\frac{dZ}{dx} + \omega kZ\right]. \tag{21}$$

Inserting these relations in (17) yields

$$\omega s\left[\frac{d}{dx}\left(x\frac{dZ}{dx}\right) + (\kappa - k^2x)Z\right] = 0, \tag{22}$$

where

$$\kappa = \frac{\omega^2 - f^2}{gs} + \frac{fk}{\omega}. \tag{23}$$

The set of normal mode solutions, containing the eigenfunctions and characteristic frequencies, forms an essential part of the general solution of the forced and/or initial value problem specified by (1) to

(6). In fact this constitutes the primary justification for the investigation of the normal modes. It may be noted immediately from (20) that condition (18) and hence (10) are automatically satisfied if Z and its derivative are finite at shore. Consequently the addition of Coriolis force to the edge wave problem does not lead to the complication of a mixed boundary condition which is encountered in problems of very long surges incident upon a vertical barrier (Crease, 1956).

3. Standing "Shelf" Modes. Our main interest centers on the edge wave modes for which ω and k differ from zero, since it is only this type which can be effectively excited by a localized atmospheric disturbance. However, there are several nontrivial solutions of (15) to (17) for $k = 0$, with finite Z at shore, which might be mentioned in passing. These modes represent either standing or stationary wave patterns on the sloping shelf with uniform flow and water level along shore.

The case of $k = \omega = 0$ represents a steady geostrophic mode with H contours and with flow parallel to shore. Any transverse distribution $Z(x)$ is admissible subject to condition (19).

For $k = 0$ and $\omega > f$, (22) admits a solution with finite $Z(0)$ of the form

$$Z(x) = AJ_0(2\sqrt{\kappa x}), \tag{24}$$

where J_0 is the Bessel function of the first kind, order zero, and where A is an arbitrary amplitude. The disturbance represents a standing shelf oscillation which is independent of y but which has an oscillatory component of flow parallel to shore as well as transverse to shore. The period of these waves is less than 12 pendulum hours ($2\pi/f$). It is conceivable that this mode is of importance in the study of co-oscillating tides on the continental shelf.

For $k = 0$ and $\omega = f$, (15) to (17) admit a peculiar type of inertial motion with periodic but spatially uniform surface displacement. This is a degenerate case of (24), and as we shall see it is also a limiting case of higher order edge wave modes. Relations (20) and (21) lead to indeterminate forms in this case, but it is readily established from (16) and (17) that both X and Y have the magnitude Afx, hence the horizontal trajectories of the particles are circular as in simple inertial motion. However, in view of its spatially uniform properties, it is evident that this mode does not satisfy (19) unless $A = 0$, hence it cannot be excited by a localized atmospheric disturbance.

EDGE WAVE MODES

1. Edge Wave Eigenfunctions. For nonvanishing ω and k it can be shown (Eckart, 1951: 48–50) that the only solutions of (22) which lead to finite Z for all positive x are the functions $Aq_n(2|k|x)$, where A is an arbitrary amplitude and $q_n(z)$ is the Laguerre function of order n:

$$q_n(z) = \frac{e^{-z/2}}{n!} L_n(z), \tag{25}$$

where $n = 0, 1, 2, 3 \ldots$ and

$$L_n(z) = n!\left[1 - nz + \frac{n(n-1)}{(2!)^2} z^2 - \frac{n(n-1)(n-2)}{(3!)^2} z^3 + \ldots (-1)^r \frac{n(n-1)\ldots(n-r+1)}{(r!)^2} z^r + \ldots \frac{(-1)^n z^n}{n!}\right]. \tag{26}$$

Note that for $z = 0$, $L_n = n!$; consequently $q_n(0) = 1$ for all n.

The Laguerre polynomials, $L_n(z)$, satisfy the differential equation

$$z\frac{d^2L_n}{dz^2} + (1 - z)\frac{dL_n}{dz} + nL_n = 0. \tag{27}$$

If the function $q_n(2|k|x)$ is substituted for Z in (22), the latter reduces to (27) provided that

$$\kappa = (2n + 1)|k|. \tag{28}$$

This is the characteristic equation to be satisfied by normal modes and it yields the allowable values of κ and hence ω for a given longshore wave number k. Note that there is no effect of Coriolis force on the surface form of the edge wave modes. However, the flow associated with these waves is definitely influenced by Coriolis force, as is evident from (20) and (21). The fundamental waves are characterized by an exponentially decaying amplitude of the surface with increasing x (Fig. 1), while the higher order modes are characterized by n discrete nodal lines offshore; beyond the nth nodal line the amplitude decays monotonically as $(2|k|x)^n e^{-|k|x}$. Tables of the Laguerre functions through order 7 are given by Eckart (1934).

The Laguerre functions form an orthonormal set in the sense that

$$\int_0^\infty q_n(z)q_m(z)\,dz = \begin{cases} 0 \text{ for } n \neq m \\ 1 \text{ for } n = m \end{cases}, \tag{29}$$

where m is a positive integer or zero (Courant and Hilbert, 1931: 79–82). Later on we shall note a more general orthogonality property

of normal mode functions which is useful in establishing the formal solution of the forced wave problem.

2. Edge Wave Frequencies. By employing (23) we may write the characteristic relation (28) in the form

$$\omega^3 - [f^2 + (2n + 1)gs|k|]\omega + gskf = 0. \tag{30}$$

For any given order, n, and wave number, k, there are *three* allowable values of ω. The admissible frequency functions will be denoted by $\omega_{jn}(k)$, where $j = 1, 2, 3$ denotes the three different *modes* corresponding to each *order* n. An examination of the cubic equation (30) reveals that the roots $\omega_{jn}(k)$ are real and have the following general properties:

$$\omega_{jn}(-k) = -\omega_{jn}(k), \tag{31}$$

$$\omega_{1,n} + \omega_{2,n} + \omega_{3,n} = 0, \tag{32}$$

and

$$\omega_{1,n}\omega_{2,n}\omega_{3,n} = -gskf. \tag{33}$$

It is evident from (32) and (33) that two of the roots are positive and one is negative for each mode, if kf is positive. Furthermore, the $\omega_{jn}(k)$ functions are antisymmetric with respect to k, which indicates that the phase velocities $-\omega_{nj}/k$ are independent of the sign of k. Accordingly we can confine our attention to the case of positive k alone. Finally we will adopt $\omega_{1,n}$ as the negative root, corresponding to waves which move in the positive y direction.

For the fundamental mode ($n = 0$), relation (30) can be factored such that for positive k:

$$(\omega - f)[\omega(\omega + f) - gsk] = 0. \tag{34}$$

Consequently

$$\omega_{1,0} = -\tfrac{1}{2}f - \sqrt{gsk + \tfrac{1}{4}f^2}, \tag{35}$$

$$\omega_{2,0} = -\tfrac{1}{2}f + \sqrt{gsk + \tfrac{1}{4}f^2}, \tag{36}$$

$$\omega_{3,0} = f. \tag{37}$$

Relations (20) and (21) are indeterminate for the case of $\omega = f$, and an analysis of (15) to (17) for this case indicates that the only meaningful solutions satisfying conditions (18) and (19) occur for $k = 0$ and $k = 2f^2/gs$. The first of these cases, the standing inertial mode discussed earlier, is a limiting case of the higher order waves of mode $j = 2$; the other is a special case of the fundamental waves of mode $j = 2$. Thus

for the fundamental edge waves, only the modes $j = 1, 2$ need be considered.

Note that, for no rotation of the earth, $\omega = \pm \sqrt{gsk}$ for the fundamental mode. This corresponds to the frequency of Stokes edge waves for sufficiently small bottom slope. However, in the presence of rotation, the frequencies $\omega_{1,0}$ and $\omega_{2,0}$ differ in magnitude by f; hence the phase speeds for waves moving to right or left along shore differ by f/k for the fundamental mode.

It is usually convenient to express the frequency in terms of wave period $T_{jn} = 2\pi/|\omega_{jn}|$. The periods corresponding to $\omega_{1,0}$ and $\omega_{2,0}$, as evaluated from (35) and (36) for several different values of longshore wave length (λ), are given in Table I based upon a latitude of 45° and $s = 10^{-3}$ (about 1 fathom per nautical mile). The period as computed for the case of no rotation, $T_0 = (2\pi/\sqrt{gsk})$, is tabulated for comparison. The last column gives the percent difference between periods of waves moving to right and left. As we should expect, the greatest difference occurs for the longest waves, those for which T_0 approaches or exceeds the pendulum period $(2\pi/f)$; the influence of the earth's rotation is essentially negligible for periods less than one hour.

As applied to the east coast of the United States, taking $s = 10^{-3}$, the fundamental edge waves of 1000 km wave length would have a period of 5.70 hours if traveling north, or a period of 8.63 hours if traveling south. Munk, *et. al.* (1956) have suggested that edge waves of about 5 to 6 hour period can be generated by hurricanes moving northward along the east coast. The present analysis indicates that the Coriolis force can have a significant influence on the characteristics of fundamental edge waves of this period.

TABLE 1.—Periods of the fundamental mode ($n = 0$) for 45° latitude $\left(\frac{2\pi}{f} = 17 \text{ hrs}\right)$

	With Rotation		*No Rotation*	
λ (*km*) for $s = 10^{-3}$	$T_{1,0}$ (*hrs*)	$T_{2,0}$ (*hrs*)	T_0 (*hrs*)	$\frac{T_{2,0} - T_{1,0}}{T_0}$ (%)
10	0.690	0.718	0.703	4
100	2.08	2.37	2.22	13
1000	5.70	8.63	7.03	42
10,000	12.0	41.2	22.2	132

The general roots of (30) for the higher order edge waves ($n \geq 1$) are given by

$$\omega_{jn} = -\frac{2}{\sqrt{3}} f \sqrt{1 + (2n + 1)gsk/f^2} \cos [\beta + (j - 1)2\pi/3], \quad (38)$$

where

$$\cos 3\beta = \frac{3}{2}\sqrt{3}\,\frac{gsk}{f^2}\,[1 + (2n + 1)gsk/f^2]^{-3/2}. \tag{39}$$

The asymptotic behavior of the functions $\omega_{jn}(k)$ for very small k and very large k is indicated in Table II for all n. The frequency functions are also illustrated in Figs. 2 and 3. In the logarithmic plot (Fig. 3), only modes $j = 2, 3$ are shown; ω_{1n} can be computed readily by using (32).

The function $|\omega_0/f| = \sqrt{gsk/f^2}$ representing the relative frequency of Stokes edge wave is shown by the dashed curve in both figures, for comparison. It is of interest to note that the fundamental mode for

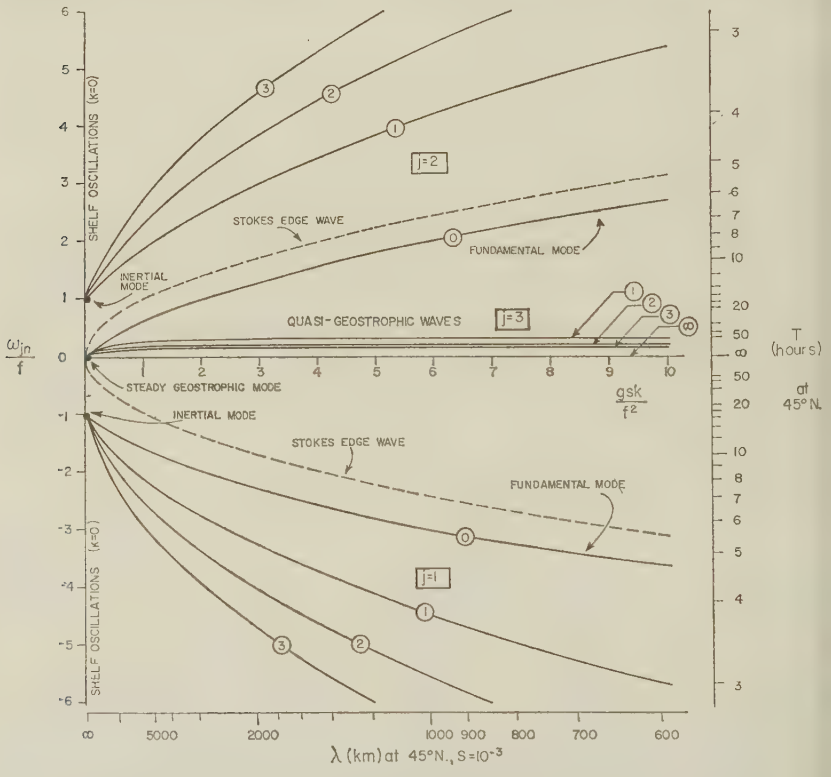

Figure 2. Relative values of the characteristic frequency functions, $\omega_{jn}(k)/f$, versus relative wave number, gsk/f^2 (dimensionless); the different orders n are indicated by the numbers in circles; the mode $j = 1$ represents waves progressing in the positive y direction (*e.g.*, northward along the east coast of a continent in the northern hemisphere). Auxiliary scales for period and wave length corresponding to 45° latitude and $s = 10^{-3}$ are shown for convenience.

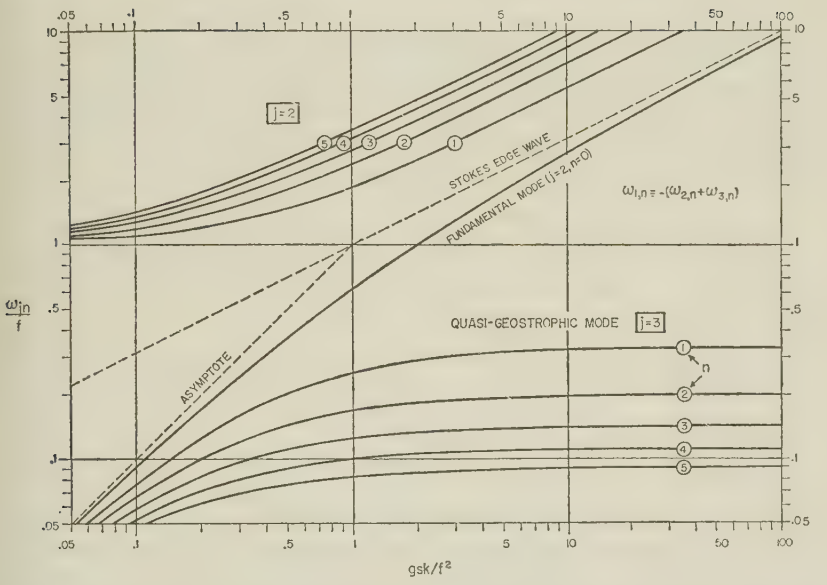

Figure 3. Relative frequencies $\omega_{jn}(k)/f$ versus gsk/f^2 for modes 2 and 3 on a log-log plot; this figure emphasizes the peculiar behavior of the fundamental wave (for $j = 2$) relative to the higher order waves of modes 2 and 3. Note that modes 2 and 3 correspond to waves progressing in the negative y direction.

$j = 2$ is really in a class apart from the other waves; for large k it behaves like Stokes wave but for very small k it behaves like the higher order quasigeostrophic modes (see Fig. 3 or Table II). On the other hand, the fundamental mode for $j = 1$ behaves like an inertial oscillation with frequency f for very small k.

For all n, the modes $j = 1, 2$ behave like purely gravitational edge waves if k is sufficiently large. Ursell (1952) obtained the result

$$\omega = \pm \sqrt{gk \sin (2n + 1)\alpha}, \tag{40}$$

where α is the angular inclination of the sea bed in radians. If $(2n + 1)\alpha \ll 1$, then (40) reduces to the asymptotic expressions given in Table II for $j = 1, 2$ and large k, since in this case α and s are essentially the same. An interesting feature of Ursell's analysis is that it predicts an upper limit on n, corresponding to $(2n + 1)\alpha \simeq \pi/2$. However, even for $s = 10^{-2}$ the maximum n is well over 70.

The mode $j = 3$, which exists for the higher order waves ($n \geq 1$), represents an entirely different class of waves. The frequency of these waves is very small ($< f$) for all values of k and, as will be shown presently, they are characterized by quasigeostrophic flow and rela-

tively large vorticity. The counterpart of this class of disturbance in the case of $f = 0$ is a steady vortex mode with no surface distortion. The quasigeostrophic waves ($j = 3$) propagate only in the negative y direction in the northern hemisphere (for example, to the south along the east coast of the United States). In this respect they are analogous to Kelvin boundary waves (Proudman, 1953: 253–255).

TABLE II. Asymptotic expressions for the frequencies $\omega_{jn}(k)$

Condition	*Order*	*Mode* $j = 1$	$j = 2$	$j = 3$
$k \ll \frac{f^2}{(2n+1)gs}$	$n = 0$	$-\left[f + \frac{gsk}{f}\right]$	$\frac{gsk}{f}$	(f)
	$n \geqslant 1$	$-\left[f + (n+1)\frac{gsk}{f}\right]$	$\left[f + n\frac{gsk}{f}\right]$	$\frac{gsk}{f}$
$k \gg \frac{f^2}{(2n+1)gs}$	$n \geqslant 0$	$-\sqrt{(2n+1)gsk}$	$\sqrt{(2n+1)gsk}$	$\frac{f}{(2n+1)}$

3. Group Velocity and Dispersive Properties. In a study of non-periodic free waves emerging from some initially localized disturbance (*e.g.*, the Cauchy-Poisson problem; Lamb, 1932: 384–391), the group velocity, $-d\omega/dk$, is of importance since it is essentially a measure of the rate of propagation of a given segment of the energy spectrum. The dependence of group velocity on k consequently governs the dispersion or resolution of the resulting wave train. Using (30), the following formula is obtained for the group velocity for $k > 0$ and $n \geqslant 1$:

$$G_{jn}(k) = -\frac{d\omega_{jn}}{dk} = \frac{-gs[2n+1)\omega_{jn} - f]}{[3\omega^2{}_{jn} - f^2 - (2n+1)gsk]}. \tag{41}$$

For the special case $n = 0$, (35) and (36) yield directly

$$G_{j,0}(k) = \pm \frac{gs}{\sqrt{4gsk + f^2}} \tag{42}$$

for $j = 1, 2$ respectively. Thus the group velocity of the two fundamental modes are equal in magnitude even though the phase speeds differ.

It follows from (42) that the group velocity of the fundamental edge waves cannot exceed gs/f. For the higher order modes, the maximum group velocity is $(n+1)gs/f$, corresponding to the $j = 1$ modes for $k \to 0$. For $s = 10^{-3}$, the maximum group velocity of the fundamental waves is about 100 m/sec at midlatitudes and corresponds to about half the speed of a tsunami in the open ocean.

TABLE III. Asymptotic expressions for the group velocities $G_{jn}(k)$

Condition	*Order*	*Mode* $j = 1$	$j = 2$	$j = 3$
$k \ll \dfrac{f^2}{(2n+1)gs}$	$n = 0$	$\dfrac{gs}{f}\left(1 - 2\dfrac{gsk}{f^2}\right)$	$-\dfrac{gs}{f}\left(1 - 2\dfrac{gsk}{f^2}\right)$	(0)
	$n \geqslant 1$	$(n+1)\dfrac{gs}{f}\left[1 - (n+2)\dfrac{gsk}{f^2}\right]$	$-n\dfrac{gs}{f}\left[1 - (n-1)\dfrac{gsk}{f^2}\right]$	$-\dfrac{gs}{f}\left[1 - 2(2n+1)\dfrac{gsk}{f^2}\right]$
$k \gg \dfrac{f^2}{(2n+1)gs}$	$n = 0$	$\frac{1}{2}\sqrt{\dfrac{gs}{k}}$	$-\frac{1}{2}\sqrt{\dfrac{gs}{k}}$	(0)
	$n \geqslant 1$	$\frac{1}{2}\sqrt{\dfrac{(2n+1)gs}{k}}$	$-\frac{1}{2}\sqrt{\dfrac{(2n+1)gs}{k}}$	$-\dfrac{f^3}{(2n+1)^2gsk^2}$

The asymptotic expressions for group velocity are listed in Table III, and a plot of the group velocity as a function of k for $n = 0, 1, 2$ and $j = 2, 3$ is shown in Fig. 4. It is evident that the group velocity of the quasigeostrophic mode is practically zero for $k > 2f^2/gs$. This implies that the propagation of wave energy away from an initially localized disturbance is principally due to the ordinary edge wave modes $j = 1, 2$, unless the wave spectrum contains a preponderance of energy in the range $0 < k \ll 2f^2/gs$.

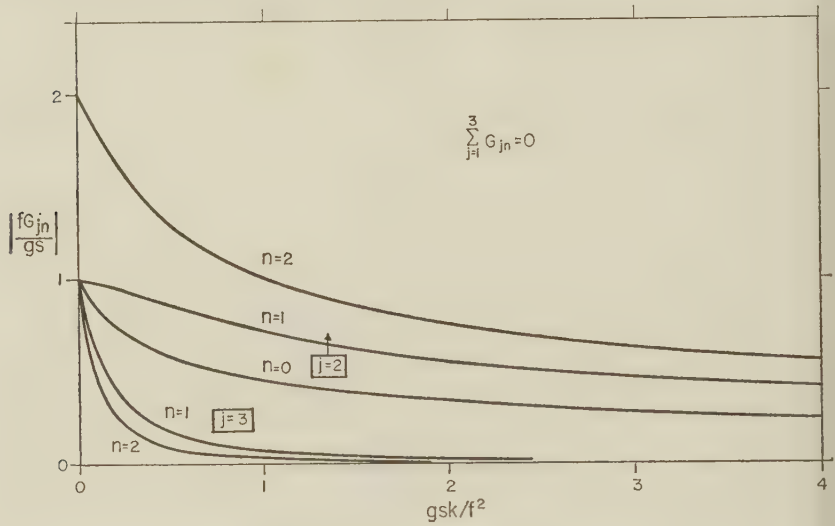

Figure 4. Relative group velocity $|G_{jn}f/gs|$ versus gsk/f^2 for modes 2 and 3 and orders 0, 1, 2. Note that $G_{1,n}$ is readily obtained by the expression $|G_{2,n} + \frac{f}{s}G_{1,n}|$.

KINEMATIC BEHAVIOUR OF THE EDGE WAVE MODES

1. Character of the Fluid Flow. Hereafter we will employ the following notation for the normal mode flow and elevation functions:

$$U_{jn}(x, y, t; k) = X_{jn}(kx) \exp [iky + i\omega_{jn}(k)t], \quad (43$$

$$V_{jn}(x, y, t; k) = Y_{jn}(kx) \exp [iky + i\omega_{jn}(k)t], \quad (44$$

$$H_{jn}(x, y, t; k) = Z_n(kx) \exp [iky + i\omega_{jn}(k)t]. \quad (45$$

For each of the three frequency modes ($j = 1, 2, 3$) there is a corresponding set of eigenfunctions; however, all three modes have $Z_n(kx)$ in common.

For convenience we will take the amplitude of the surface disturbance at $x = 0$ as unity, so that $Z_n(kx) = q_n(2|k|x)$. By employ

ng the appropriate recursion formulas for the Laguerre polynomials (Courant and Hilbert, 1931: 79–80), we then find from (20) and (21) or $k \geqslant 0$, $n \geqslant 1$:

$$X_{jn}(kx) = -igs\left\{\frac{kxZ_n(kx)}{(\omega_{jn}+f)} - \frac{n\omega_{jn}}{(\omega^2{}_{jn}-f^2)}[Z_n(kx)-Z_{n-1}(kx)]\right\}, \quad (46)$$

$$Y_{jn}(kx) = -gs\left\{\frac{kxZ_n(kx)}{(\omega_{jn}+f)} + \frac{nf}{(\omega^2{}_{jn}-f^2)}[Z_n(kx)-Z_{n-1}(kx)]\right\}, \quad (47)$$

$$Z_n(kx) = \frac{e^{-kx}}{n!}L_n(2kx). \quad (48)$$

n the case of the fundamental mode for $k \geqslant 0$ and $j = 1, 2$ the follow-ng eigenfunctions apply:

$$X_{j,0}(kx) = -\frac{igskx}{(\omega_{j,0}+f)}e^{-kx}, \quad (49)$$

$$Y_{j,0}(kx) = -\frac{gskx}{(\omega_{j,0}+f)}e^{-kx}, \quad (50)$$

nd

$$Z_0(kx) = e^{-kx}. \quad (51)$$

t can be shown, from a separate analysis for negative k, that X_{jn} is an dd function with respect to k and that Y_{jn} and Z_n are even.

In general the component of flow U_{jn} is $\pi/2$ radians out of phase vith the V_{jn} component and the latter is in phase with the water level. Furthermore, the amplitudes of U_{jn} and V_{jn} differ in magnitude for $\geqslant 1$; thus, in the Lagrangian system, the paths of the water par-icles describe ellipses in a nearly horizontal plane. However, in the ase of the fundamental mode, we note from (49) and (50) that the x nd y components of flow are of equal amplitude, and hence the hori-ontal projections of the particle orbits are circular. The orbit radius, , at a given mean position offshore, can be evaluated by integrating $U_{j,0}/h$ or $V_{j,0}/h$ with respect to t and by using (34); the result is

$$r| = \frac{1}{s}e^{-|k|x} \quad (52)$$

or unit amplitude at shore.

Both components of volume transport vanish at the water's edge. Iowever, the components of fluid velocity U_{jn}/h and V_{jn}/h do not anish at this position. It is simple to evaluate these components for ne fundamental waves, but in the case of the higher order waves we

must consider the limit of $(Z_n - Z_{n-1})/kx$ as $kx \to 0$. Making use of (30), the result is for all j, n, k:

$$\left[\frac{U_{jn}}{h}\right]_{x=0} = -i\,\frac{\omega_{jn}}{s}\,e^{i(ky+\omega_{jn}t)}, \tag{53}$$

$$\left[\frac{V_{jn}}{h}\right]_{x=0} = \frac{\omega_{jn}}{s}\left[\frac{(2n+1)f - \omega_{jn}}{(2n+1)\omega_{jn} - f}\right] e^{i(ky+\omega_{jn}t)}. \tag{54}$$

As a check, we note that the amplitude of horizontal excursion of the water's edge, as obtained from the integral of (53) with respect to t, is simply $1/s$. This must be the case in the linear approximation with unit amplitude of Z_n at shore. The longshore excursion of the fluid particles at the water's edge has an amplitude $\leqslant 1/s$ for modes $j = 1, 2$, but for $j = 3$ the amplitude of longshore excursion is much greater than $1/s$.

An interesting feature worth noting is that, although the amplitudes of flow are different for the $j = 1$ and $j = 2$ modes of the fundamental edge wave on a rotating earth, the orbit radii are the same at a given position offshore. From (49) and (50), using (35) and (36), it follows that the fundamental waves which move in the positive y direction ($j = 1$) are associated with a greater magnitude of flow than the fundamental waves which move in the opposite sense, assuming the same wave length and water level amplitude at shore for both.

In the case of the $j = 3$ modes, the frequency is much less than f for all k, and since $|dZ_n/dx|$ is of the order $|(2n+1)kZ_n|$, it follows from (21) that

$$Y_{3,n}(kx) \simeq \frac{gsx}{f}\,\frac{dZ_n}{dx}. \tag{55}$$

Thus the longshore flow is in quasigeostrophic balance with the offshore slope of the sea surface for any k associated with this mode. The fundamental waves for mode $j = 2$ also have this property when k is sufficiently small ($\ll f^2/gs$). It is of interest that the quasigeostrophic character applies only to waves propagating in the negative y sense.

2. Vorticity and Divergence. We can gain a greater appreciation of the distinction in kinematic behavior of various edge wave modes by investigating the vorticity and divergence of these waves. It may be remarked that one of the outstanding features of Stokes edge waves, which sets them apart from all other surface gravity waves, is that they are *horizontally divergenceless*. This unusual property is possible only in the presence of the sloping sea bed; the variations in the surface elevation can be regarded, in the Lagrangrian sense, as being associated

with the onshore or offshore displacements of a column of sea water (of fixed height) along the sloping bed. Thus the rate of rise or fall of sea level is directly proportional to the onshore or offshore component of horizontal velocity of the water for a given bottom slope.

The vertical component of vorticity in Stokes edge waves is also zero. The irrotational and horizontally divergenceless property of the fundamental mode is not modified by the presence of the earth's rotation (the vorticity relative to the earth being zero). However, the higher order waves of both classes do possess vorticity and horizontal divergence. As we shall see presently, this property is important in determining the excitation of higher order edge waves by wind stress.

The vertical component of relative vorticity, ζ, and the horizontal divergence, D, are defined respectively by

$$\zeta = \frac{\partial v}{\partial x} - \frac{\partial u}{\partial y} \tag{56}$$

and

$$D = \frac{\partial u}{\partial x} + \frac{\partial v}{\partial y}, \tag{57}$$

where $u = U/h$ and $v = V/h$, representing the vertically averaged components of fluid velocity. Using (43), (44) and (46) to (48), it can be shown that for any normal mode

$$\zeta_{jn}(x, y, t; k) = \frac{4gfk^2}{(\omega^2_{jn} - f^2)} \frac{e^{-k|x}}{n!} \left[\frac{nL_n(2|k|x) + L'_n(2|k|x)}{(2|k|x)} \right] \times \exp [iky + i\omega_{jn}(k)t] \tag{58}$$

and

$$D_{jn}(x, y, t; k) = -i \frac{\omega_{jn}}{f} \zeta_{jn}(x, y, t; k), \tag{59}$$

where

$$L'_n(z) = dL_n(z)/dz.$$

Note first of all that, for the fundamental mode, $L_0(z)$ is unity for all z, and $L'_0(z)$ vanishes identically; consequently

$$\zeta_{j,0}(x, y, t; k) = D_{j,0}(x, y, t; k) = 0, \tag{60}$$

as in the case of Stokes edge wave. For the higher modes we find from the properties of the Laguerre polynomial (26) that the amplitudes of the vorticity and divergence at $x = 0$ are respectively

$$\bar{\zeta}_{jn}(k) = \frac{2n(n+1)gfk^2}{|\omega^2{}_{jn} - f^2|} \tag{61}$$

and

$$\bar{D}_{jn}(k) = \frac{2n(n+1)g|\omega_{jn}|k^2}{|\omega^2{}_{jn} - f^2|}. \tag{62}$$

The asymptotic expressions for $\bar{\zeta}_{jn}$ and $\bar{D}_{jn}$ are given in Tables IV and V respectively. It is evident that the $j = 3$ mode is quite differen from the other two; if we allow $f \to 0$, then the vorticity of the $j = 1, 2$ modes vanishes while that of the $j = 3$ mode increases without bound However, it should be recalled that a unit amplitude of H_{jn} is pre sumed. Thus a finite vorticity of the $j = 3$ mode can exist for $f = 0$ if there is no surface distortion; this is the vortex flow referred t earlier. Another point worthy of note is that the vorticity of the $j =$ 3 mode is virtually independent of the bottom slope s.

TABLE IV. ASYMPTOTIC EXPRESSIONS FOR THE VORTICITY AMPLITUDE AT SHOR $\bar{\zeta}_{jn}(k)$ FOR $n \geqslant 1$

Condition	*Mode* $j = 1$	$j = 2$	$j = 3$
$k \ll \frac{f^2}{(2n+1)gs}$	$\frac{nfk}{s}$	$\frac{(n+1)fk}{s}$	$2n(n+1)\frac{gk^2}{f}$
$k \gg \frac{f^2}{(2n+1)gs}$	$\frac{2n(n+1)}{(2n+1)}\frac{fk}{s}$	$\frac{2n(n+1)}{(2n+1)}\frac{fk}{s}$	$\frac{(2n+1)^2}{2}\frac{gk^2}{f}$

TABLE V. ASYMPTOTIC EXPRESSIONS FOR THE DIVERGENCE AMPLITUDE AT SHOR $\bar{D}_{jn}(k)$ FOR $n \geqslant 1$

Condition	*Mode* $j = 1$	$j = 2$	$j = 3$
$k \ll \frac{f^2}{(2n+1)gs}$	$\frac{nfk}{s}$	$\frac{(n+1)fk}{s}$	$2n(n+1)\frac{sg^2k^2}{f^3}$
$k \gg \frac{f^2}{(2n+1)gs}$	$\frac{2n(n+1)}{\sqrt{2n+1}}\sqrt{\frac{gk^3}{s}}$	$\frac{2n(n+1)}{\sqrt{2n+1}}\sqrt{\frac{gk^3}{s}}$	$\frac{(2n+1)}{2}\frac{gk^2}{f}$

THE FORCED WAVE PROBLEM

1. Formal Solution of the Forced and/or Initial Value Problem The system of equations (15) to (19), which define the eigenfunction of the problem, also require an orthogonality condition among th eigenfunctions in the generalized Hilbert sense. This condition i

$$\int_0^\infty \left\{ \frac{1}{gsx} \left[X^*_{jn}(kx) X_{pm}(kx) + Y^*_{jn}(kx) Y_{pm}(kx) \right] + Z^*_n(kx) Z_m(kx) \right\} dx = \begin{cases} 0 & \text{if } p \neq j \text{ or } m \neq n \\ N_{jn}(k) & \text{if } p = j \text{ and } m = n \end{cases}, \tag{63}$$

where the asterisk denotes the complex conjugate (for proof, see Appendix A). The quantity $N_{jn}(k)$ is the norm of the set of eigenfunctions; it has positive real values for all k and is closely related to the energy of the normal modes. Using (20) to (22) together with (29) and (30) it can be shown (but not easily) that

$$N_{jn}(k) = \left| \frac{2\omega^3_{jn} - gskf}{2k\omega_{jn}(\omega^2_{jn} - f^2)} \right|. \tag{64}$$

In the absence of f, $N_{jn}(k)$ reduces to $1/|k|$ for all j, n.

The formal solution for Q_x, Q_y and η of the original problem stipulated by (1) to (6) can be represented by suitable linear combinations of the corresponding normal mode functions U_{jn}, V_{jn} and H_{jn}, respectively. Now, since the latter functions must have a common complex amplitude for a given j, n, k, it follows that the general solutions, incorporating the complete set of edge wave modes for all possible k, must be of the form

$$Q_x(x, y, t) = \sum_{j=1}^{3} \sum_{n=0}^{\infty} \int_{-\infty}^{\infty} A_{jn}(k, t) U_{jn}(x, y, t; k)\, dk, \tag{65}$$

$$Q_y(x, y, t) = \sum_{j=1}^{3} \sum_{n=0}^{\infty} \int_{-\infty}^{\infty} A_{jn}(k, t) V_{jn}(x, y, t; k)\, dk, \tag{66}$$

$$\eta(x, y, t) = \sum_{j=1}^{3} \sum_{n=0}^{\infty} \int_{-\infty}^{\infty} A_{jn}(k, t) H_{jn}(x, y, t; k)\, dk, \tag{67}$$

where the set of (complex) functions $A_{jn}(k, t)$ represent collectively the *amplitude* spectrum of the disturbance (with respect to j, n, k).

In view of the orthogonality condition (63), together with (1) to (11), it can be shown that

$$A_{jn}(k, t) = a_{jn}(k) + \int_0^t M_{jn}(k, t')\, dt', \tag{68}$$

where

$$a_{jn}(k) = \frac{1}{2\pi N_{jn}(k)} \int_{-\infty}^{\infty} dy \int_0^\infty \left\{ \frac{1}{gsx} \left[X^*_{jn}(kx) Q_x(x, y, 0) + Y^*_{jn}(kx) Q_y(x, y, 0) \right] + Z^*_n(kx) \eta(x, y, 0) \right\} e^{-iky}\, dx \tag{69}$$

and

$$M_{jn}(k, t) = \frac{1}{2\pi N_{jn}(k)} \int_{-\infty}^{\infty} dy \int_{0}^{\infty} \left\{ \frac{1}{gsx} [U^*_{jn}(x, y, t; k) F_x(x, y, t) + V^*_{jn}(x, y, t; k) F_y(x, y, t)] \right\} dx. \tag{70}$$

The derivation of these last three relations is outlined in Appendix B. The function $a_{jn}(k)$ represents that part of the amplitude spectrum governed by the initial conditions of flow and water level; $M_{jn}(k, t)$ on the other hand is determined by the forcing functions alone and will be referred to hereafter as the *excitation*. Note that the excitation represents the time rate of change of the amplitude spectrum.

If we relax condition (5) by allowing a nonuniform line source $Q_x(0, y, t)$ at the water's edge (representing a localized land drainage), then we must add a third function, $B_{jn}(k, t)$, on the right-hand side of (68). It is shown in Appendix B that the contribution to the amplitude spectrum by the volume source is

$$B_{jn}(k, t) = \frac{1}{2\pi N_{jn}(k)} \int_{0}^{t} dt' \int_{\infty}^{\infty} H^*(0, y, t'; k) Q_x(0, y, t') \, dy. \tag{71}$$

The effect of localized land drainage is probably of secondary importance, but it may be significant near river mouths during times of exceptional flood stage.

It may be remarked that, in view of the behaviour of the functions X_{jn}, Y_{jn}, Z_n and ω_{jn} for negative k, the real part of A_{jn} is even in k while the imaginary part is odd, thus assuring real values of the outputs of operations (65) to (67). The imaginary part vanishes identically in the integration over all k. Thus we need consider only the *real* parts of the integrands of (65) to (67); furthermore, if we restrict k to positive values only, then the integration over all k can be replaced by *twice* the integral over all *positive* k.

2. Energy Spectrum. The total kinetic and potential energy of the disturbance at any instant is defined by

$$E(t) = \frac{1}{2} \rho \int_{-\infty}^{\infty} dy \int_{0}^{\infty} \left[\frac{Q_x^2 + Q_y^2}{h} + g\eta^2 \right] dx. \tag{72}$$

This can be transformed to a convenient form involving $A_{jn}(k, t)$ as follows: multiply (65), (66) and (67) by Q_x/h, Q_y/h and $g\eta$, respectively; add the resulting equations and substitute in the integrand of (72); then change the order of integration and summation and apply the

complex conjugate counterpart of (101) as given in Appendix B; this yields

$$E(t) = 2\pi\rho g \sum_{j=1}^{3} \sum_{n=0}^{\infty} \int_0^\infty N_{jn}(k) A_{jn}(k, t) A_{jn}^*(k, t)\, dk, \tag{73}$$

which is an analogue of Parseval's theorem. Except for the factor $2\pi\rho g$, the *spatial* energy spectrum is given by

$$S_{jn}(k, t) = N_{jn}(k) |A_{jn}(k, t)|^2. \tag{74}$$

3. Initially Static Mound of Water. If we are interested in the dispersion of free edge waves from an *initially static* mound of water, then the amplitude spectrum is simply $a_{jn}(k)$, which is invariant in time, and from (69) we find

$$a_{jn}(k) = p_{jn}(k) \frac{1}{\pi} \int_{-\infty}^{\infty} dy \int_0^\infty Z_n(kx) \eta(x, y, 0) e^{-iky}\, d|kx|, \tag{75}$$

where

$$p_{jn}(k) = \frac{1}{2|k| N_{jn}(k)}. \tag{76}$$

The latter function has the convenient property that

$$\sum_{j=1}^{3} p_{jn}(k) = 1. \tag{77}$$

The spectral distribution in respect to n and k is determined largely by the form of $\eta(x, y, 0)$. However, the partitioning of the energy spectrum among the three discrete modes ($j = 1, 2, 3$) is determined entirely by the weight function $p_{jn}(k)$ for an initially static mound of water, since

$$S_{jn} = p_{jn} \sum_{j=1}^{3} S_{jn}$$

in this case. Graphs of the weight functions $p_{jn}(k)$ for some selected values of n are shown in Fig. 5. Modes 1 and 2 are shown for the fundamental ($p_{3,0}$ being identically zero), modes 1 and 3 for the higher order waves. The asymptotic expressions for $p_{jn}(k)$ are listed in Table VI. For the particular case of the fundamental mode

$$p_{j,0}(k) = \frac{1}{2}\left[1 \mp \frac{1}{\sqrt{1 + 4gsk/f^2}}\right], \tag{78}$$

for $j = 1, 2$ respectively.

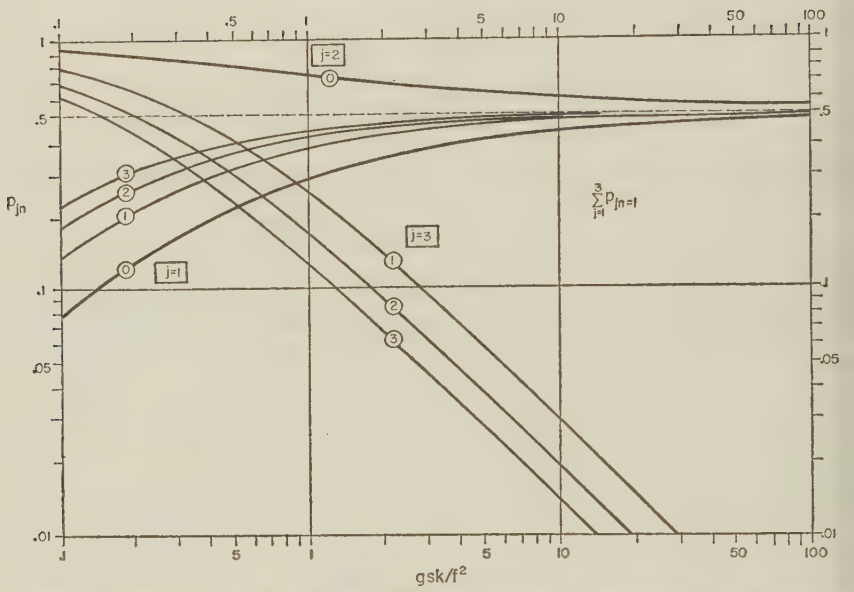

Figure 5. Weight functions $p_{jn}(k)$ versus gsk/f^2 on a log-log plot. Note that only the fundamental is shown for mode 2. Values of n are shown circled.

Inspection of Fig. 5 reveals that $p_{1,n} < \frac{1}{2}$ for finite k, hence we must conclude that rotation of the earth favors dispersal of energy of an initially static deformation towards the negative y direction (to the south along the east coast of the United States). This effect is most pronounced of course for the longest waves; for the shorter waves the energy is propagated nearly equally in both directions. The quasi-geostrophic mode can contribute about 10% or more to the spectral energy for a given n and k if $(2n + 1)gsk < 9f^2$. For $n = 1$, $s = 10^{-3}$, this would require an initial disturbance with an effective scale of the order of 2000 km or greater.

TABLE VI. Asymptotic expressions for the weight functions $p_{jn}(k)$

Condition	*Order*	*Mode* $j = 1$	$j = 2$	$j = 3$
$k \ll \dfrac{f^2}{(2n+1)gs}$	$n = 0$	$\dfrac{gsk}{f^2}$	$1 - \dfrac{gsk}{f^2}$	0
	$n > 1$	$(n+1)\dfrac{gsk}{f^2}$	$n\dfrac{gsk}{f^2}$	$1 - (2n+1)\dfrac{gsk}{f^2}$
$k \gg \dfrac{f^2}{(2n+1)gs}$	$n = 0$	1/2	1/2	0
	$n \geqslant 1$	1/2	1/2	$\dfrac{f^2}{(2n+1)gsk}$

4. Some General Considerations of Forced Edge Waves. If we suppose that the force field is nil for $t \leqslant 0$ and that the water is initially undisturbed, then, except for the possibility of a volume source at shore (which shall be ignored), the amplitude spectrum is determined entirely by the space-time distribution of the forcing functions for a given bottom slope. As stated at the outset, we will regard the force field for $t \geqslant 0$ to be localized such that F_x and F_y vanish at infinity.

The vector-forcing function $\mathbf{F}$ (of which F_x and F_y are components) is determined by the surface wind stress, τ, and the atmospheric pressure, P, by the relation

$$\mathbf{F} = \frac{1}{\rho}[-h\nabla P + \tau], \tag{79}$$

where ∇ is the two-dimensional gradient operator in the x, y-plane. Using (70), the excitation can consequently be separated into two parts, $M_{jn}^{(p)}[k, t]$ and $M_{jn}^{(\tau)}[k, t]$, related to pressure and stress respectively. Thus

$$M_{jn}[k, t] = M_{jn}^{(p)}[k, t] + M_{jn}^{(\tau)}[k, t], \tag{80}$$

where

$$M_{jn}^{(p)}[k, t] = \frac{1}{2\pi\rho g N_{jn}(k)} \int_{-\infty}^{\infty} dy \int_{-\infty}^{\infty} \left[U_{jn}^* \frac{\partial P}{\partial x} + V_{jn}^* \frac{\partial P}{\partial y} \right] dx \tag{81}$$

and

$$M_{jn}^{(\tau)}[k, t] = \frac{1}{2\pi\rho N_{jn}(k)} \int_{\infty}^{\infty} dy \int_{-\infty}^{\infty} \left[\frac{U_{jn}^* \tau_x + V_{jn}^* \tau_y}{gsx} \right] dx. \tag{82}$$

In the above relations the functional dependence notation is dropped for the sake of brevity.

Relation (81) can be transformed to a more convenient form if we employ integration by parts, bearing in mind that U_{jn}^* vanishes at $x = 0$ and that the departure of pressure from normal, P', approaches zero as x and $|y| \to \infty$. Furthermore, if we make use of the conjugate counterparts of (9) and (45), we find that

$$M_{jn}^{(p)}[k, t] = \frac{ikp_{jn}\omega_{jn}}{\pi\rho g} \int_{-\infty}^{\infty} dy \int_{0}^{\infty} H_{jn}^*(x, y, t; k) P'(x, y, t)\, dx. \tag{83}$$

The excitation of edge waves by atmospheric pressure has been dealt with at some length by Greenspan (1956). His analysis for a storm moving parallel to the coast indicates that, for a Gaussian distribution of P', it is primarily the fundamental mode which is excited (at least for distributions in which the horizontal scale is comparable

to that of a typical hurricane). Furthermore, the greatest effect occurs when the path of the low pressure center is close to the coast. These results, insofar as P' alone is concerned, should apply equally well for the inertiogravitational edge waves considered here, since the integral involved in (83) is independent of f. It need only be remarked in passing that the partitioning of the energy of the fundamental waves to modes $j = 1$ and 2 is governed, at least in part, by $p_{j,0}(k)$. The implications of this are explored in some detail by Kajiura (1958).

In the remaining discussion we turn our attention to the question of excitation of edge waves by wind stress. There are two different transformations of (82) which will be considered. The first involves the divergence and curl of the wind stress and the second involves the divergence and vorticity of the normal mode flow.

If we employ the conjugate counterparts of (7) and (8) and keep in mind the periodic character of the normal modes, we find that

$$U_{jn}^* = \frac{gsx}{(\omega_{jn}^2 - f^2)}\left[-i\omega_{jn}\frac{\partial H_{jn}^*}{\partial x} + f\frac{\partial H_{jn}^*}{\partial y}\right] \tag{84}$$

and

$$V_{jn}^* = \frac{gsx}{(\omega_{jn}^2 - f^2)}\left[-i\omega_{jn}\frac{\partial H_{jn}^*}{\partial y} - f\frac{\partial H_{jn}^*}{\partial x}\right]. \tag{85}$$

Substituting (84) and (85) in relation (82) and integrating by parts, using the condition that τ vanishes as x and $|y| \to \infty$ for a localized disturbance, we obtain the first transformation of the stress excitation function, namely

$$\begin{aligned} M_{jn}^{(\tau)}[k, t] = {} & -iR_{jn}\omega_{jn}\left[-\int_{-\infty}^{\infty} dy \int_0^{\infty} H_{jn}^* \operatorname{Div} \tau \, dx \right. \\ & \left. + \int_{-\infty}^{\infty} (H_{jn}^* \tau_x)_{x=0} \, dy\right] + R_{jn} f\left[\int_{-\infty}^{\infty} dy \int_0^{\infty} H_{jn}^* \operatorname{Curl} \tau \, dx \right. \\ & \left. - \int_{-\infty}^{\infty} (H_{jn}^* \tau_y)_{x=0} \, dy\right], \end{aligned} \tag{86}$$

where the following abbreviations are employed for convenience:

$$\operatorname{Div} \tau = \frac{\partial \tau_x}{\partial x} + \frac{\partial \tau_y}{\partial y}, \tag{87}$$

$$\operatorname{Curl} \tau = \frac{\partial \tau_y}{\partial x} - \frac{\partial \tau_x}{\partial y}, \tag{88}$$

and

$$R_{jn} = \frac{kp_{jn}(k)}{\pi\rho(\omega_{jn}^2 - f^2)}. \tag{89}$$

For an axially symmetric atmospheric disturbance, the divergence and curl of the wind stress are readily determined from distributions of the radial and rotary components of the stress respectively.

The first two integrals in (86) represent the effect of "piling up" of water by the action of a converging wind pattern and by the onshore wind component at the coast respectively. The last two integrals represent the quasigeostrophic response of the water level to the circulation or longshore flow caused by a rotary wind pattern and by the longshore wind component at the coast respectively. *In the absence of the earth's rotation, the wind curl and longshore wind component at the coast would have no effect on the water level.* The relative partitioning of excitation among different edge wave modes is governed by $R_{jn}\omega_{jn}$ for the effect of convergent winds or onshore wind component and by R_{jn} for the case of rotary winds or longshore wind component.

A second transformation of (82) is obtained by expressing the stress components in the form

$$\tau_x = -\frac{\partial\Phi}{\partial x} - \frac{\partial\Psi}{\partial y}, \tag{90}$$

$$\tau_y = -\frac{\partial\Phi}{\partial y} + \frac{\partial\Psi}{\partial x}, \tag{91}$$

where the potential functions $\Phi(x, y, t)$ and $\Psi(x, y, t)$ satisfy the relations

$$\nabla^2\Phi = -\operatorname{Div}\tau, \tag{92}$$

$$\nabla^2\Psi = \operatorname{Curl}\tau. \tag{93}$$

In order to define Φ and Ψ uniquely we may specify that Φ and Ψ, together with their gradients, vanish at infinite x and y. The interpretation of the above potential functions is particularly simple for an axially symmetric stress field; in this case Φ and Ψ are determined respectively by the integrals of the radial and rotary components of stress with respect to distance from the axis of symmetry. Substituting (90) and (91) in (82), integrating by parts and making use of the conjugate counterparts of (53) and (54), yields

$$M_{jn}^{(\tau)}[k, t] = \frac{kp_{jn}}{\pi\rho g}\left\{\int_{-\infty}^{\infty} dy \int_{0}^{\infty} (\Phi D_{jn}^{*} - \Psi\zeta_{jn}^{*})\, dx + \frac{\omega_{jn}}{s}\left[-i\int_{-\infty}^{\infty} (\Phi H_{jn}^{*})_{x=0}\, dy + \frac{(2n+1)f - \omega_{jn}}{(2n+1)\omega_{jn} - f}\int_{-\infty}^{\infty} (\Psi H_{jn}^{*})_{x=0}\, dy\right]\right\}. \quad (94)$$

Since D_{jn} and ζ_{jn} vanish identically for $n = 0$, we have as a special case of (94)

$$M_{jo}^{(\tau)}[k, t] = \frac{-kp_{jo}\omega_{jo}}{\pi\rho g s}\int_{-\infty}^{\infty} [(\Psi + i\Phi)H_{jo}^{*}]_{x=0}\, dy. \quad (95)$$

This relation implies a rather surprising result which is of considerable interest from a practical standpoint: *The excitation of the fundamental edge wave mode by wind stress is determined uniquely by variation of the potentials* Φ *and* Ψ *along the shore alone.* For an axially symmetric wind stress vortex, the functions Φ and Ψ can be related to the pressure anomaly, P', by virtue of the gradient wind equation and by a knowledge of the direction of the surface stress relative to the isobars. Consequently, in such a model the distribution of pressure along shore determines the stress-induced fundamental edge waves. This immediately leads to the following corollary: If the atmospheric disturbance is confined to a finite region offshore, such that Φ and Ψ are zero along shore, then the wind stress field associated with the disturbance will not produce a fundamental edge wave. However, the fundamental may be excited to some degree by the direct effect of pressure. Evidently the maximum excitation of fundamental edge waves by wind stress occurs when the center of the atmospheric vortex is close to shore. It may also be noted, on comparing (83) and (95), that the ratio of the excitation by wind stress to that by pressure (for the fundamental waves) is inversely proportional to the bottom slope, as we might have anticipated.

Relation (94) is useful in ascertaining the relative partitioning of excitation between the gravitational edge wave modes ($j = 1, 2$) and the quasigeostrophic mode ($j = 3$) for the higher order edge waves ($n \geqslant 1$). For a *convergent* wind stress system, the products $p_{jn}D_{jn}^{*}$ and $p_{jn}\omega_{jn}$ determine the partitioning of $M_{jn}^{(\tau)}$ among the three separate modes. Inspection of the asymptotic expressions for ω_{jn}, D_{jn} and p_{jn} (Tables II, V and VI) reveals that the gravity modes are favored for large k; however, a nearly equal partitioning of $M_{jn}^{(\tau)}$ between the gravity modes and the quasigeostrophic mode occurs for small k.

For a *rotary* wind stress system, the products $p_{jn}\zeta_{jn}^*$ and

$$\left[\frac{(2n+1)f-\omega_{jn}}{(2n+1)\omega_{jn}-f}\right]p_{jn}$$

determine the relative partitioning of $M_{jn}^{(\tau)}$ among the three modes. Using (30) and Tables II, IV and VI it is found that the quasigeostrophic mode is favored for all k. In a typical hurricane the rotary component of wind stress is usually of greater magnitude than the radial (or convergent) component. We should therefore expect that, if higher order edge waves are generated by a hurricane, the quasigeostrophic mode will play a significant role.

The relative importance of the higher order edge waves, compared with the fundamental, depends to a large extent on the actual distribution of stress in the hurricane. However, a simple special case may serve to demonstrate that the higher order waves are not negligible. In order to examine this question we will return to relation (86). For simplicity we will suppose $f = 0$, as in Greenspan's analysis of pressure-induced edge waves; furthermore, we will consider that the field of stress is divergenceless, as would be the case for an axially symmetric system with purely rotary stresses. In this special case, (86) reduces to

$$M_{jn}^{(\tau)}[k,t] = \mp\frac{i}{2\pi\rho}\sqrt{\frac{k}{(2n+1)gs}}\,e^{-\omega_{jn}t}\int_{-\infty}^{\infty}\tau_x(0,y,t)e^{-iky}\,dy \qquad (96)$$

for $j = 1, 2$ respectively. The absolute value of the excitation decreases rather slowly with increasing n, and it is evident that the higher order waves play a significant role in this special case.

The above example, in fact, raises the question of the convergence of the formal solution given by relations (65) to (67). Examination of the basic relations (1) and (2) at $x = 0$ reveals that the solution may indeed be questionable when τ differs from zero at the water's edge. The difficulty is not merely a mathematical one; undoubtedly it stems from the omission of bottom stress in the formulation of the problem. This matter definitely needs further attention; it may well be that we must impose the condition that the *net* stress at the water's edge should vanish if we are to get sensible results from the linear wave theory. In any event we cannot conclude, *a priori*, that the introduction of bottom stress will completely suppress the higher order edge waves for a given wind stress distribution, for in the more general theory the large divergence of net stress which is required near shore should play a role similar to that of $\tau_x(0, y, t)$ in the special case above.

SUMMARY AND CONCLUSIONS

It has been attempted herein to determine some of the important characteristics of edge waves on a rotating flat earth and to discuss the question of excitation of different edge wave modes from a general point of view. The linearized mathematical development is confined to the case of very small bottom slope and employs the hydrostatic pressure approximation. The vertical component of the earth's vorticity (f) is regarded as a constant. Furthermore, bottom stress is neglected and consequently no allowance is made for the dissipation of energy in the system. In the discussion of forced disturbances it is considered that the forcing functions are localized and consequently our attention is directed exclusively to the question of excitation of edge waves.

The periodic edge wave modes have a surface configuration which is characterized in the offshore direction by Laguerre functions of integer order n, just as in the case of no Coriolis force. However, for a given order $n(\geqslant 1)$ and a given longshore wave length, there are three different frequencies (hence phase speeds) which are possible. Two of these modes are the counterpart of pure gravity edge waves in a nonrotating co-ordinate system; the other mode corresponds to a quasi-geostrophic wave with very small speed. In the case of the fundamental edge waves ($n = 0$), only the first two modes are possible. These inertiogravitational edge waves are the counterpart of Stokes edge wave; however, the phase speed is dependent upon the direction of propagation along the coast. The important characteristics of the various edge wave modes and some general comments in regard to the excitation of these waves are summarized below.

A. *General Comments on Inertiogravitational Edge Wave Modes* ($j = 1, 2$; *all* n)

(1) For a given longshore wave length, the period of free waves progressing to the right is less than that of waves progressing to the left (facing shore from the sea in the northern hemisphere).

(2) For a given longshore wave length, the phase speed of waves progressing to the right is greater than that of waves progressing to the left.

(3) For sufficiently small longshore wave length (less than 10 km at midlatitudes for $s = 10^{-3}$), the effect of the earth's rotation is negligible and the properties of waves progressing in either direction alongshore are essentially the same.

3. *Fundamental Inertiogravitational Edge Waves* ($j = 1, 2; n = 0$)

(1) The magnitude of the group velocity of these waves is independent of the direction of propagation along shore.

(2) The limiting value of the group velocity is gs/f; this is approached for extremely great longshore wave lengths.

(3) The fundamental waves are horizontally divergenceless and irrotational (in the sense that the vertical component of vorticity relative to the earth is zero); this is one of the few characteristics which is independent of the earth's rotation.

(4) For sufficiently large wave length, the waves which propagate to the left are associated with quasigeostrophic flow; this is quite different from the character of the fundamental long waves which move to the right.

4. *Inertiogravitational Edge Waves of Higher Order* ($j = 1, 2; n \geq 1$)

(1) The magnitude of the maximum group velocity for waves moving to the right and left is $(n + 1)gs/f$ and ngs/f respectively.

(2) The higher order inertiogravitational waves possess horizontal divergence; for relatively small longshore wave lengths the divergence is independent of the earth's rotation but is strongly dependent upon bottom slope.

(3) The higher order inertiogravitational waves also possess vorticity relative to the earth; the magnitude of the vorticity is proportional to the vertical component of the earth's vorticity (f) and is also strongly dependent upon bottom slope.

5. *Quasigeostrophic Edge Waves* ($j = 3; n \geq 1$)

(1) These waves are of very small frequency or large period (greater than 12 pendulum hours) and move only to the left along shore (for example, to the south along the east coast of the United States).

(2) The magnitude of the maximum group velocity (and phase speed) is the same as that of fundamental edge waves (gs/f); however, for longshore wave lengths less than about 3000 km (for $s = 10^{-3}$), the phase speed is very small and the group velocity virtually zero.

(3) The small group velocity (for $\lambda > 3000$ km) implies that these waves are not effective in the dispersion of energy.

(4) The oscillatory longshore flow is in quasigeostrophic balance with the oscillatory offshore slope of the sea surface for all longshore wave lengths and for all $n \geq 1$.

(5) The quasigeostrophic edge waves possess large vorticity relative to the earth; the vorticity is independent of bottom slope and *inversely* proportional to f.

E. *Forced or Initial Disturbances*

The general considerations of the dispersion of energy from an ini tially static mound of water disclose that rotation of the earth favors a greater propagation of energy to the left than to the right along shore Some energy will remain temporarily in the region of the initial dis turbance in the form of a quasistationary disturbance with quasi geostrophically balanced flow if the initial disturbance is of sufficiently large horizontal scale (of 2000 km or greater). A formula for the tota energy of a general edge wave disturbance is given in terms of the complex amplitude spectrum of the disturbance.

In respect to forced edge waves due to a localized atmospheric dis turbance, we may note the following general findings:

(1) Greenspan's conclusion that the higher order edge waves are not effectively excited by a Gaussian *pressure* distribution should apply equally well in the presence of the earth's rotation; however, the response of the fundamental waves differs because of the dependency of these waves on the direction of propagation.

(2) Excitation of fundamental edge waves by *wind stress* can be determined from a knowledge of two stress potentials along shore these potentials are determined from the convergence and curl of the wind stress field.

(3) The ratio of excitation of fundamental waves by wind stress to that by pressure is inversely proportional to the bottom slope.

(4) The present analysis indicates that the higher order inertiogravi tational waves can be excited significantly by the onshore componen of stress at the shore or by the convergent part of the wind field, al though this is not conclusive in view of items (6) and (7) below.

(5) The quasigeostrophic mode can be excited by the longshore com ponent of the wind at the shore or by the curl of the wind stress field

(6) The convergence of the series solutions for a stress-induced dis turbance is questionable if a finite net stress is allowed at the shore line

(7) The omission of bottom stress apparently imposes serious limita tions on the applicability of the present theory insofar as stress-induced edge waves are concerned. The need for further investigation i evident.

ACKNOWLEDGMENTS

This work is based in part on investigations conducted for the Texa A. & M. Research Foundation through the sponsorship of the Office o Naval Research (Project NR 083036, N7-onr-48702) and the U. S Weather Bureau (Contract Cwb-9281). The study was initiated dur ing the author's stay at Scripps Institution of Oceanography in the

fall of 1954. The author is indebted to Dr. Carl Eckart, whose stimulating discussions, guidance and lectures have provided the inspiration and encouragement for the present investigation. It must be acknowledged that the method of solution outlined in the appendices is the direct application of the methods discussed by Dr. Eckart. The author is also obliged to Dr. K. Kajiura for many helpful discussions of the problem.

REFERENCES

COURANT, RICHARD AND DAVID HILBERT
1931. Methoden der mathematischen physik. *1.* Julius Springer, Berlin. 469 pp.

CREASE, J.
1956. Long waves on a rotating earth in the presence of a semi-infinite barrier. J. fluid Mech., *1* (1): 86–96.

ECKART, CARL
1934. The analysis of the cosmic-ray absorption curve. Phys. Rev., *45:* 851–859.
1951. Surface waves on water of variable depth. Marine Physical Laboratory and Scripps Institution of Oceanography, Wave Rep. 100, Ref. 51–12, 99 pp.

GREENSPAN, H. P.
1956. The generation of edge waves by moving pressure distributions. J. fluid Mech., *1:* 574–592.

KAJIURA, KINJIRO
1958. Effect of Coriolis force on edge waves (II) Specific examples of free and forced waves. J. mar. Res., *16:* 145–157.

LAMB, HORACE
1932. Hydrodynamics, 6th Ed. Cambridge Univ. Press. 738 pp.

MUNK, WALTER, FRANK SNODGRASS AND GEORGE CARRIER
1956. Edge waves on the continental shelf. Science, *123:* 127–132.

PROUDMAN, J.
1953. Dynamical oceanography. John Wiley and Sons, Inc., New York. 409 pp.

STOKER, J. J.
1957. Water waves. Interscience Publishers, Inc., New York. 567 pp.

STOKES, G. G.
1846. Report of the British Assoc., Part 1, 1846; also Mathematical and physical papers, *1,* Cambridge Univ. Press, 167–168. (1880).

URSELL, F.
1952. Edge waves on a sloping beach. Proc. roy. Soc., (A) *214:* 79–97.

APPENDIX A

In order to establish the orthogonality condition (63) we consider any two sets of eigenfunctions $\{X_{jn}(kx),\ Y_{jn}(kx),\ Z_n(kx)\}$ and $\{X_{pm}(kx),\ Y_{pm}(kx),\ Z_m(kx)\}$ which, together with their associated characteristic frequencies $\omega_{jn}(k)$ and $\omega_{pm}(k)$, respectively, satisfy the basic relations (15) to (17) and conditions (18), (19). The integers $p(1, 2, 3)$ and $m(0, 1, 2, \ldots)$ are considered independent of j and n, but the two sets of functions have a common k. The complex conjugate functions $\{X_{jn}^*,\ Y_{jn}^*,\ Z_n^*\}$ satisfy the conjugate relations formed from (15) to (17), using the general rule that the conjugate of a product equals the product of the conjugates of the individual factors. This implies that the equations which the conjugate eigenfunctions satisfy are the same as (15) to (17) except that i is replaced by $-i$ and ω is taken as ω_{jn}. We will refer to these equations as (15c) to (17c).

The conjugate relations (15c) to (17c) formed from $\{X_{jn}^*,\ Y_{jn}^*,\ Z_n^*,\ \omega_{jn}\}$ are multiplied by X_{pm}/gsx, Y_{pm}/gsx and Z_m, respectively. Similarly, the relations (15) to (17) formed from $\{X_{pm},\ Y_{pm},\ Z_m;\ \omega_{pm}\}$ are multiplied by X_{jn}^*/gsx, Y_{jn}^*/gsx and Z_n^*, respectively. If we add the six resulting equations, we find that the terms involving f and h drop out and the final quadratic relation is

$$i(\omega_{pm} - \omega_{jn}) \left\{ \frac{1}{gsx} [X_{pm}X_{jn}^* + Y_{pm}Y_{jn}^*] + Z_mZ_n^* \right\} + \frac{d}{dx} [X_{jn}^*Z_m + X_{pm}Z_n^*] = 0. \tag{97}$$

The above relation is the normal mode counterpart of an energy equation. If we integrate with respect to x from 0 to ∞ and bear in mind conditions (18) and (19), then it follows that

$$(\omega_{pm} - \omega_{jn}) \int_0^\infty \left\{ \frac{1}{gsx} [X_{pm}X_{jn}^* + Y_{pm}Y_{jn}^*] + Z_mZ_n^* \right\} dx = 0. \tag{98}$$

Thus if $\omega_{pm} \neq \omega_{jn}$, then the integral must vanish and the orthogonality condition (63) follows at once. On the other hand, if $\omega_{pm} = \omega_{jn}$, which requires that the two sets of eigenfunctions are identical, then the integral in (98) does not vanish since the integrand represents the sum of squares of real numbers. The integral in this case is the norm of the eigenfunctions in a collective sense and is given by

$$N_{jn}(k) = \int_0^\infty \left\{ \frac{1}{gsx} [|X_{jn}|^2 + |Y_{jn}|^2] + |Z_n|^2 \right\} dx, \tag{99}$$

which is a positive real number for any j, n and k.

APPENDIX B

An outline of the derivation of relations (68) to (71) is given herein. he form of the solutions for Q_x, Q_y and η are given by (65), (66) and 67), respectively, where the complex amplitude-phase functions $_{jn}(k, t)$ are to be determined. The latter set of functions represents particular set of integral transforms of the functions Q_x, Q_y and η a collective sense; the first step is to find out the form of this trans-rm. The next step is to determine the differential equation in t hich the transforms $A_{jn}(k, t)$ must satisfy.

The first step is carried out as follows: multiply (65), (66) and (67) X_{pm}^*/gsx, Y_{pm}^*/gsx and Z_m^*, respectively; introduce relations (43), 44) and (45); add the resulting three equations; then integrate with spect to x from 0 to ∞. In view of the orthogonality condition 53), the resulting equation reduces to

$$\int_{-\infty}^{\infty} [N_{jn}(k)A_{jn}(k, t)e^{\omega_{jn}(k)t}]e^{iky}\,dk = \int_0^{\infty} \left[\frac{X_{jn}^*Q_x + Y_{jn}^*Q_y}{gsx} + Z_n^*\eta\right] dx, \tag{100}$$

nce the only term in the double summation which does not vanish that for which $p = j$ and $m = n$. We can solve formally for A_{jn} taking the Fourier transform of (100), and if we employ the con-gate counterparts of (43), (44) and (45) we find

$$_{jn}(k, t) = \frac{1}{2\pi N_{jn}(k)} \int_{-\infty}^{\infty} dy \int_0^{\infty} \left[\frac{U_{jn}^*Q_x + V_{jn}^*Q_y}{gsx} + H_{jn}^*\eta\right] dx. \tag{101}$$

his is the particular Fourier-Laguerre transform appropriate to the esent problem.

The next step is to reduce the basic relations (1), (2), (3) and the rmal mode equations (7), (8), (9) to a form involving the above ansform as well as an analogous transform of the forcing functions. ote first that, since the set of functions $\{U_{jn}, V_{jn}, H_{jn}\}$ satisfies rela-ns (7) to (9), the conjugate set $\{U_{jn}^*, V_{jn}^*, H_{jn}^*\}$ must also satisfy ese relations. The procedure is then as follows: multiply the rela-ns (7), (8) and (9) formed from the set $\{U_{jn}^*, V_{jn}^*, H_{jn}^*\}$ by $/gsx$, Q_y/gsx and η, respectively; multiply (1), (2) and (3) by U_{jn}^*/x, V_{jn}^*/gsx and H_{jn}^*, respectively; then add the six resulting equa-ns. Upon collecting terms we find

$$\frac{\partial}{\partial t}\left[\frac{U_{jn}{}^{*}Q_x + V_{jn}{}^{*}Q_y}{gsx} + H_{jn}{}^{*}\eta\right] + \frac{\partial}{\partial x}\left[U_{jn}{}^{*}\eta + H_{jn}{}^{*}Q_x\right] + \frac{\partial}{\partial y}\left[V_{jn}{}^{*}\eta + Q_y H_{jn}{}^{*}\right] = \frac{U_{jn}{}^{*}F_x + V_{jn}{}^{*}F_y}{gsx}. \tag{102}$$

If we integrate with respect to x and y over the entire semi-infinite half plane ($x \geqslant 0$) and make use of (101) and condition (6) we find

$$2\pi N_{jn}(k)\frac{d}{dt}\left[A_{jn}(k, t)\right] = \int_{-\infty}^{\infty}\left(U_{jn}{}^{*}\eta + Q_x H_{jn}{}^{*}\right)_{x=0}\,dy + \int_{-\infty}^{\infty} dy \int_0^{\infty}\left[\frac{U_{jn}{}^{*}F_x + V_{jn}{}^{*}F_y}{gsx}\right] dx. \tag{103}$$

Conditions (5) and (10) imply that the first integral on the right side of (103) vanishes. However, if we relax the condition (5) and allow a finite volume source at shore, then the term $Q_x H_{jn}{}^{*}$ does not vanish at $x = 0$. It therefore follows immediately from (103) that

$$A_{jn}(k, t) = A_{jn}(k, 0) + B_{jn}(k, t) + \int_0^t M_{jn}(k, t)\,dt, \tag{104}$$

where $B_{jn}(k, t)$ and $M_{jn}(k, t)$ are as defined by (70) and (71). The term $B_{jn}(k, t)$ of course vanishes in the absence of a volume source at shore. To complete the solution we note that $A_{jn}(k, 0)$ can be evaluated by direct application of (101) since Q_x, Q_y and η are presumed to be known at $t = 0$. If we make use of (43) to (45) we find that $A_{jn}(k, 0) = a_{jn}(k)$, as defined by (69).

EFFECT OF CORIOLIS FORCE ON EDGE WAVES II) SPECIFIC EXAMPLES OF FREE AND FORCED WAVES[1]

By

KINJIRO KAJIURA

Department of Oceanography and Meteorology, Agricultural and Mechanical College of Texas

ABSTRACT

Modification of edge waves due to Coriolis force is examined in terms of two specific roblems: dispersion of an initial deformation of the water surface; the forced wave ue to a moving atmospheric pressure disturbance. In both cases the scale of the isturbance is an important factor, and the larger the scale the larger the effect of oriolis force. In the northern hemisphere, the initial deformation of the water rface is split into two free edge waves in which the one moving to the left (facing ie coast from the sea) has a larger amplitude than that moving to the right. The ntribution of Coriolis force to the edge wave amplitude for an initial deformation aving a horizontal scale of several hundred kilometers is about 20% at the center the initial stage. In the case of forced waves, movement of the atmospheric pres- re system to the left is more favorable for exciting resurgent edge waves than move- ent to the right. The contribution of Coriolis force is about 10 to 20% in the forced eriod and 20 to 40% in the amplitude for an atmospheric disturbance of several undred kilometers in diameter which moves with a speed of about 20 to 30 knots.

INTRODUCTION

Resurgent water level disturbances caused by hurricanes traveling arallel to a coastline were analyzed from the standpoint of forced dge waves by Munk, *et al.* (1956), who obtained periods of resurgences close accord with some actual observations. However, the range of onditions available was not sufficient to fully establish the veracity of ie theory. Later, Greenspan (1956) extended the theory to a more ealistic situation by treating the transient problem with a Gaussian istribution for the pressure deficit in the atmosphere. One of the nteresting features of Greenspan's analysis is that, for large scale tmospheric pressure disturbances of size comparable to a hurricane, nly the fundamental edge wave mode is excited while all other modes re negligibly small if realistic values for bottom slope and storm propa- ational speed are taken. He concluded that hurricanes are usually

[1] Contribution from Department of Oceanography and Meteorology, A & M Col- ge of Texas, Oceanography and Meteorology Series No. 121.

too big to produce the maximum surge height which is possible for a given pressure deviation.

The theory of edge waves so far has been applied to specific problems without Coriolis force, and this approximation is quite proper if the scale in space and time is reasonably small. However, the effect of the earth's rotation should be taken into account if the period or the horizontal scale of the external force respectively are comparable to or larger than either $1/f$ or the deformation radius C/f (where C is a representative wave velocity or storm speed and f is the Coriolis parameter).

Reid (1958) has discussed the modification of free edge wave modes due to Coriolis force and has presented some general considerations in regard to forced edge waves. In the present paper, two specific problems are investigated in detail on the basis of the fundamental edge wave mode. First, the dispersion of an initial deformation of the water surface is studied. The propagation of free edge waves to the right and to the left (facing the coast from the sea) becomes unsymmetrical due to the presence of Coriolis force, and a greater fraction of the total energy is propagated to the left than to the right in the northern hemisphere. Next, the influence of Coriolis force on forced waves due to a moving atmospheric pressure disturbance is discussed, making use of a model similar to the one utilized by Munk, *et al.* (1956). In this case, movement of the pressure system to the left is more favorable than movement to the right for the development of resurgent waves so long as the velocity of the pressure system is less than the maximum group velocity of the edge waves. The contribution of Coriolis force amounts to about 10 to 20% for the period and 20 to 40% for the amplitude in the resurgent edge waves. The effect of wind stress is not considered in the present paper.

BASIC EQUATIONS

Assume that the coastline is straight and that the depth of water is linearly proportional to the distance offshore, with zero depth at the coast. Take the horizontal right-hand coordinates x and y so that the x-axis is directed offshore with the origin at the coast. Using the equation of continuity and the linearized equations of motion without friction [Reid, 1958: eqs. (1) to (3)], the equation for the surface elevation η (relative to the undisturbed level) due to atmospheric pressure disturbances can be shown to be

$$f^2 \frac{\partial \eta}{\partial t} + \frac{\partial^3 \eta}{\partial t^3} - gsx \nabla^2 \frac{\partial \eta}{\partial t} - gs \left(\frac{\partial^2 \eta}{\partial t \partial x} + f \frac{\partial \eta}{\partial y} \right) = -gs \left(\frac{\partial^2 \bar{\eta}}{\partial t \partial x} + f \frac{\partial \bar{\eta}}{\partial y} \right) - gsx \nabla^2 \frac{\partial \bar{\eta}}{\partial t}, \quad (1$$

here t is time, f the Coriolis parameter, g the acceleration due to ravity, $\bar{\eta}$ the equivalent height of water due to the atmospheric pressure deficit (relative to normal pressure), and s the bottom slope in the direction. The notation ∇^2 is of conventional use with respect to and y.

A useful forced wave equation can be derived from (1), if the atmospheric disturbance moves with constant velocity V, parallel to the coastline, without change of pattern. Putting $\eta = \eta(x, \xi)$ where $= y - Vt$ in (1) and assuming that all disturbances in the water are ero for $t \to -\infty$ in the finite region, we find

$$\frac{\partial^2\eta}{\partial x^2} + \frac{\partial\eta}{\partial x} + \left(x - \frac{V^2}{gs}\right)\frac{\partial^2\eta}{\partial\xi^2} - \left(\frac{f^2}{gs} + \frac{f}{V}\right)\eta = x\left(\frac{\partial^2\bar{\eta}}{\partial x^2} + \frac{\partial^2\bar{\eta}}{\partial\xi^2}\right) + \frac{\partial\bar{\eta}}{\partial x} - \frac{f}{V}\bar{\eta}. \tag{2}$$

his relation is used in the second problem treated in this paper.

DISPERSION OF AN INITIAL DEFORMATION OF THE WATER SURFACE

Consider the situation in which the water body is initially at rest ith a given surface deformation. For mathematical simplicity, we onfine our attention to only the fundamental mode of edge waves by ssuming a suitable deformation initially. Specifically, the initial onditions are as follows:

$$\left.\begin{aligned} \eta &= \frac{\eta_0\, a(a + x)}{(a + x)^2 + y^2} \\ Q_x &= Q_y = 0 \end{aligned}\right\} \quad \text{at } t = 0, \tag{3}$$

here Q_x and Q_y are the components of volume transport of water in he x and y directions respectively. The scale of the initial deformaion is represented by a and corresponds to the distance, on the x or y xis, from the origin to the position where the height of the water surace is half the maximum height (see Fig. 1). The unknowns η, Q_x, nd Q_y for $t > 0$ can be expressed by the superposition of edge waves f the fundamental mode, in view of the form of the Fourier transform f η (with respect to y) at $t = 0$.

The normal mode edge waves may be found from (1), but they are ot discussed here (Reid, 1958). Edge waves of the fundamental ode for any longshore wave length $(2\pi/k)$ are given by

$$H_j = e^{-kx + iky + i\omega_j t}, \tag{4a}$$

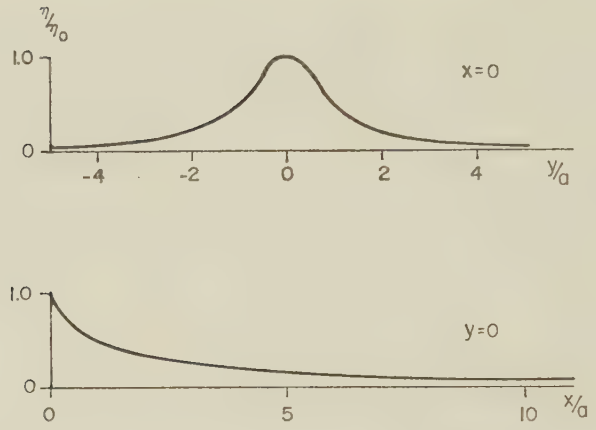

Figure 1. Graphs of the initial distribution of water level; *upper graph* is the relative water level along shore; *lower graph* is the relative water level offshore from the center of the initial disturbance

$$U_j = \frac{-ikgsx}{f + \omega_j} H_j, \tag{4b}$$

$$V_j = \frac{-kgsx}{f + \omega_j} H_j, \tag{4c}$$

where

$$\omega_1 = -\frac{f}{2} - \sqrt{\frac{f^2}{4} + gsk}, \tag{5a}$$

$$\omega_2 = -\frac{f}{2} + \sqrt{\frac{f^2}{4} + gsk}, \tag{5b}$$

$$\omega_3 = f. \tag{5c}$$

Here H_j is the fundamental normal mode elevation (of unit amplitude at shore), U_j and V_j are the corresponding components of volume transport in the x and y directions respectively, and subscript $j = 1, 2,$ or 3 correspond to the different frequencies ω_1, ω_2, and ω_3. Later in this section, $j = 3$ is omitted because there is no contribution from this mode to the surface elevation. Note that $j = 1$ and 2 correspond to waves moving in the positive and negative y directions respectively and that the phase velocity of the former is larger than that of the latter for the same wave length, though the group velocity is the same in both directions.

The functions η, Q_x, and Q_y for $t > 0$ are formally given by the real arts of the following integrals

$$\eta = \Re \int_0^\infty F(k)(p_1H_1 + p_2H_2)\, dk, \tag{6a}$$

$$Q_x = \Re \int_0^\infty F(k)(-ikgsx)\left(\frac{p_1H_1}{f + \omega_1} + \frac{p_2H_2}{f + \omega_2}\right) dk, \tag{6b}$$

nd

$$Q_y = \Re \int_0^\infty F(k)(-kgsx)\left(\frac{p_1H_1}{f + \omega_1} + \frac{p_2H_2}{f + \omega_2}\right) dk, \tag{6c}$$

ere $F(k)$ is the Fourier transform of η at $t = 0$ and $x = 0$, namely

$$F(k) = \eta_0 a e^{-ak}. \tag{7}$$

The weight functions p_1 and p_2 can be determined from the initial onditions such that

$$p_1 = \frac{1}{2}\{1 - (1 + 4gsk/f^2)^{-1/2}\}, \tag{8a}$$

nd

$$p_2 = \frac{1}{2}\{1 + (1 + 4gsk/f^2)^{-1/2}\}. \tag{8b}$$

hese weight functions p_1 and p_2 show that more energy goes to the egative y direction than to the positive y direction and also that the nger the wave length the larger is the difference in wave heights be- veen two waves propagating in opposite directions, as shown in Fig.

The functions p_1 and p_2 are a special case of the p_{jn} functions erived by Reid (1958).

Substituting (7), (8a) and (8b) into (6), we can split the elevation to four progressive waves:

$$\eta = [\eta_1^{(s)} - \eta_1^{(f)}] + [\eta_2^{(s)} + \eta_2^{(f)}], \tag{9}$$

here

$$\eta_{1,2}^{(s)} = \frac{1}{2}a\eta_0 \Re \int_0^\infty \exp\{-k(a + x) + i\theta_{1,2}(y, t; k)\}\, dk, \tag{10}$$

$$_{,2}^{(f)} = \frac{1}{2}a\eta_0 \Re \int_0^\infty (1 + 4gsk/f^2)^{-\frac{1}{2}} \exp\{-k(a + x) + i\theta_{1,2}(y, t; k)\}\, dk, \tag{11}$$

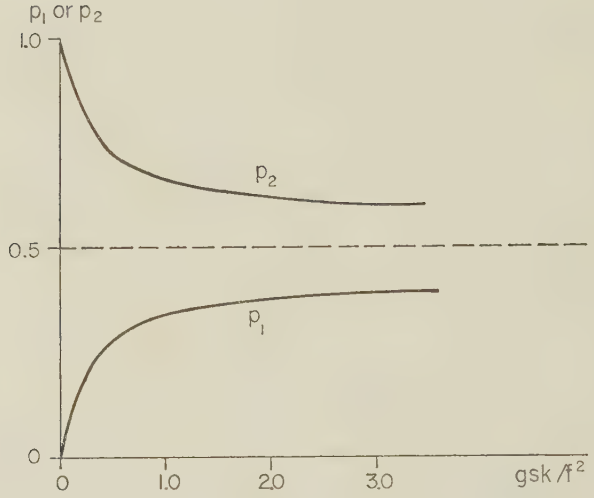

Figure 2. Graphs of the weight functions p_1 and p_2 versus relative wave number gsk/f^2, for the fundamental edge waves.

and

$$\theta_{1,2}(y, t; k) = ky \mp \left[\left(\frac{1}{4}f^2 + gsk\right)^{1/2} \pm \frac{f}{2}\right] t. \tag{12}$$

In (9), $\eta_1^{(s)}$ and $\eta_2^{(s)}$ are the counterparts of the fundamental (Stokes) edge waves without Coriolis force traveling to the positive and negative y directions respectively, although the speeds in the positive and negative directions are different, as is evident in (12). On the other hand, $\eta_1^{(f)}$ and $\eta_2^{(f)}$ represent waves essentially due to Coriolis force.

At the center of the initial deformation $x = y = 0$, it follows from (10) and (11) that initially ($t = 0$):

$$\eta_{1,2}^{(s)} = \frac{1}{2}\eta_0, \tag{13}$$

and

$$\eta_{1,2}^{(f)} = \frac{\sqrt{\pi}}{4}\frac{f\sqrt{a}}{\sqrt{gs}}\eta_0\left(1 - \frac{1}{\sqrt{\pi}}\frac{f\sqrt{a}}{\sqrt{gs}}\right), \tag{14}$$

provided that $a \ll 4gs/f^2$. The latter condition implies that the scale a must be much less than 4000 km at midlatitudes for $s = 10^{-3}$. The ratio of the elevations $\eta_{1,2}^{(f)}/\eta_{1,2}^{(s)}$ is expressed approximately by $\frac{fa}{C_0}$, where $C_0 = \sqrt{\frac{gs\lambda}{2\pi}}$ is the ordinary edge wave velocity with the

wave length $\lambda = 8a$. The ratio computed for several values of a are shown in Table I, from which we can clearly visualize the effect of Coriolis force. In the case of the initial deformation with an effective radius of about 400 km ($a = 100$ km), the contribution of Coriolis force is greater than 20% of the ordinary edge wave. If we compare the waves traveling in the positive y and in the negative y directions, the difference of initial heights of the two progressive waves may become 40% of the average height of two waves. However, the resultant deformation of the water surface does not appreciably deviate from the deformation for the case without Coriolis force so long as time is not great, because $\eta_1^{(f)}$ and $\eta_2^{(f)}$ cancel each other for initial stages.

TABLE I. THE RATIO $\eta_{1,2}^{(f)}/\eta_{1,2}^{(s)}$ AT $x, y, t = 0$ FOR $f = 10^{-4}$/SEC, AND $s = 10^{-3}$.

a(km)	10	50	100
Ratio	0.084	0.17	0.23

Making use of the method of stationary phase, we can integrate (10) and (11) approximately for large values of t, such that

$$\eta_1^{(s)} - \eta_1^{(f)} = \frac{1}{2} a\eta_0 \left(1 - \frac{fy}{gst}\right) \exp\left[-\frac{1}{4}\frac{f^2(a+x)}{gs}\left\{\left(\frac{gst}{fy}\right)^2 - 1\right\}\right] \times \sqrt{\frac{gs\pi}{}}\, \frac{t}{y^{3/2}} \cos\left[\frac{1}{4}\frac{f^2 y}{gs}\left(\frac{gst}{fy} + 1\right)^2 - \frac{\pi}{4}\right], \text{ for } y > 0, \quad (15a)$$

and

$$\eta_2^{(s)} + \eta_2^{(f)} = \frac{1}{2} a\eta_0 \left(1 + \frac{f|y|}{gst}\right) \exp\left[-\frac{1}{4}\frac{f^2(a+x)}{gs}\left\{\left(\frac{gst}{fy}\right)^2 - 1\right\}\right] \times \sqrt{\frac{gs\pi}{}}\, \frac{t}{|y|^{3/2}} \cos\left[\frac{1}{4}\frac{f^2|y|}{gs}\left(\frac{gst}{f|y|} - 1\right)^2 - \frac{\pi}{4}\right], \text{ for } y < 0. \quad (15b)$$

The above solutions are valid for $f|y|/gst < 1$ and $4\sqrt{|y|/gst^2} \ll 1$. For $f|y|/gst > 1$, there exists no stationary phase in the integral given by (11). Practically speaking, the second condition requires that the time must be very long (beyond a practical limit) if $f|y|/gst$ is not very small, because $ft > 10^3 f|y|/gst$. Therefore, if the stationary phase is attained at all, the value of $f|y|/gst$ is already very small, and the wave amplitude is almost negligible near the origin. However, formally looking into the argument of the cosine term in (15a) and (15b) we can find that modification of the dispersive character of edge waves due to Coriolis force is such that

local period: $$T_{1,2} = T_0 \cdot \frac{1}{1 \pm \alpha}, \tag{16a}$$

wave length: $$\lambda_{1,2} = \lambda_0 \cdot \frac{1}{1 - \alpha^2}, \tag{16b}$$

phase velocity: $$C_{1,2} = C_0 \left(\frac{1 \pm \alpha}{1 \mp \alpha}\right)^{1/2}, \tag{16c}$$

group velocity: $$G_{1,2} = \frac{|y|}{t}, \tag{16d}$$

where

$$\alpha = f|y|/gst, \tag{16e}$$

$$T_0 = \frac{4\pi|y|}{gst}, \tag{16f}$$

$$\lambda_0 = \frac{8\pi y^2}{gst^2}, \tag{16g}$$

and

$$C_0 = \sqrt{\frac{gs\lambda_0}{2\pi}}, \tag{16h}$$

where the subscript $_0$ indicates the quantity without Coriolis force and the upper sign and the lower sign in (16a, b, c) correspond to the subscripts $_1$ and $_2$ respectively. The above relationships are all consistent with the discussion based on the normal modes (Reid, 1958) such that $C_1 > C_2$ and $G_1 = G_2$ for the same wave length. The ratio of the wave amplitudes at a common distance $|y|$ to the right and to the left is given by

$$r = \left|\frac{\eta_1^{(s)} - \eta_1^{(f)}}{\eta_2^{(s)} + \eta_2^{(f)}}\right| = \frac{1 - \alpha}{1 + \alpha}, \tag{17}$$

as shown in Fig. 3. The amplitudes for both waves decrease very rapidly with decreasing α due to the exponential factor involved in (15a) and (15b).

As a whole, the effect of Coriolis force increases with increasing values of α, ($\alpha < 1$). This implies that, for a fixed time, the local wave length increases with distance from the origin, and consequently the effect of Coriolis force increases. However, for $|y| > gst/f$ the condition of stationary phase does not exist and consequently the local wave length is undefined. It is probable that beyond this point, to the left, the water level decays monotonically to zero as in the outer

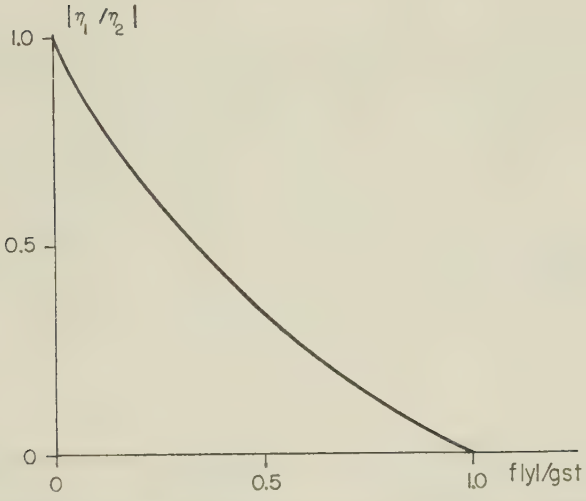

Figure 3. Ratio of the wave amplitudes at a common distance $|y|$ to the right and to the left at time due to an initial static mound of water.

part of the initial disturbance, but to the right the elevation is essentially zero beyond $|y| = gst/f$.

Note that the condition $f|y|/gst < 1$, which is required to establish the stationary phase, gives the maximum group velocity $G_{1,2} = gs/f$; this maximum value corresponds exactly to the maximum group velocity derived from the study of the normal modes [Reid, 1958: eq. (42)].

FORCED WAVE DUE TO A TRAVELING PRESSURE DISTURBANCE

For atmospheric pressure disturbances, (2) can be solved generally by means of the Fourier transform technique. However, for mathematical simplicity, we assume an atmospheric disturbance of the form

$$\bar{\eta}(x, \xi) = \frac{\bar{\eta}_0 a(x + a)}{\xi^2 + (x + a)^2}, \quad \xi = x - Vt. \tag{18}$$

This is the same form as that assumed by Munk, *et al.* (1956), which is convenient since it implies that we can confine our attention to fundamental waves only. The wave characteristics derived from this model may be considered as fairly representative of the actual situation because, according to Greenspan (1956), the fundamental mode of the edge wave is the only mode effectively excited by a pressure disturbance of the scale comparable to a hurricane.

Since η and $\partial\eta/\partial t$ are assumed zero for $t \to -\infty$ (which corresponds to $\xi \to \infty$ for $V > 0$, and $\xi \to -\infty$ for $V < 0$), the Fourier transform of (2) with the pressure disturbance (18) may be solved straightforward, and the solution for η is formally given by

$$\eta(x, \xi) = -\frac{1}{2}\bar{\eta}_0 a k_s \int_{-\infty+i\tau}^{\infty+i\tau} \frac{e^{-k^*(a+x)-ik\xi}}{k^* - K}\, dk, \tag{19}$$

where $\tau < 0$ for $V > 0$ and $\tau > 0$ for $V < 0$ and $k^* = \sqrt{k^2 + \epsilon^2}$ $(\epsilon \to 0)$. The other parameters are

$$K = k_s(1 + V/G) \tag{20a}$$

$$k_s = gs/V^2 \tag{20b}$$

$$G = gs/f. \tag{20c}$$

The quantities k_s and G represent respectively the wave number for the resurgence without Coriolis force and the maximum group velocity. If we assume $f = 0$ $(G \to \infty)$, the solution for η reduces to the case discussed by Munk, *et. al.* (1956) and by Greenspan (1956).

Making use of the contour integral technique, we can express (19) for $V > 0$ in the form[2]

$$\eta = \Phi(x, |\xi|, K), \ \xi > 0, \tag{21a}$$

$$\eta = \Phi(x, |\xi|, K) + 2\pi\bar{\eta}_0 a k_s e^{-K(a+x)} \sin K|\xi|, \ \xi < 0, \tag{21b}$$

where

$$\Phi(x, |\xi|, K) = \bar{\eta} a k_s \int^{\infty} \frac{\{K \sin m(a + x) - m \cos m(a + x)\}e^{-m|\xi|}}{m^2 + K^2}\, dm. \tag{22}$$

For $V < 0$, we have a similar expression, provided $|V| < G$:

$$\eta = \Phi(x, |\xi|, K) + 2\pi\bar{\eta}_0 a k_s e^{-K(a+x)} \sin K|\xi|, \ \xi > 0, \tag{23a}$$

$$= \Phi(x, |\xi|, K), \qquad \xi < 0. \tag{23b}$$

If $|V| > G$, the oscillatory part of the above solution is absent.

Asymptotically, for large values of $\xi^2 + (x + a)^2$, Φ is proportional to the atmospheric pressure disturbance $\bar{\eta}$. In fact, for $|V| \to 0$, $\Phi(x, |\xi|, K) \to \bar{\eta}$ for all values of x and $|\xi|$. Thus, the forced response in the water consists of a train of resurgent edge waves of speed V behind the storm together with a disturbance restricted to the immediate neighborhood of the pressure system for which the water level is

[2] A somewhat similar integration is given by Lamb (1932: 412).

the direct effect of the atmospheric pressure. This result is qualitatively similar to that for the case without Coriolis force. However, if $-V/G > 1$, no resurgent wave exists in the present case. In other words, if the storm moves faster in the negative y direction than the maximum group velocity gs/f (this is very unrealistic), the resurgent waves do not develop. The case $V = -G$ is the resonant condition and the water level increases indefinitely ($\Phi(x, |\xi|, K) \to \infty$). For the movement of the storm in positive y direction, no such condition exists.

The resurgent edge waves behind the storm are given by

$$\eta(x, |x - Vt|) \simeq 2\pi\bar{\eta}_0 a k_s e^{-K(a+x)} \sin K|x - Vt|. \tag{24}$$

Therefore, the period of edge waves is given by

$$T = \frac{2\pi}{K|V|} = T^*(1 + V/G)^{-1}, \tag{25a}$$

or

$$(T^* - T)/T^* \simeq V/G = fV/gs, \tag{25b}$$

where $T^*(= 2\pi|V|/gs)$ is the period of forced edge waves in the absence of Coriolis force. The contribution of Coriolis force in the forced period is approximately $|V|$ per cent of T^* if V is measured in meters per second, $s = 10^{-3}$ and $f = 10^{-4}$ sec^{-1}. Resurgences following a pressure pattern which moves to the right have a shorter period than that of forced edge waves without Coriolis force. The opposite is true of resurgences associated with a pressure pattern which moves to the left. If the scale of the pressure system is very large, the contribution of Coriolis force to the height of resurgent waves becomes large compared with that which occurs in the case without Coriolis force. Putting η_1 and η_2 as the amplitude of resurgent edge waves moving to the right and to the left ($V > 0$ and $V < 0$) respectively, and putting η^* as the amplitude of edge waves in the case without Coriolis force, we have

$$\frac{\eta_1}{\eta^*} = \frac{\eta^*}{\eta_2} = e^{-f(a+x)/|V|}. \tag{26}$$

Note that the ratio is independent of the slope of the bottom, and the effect of Coriolis force is measured by the number $fa/|V|$, which is what we anticipated in the beginning. For reasonable values of V and a ($V \sim 10$ to 15 m/sec, $a \sim 25$ to 50 Km), the contribution of Coriolis force in the wave amplitude along the coast seems to be about 20 to 40%.

The ratio of amplitudes η_1, η_2 and η^* to the equilibrium height $\bar{\eta}_0$ along the coast is shown in Table II. There exists an optimum value of a for which the ratio becomes maximum if V and s are fixed.

The amplitude of edge waves decreases exponentially in the offshore direction, and the rate of decrease is larger for a storm moving in the positive y direction than that for a storm moving in the negative y direction.

TABLE II. Ratios of the various amplitudes of resurgent edge waves relative to the maximum equilibrium height along the coast for $f = 10^{-4}$ sec^{-1} and $s = 10^{-3}$. The ratio $\eta^*/\bar{\eta}_0$ is shown in italics. Upper figures in each block represent $\eta_1/\bar{\eta}_0$ (storm moving to the right); the lower figures represent $\eta_2/\bar{\eta}_0$ (storm moving to the left).

V (m/sec) \ a(Km)	10	25	50	100
5	0.38	0.001	—	—
	0.46	*0.002*	—	—
	0.56	0.004	—	—
10	2.09	1.00	0.13	—
	2.30	*1.29*	*0.21*	*0.02*
	2.55	1.65	0.35	0.06
15	1.67	1.94	1.09	0.17
	1.79	*2.30*	*1.51*	*0.33*
	1.91	2.71	2.11	0.64
20	1.16	1.85	1.75	0.78
	1.23	*2.09*	*2.26*	*1.28*
	1.29	2.38	2.89	2.12

CONCLUDING REMARKS

In general, Coriolis force in the edge wave problem has the effect of producing unsymmetrical disturbances moving to the right and to the left along the coast, with waves moving to the left (negative y direction) from an initial static mound containing the larger fraction of total energy. For pressure-induced disturbances, a storm moving to the left is more favorable in the excitation of resurgent edge waves behind the storm than movement to the right. This is true so long as the speed of the storm does not surpass the maximum group velocity of the edge wave (order of 100 m/sec). The model utilized in this paper is not adequate for predicting changes in water level due to actual meteorological disturbance, because (besides the rather arbitrary pressure pattern in the present example) the effect of wind stresses is completely neglected. A brief investigation concerning the effect of wind stress (to appear later) shows that the stress may produce edge waves of the higher modes and that the cumulative effect of wind stresses parallel to the coast would remain behind the storm; this manifests itself as a geostrophic current system parallel to the coast (if the storm travels a long distance without change of pattern).

ACKNOWLEDGMENTS

This work is based in part on research conducted for the Texas A. & M. Research Foundation through sponsorship of the U. S. Weather Bureau (Contract Cwb-9281).

REFERENCES

Greenspan, H. P.
1956. The generation of edge waves by moving pressure distributions. J. fluid Mech., *1:* 574–592.

Lamb, Horace
1932. Hydrodynamics, 6th Ed., Cambridge Univ. Press. 738 pp.

Munk, Walter, Frank Snodgrass and George Carrier
1956. Edge waves on the continental shelf. Science, *123:* 127–132.

Reid, R. O.
1958. Effect of Coriolis force on edge waves (I) Investigation of the normal modes. J. mar. Res., *16:* 109–144.

THE USE OF A LARGE CAPACITY PORTABLE PUMP FOR PLANKTON SAMPLING, WITH NOTES ON PLANKTON PATCHINESS[1]

By

WILLIAM ARON

Department of Oceanography, University of Washington
Seattle 5, Washington

ABSTRACT

A centrifugal pump with rated capacity of 400 gals./min. was used for plankton sampling in Puget Sound. With the ship under way, 50 simultaneous paired hauls were made with the pump and with a 0.5-meter nylon plankton net. The pumped water was passed through a special filtering unit with negligible damage to the plankters. Data show remarkable agreement between catches of fish eggs captured by pump and by tow net. Large discrepancies between catches of motile organisms by pump and by tow net are discussed; gear selectivity and plankton patchiness are considered as possible explanations for variations which occur between the two sampling devices. Use of large capacity pumps is recommended for further investigations of horizontal and vertical distribution of plankton.

INTRODUCTION

The Department of Oceanography of the University of Washington has realized the need for a device capable of obtaining surface plankton samples from either a moving or a stationary vessel. Consequently, during a recent fisheries research program, this study was undertaken to evaluate the pump as a means of sampling plankton in surface waters.

A 0.5-meter plankton net is compared to a centrifugal pump with a rated capacity of 400 gals./min. Fifty paired hauls in Elliott Bay, Puget Sound, Washington (Fig. 1) from 21 to 26 January 1957 were made in conjunction with a fish egg distribution study conducted by Dr. A. C. DeLacy, University of Washington College of Fisheries, and a group of his students. All of the hauls were obtained from the M. V. Commando, research vessel of the College of Fisheries, while the ship was under way. Samples collected from an anchored vessel will be the subject of a later report.

[1] Contribution No. 220 from the Department of Oceanography, University of Washington. This work was supported in part by funds provided by the Office of Naval Research, Contract NR 083-012.

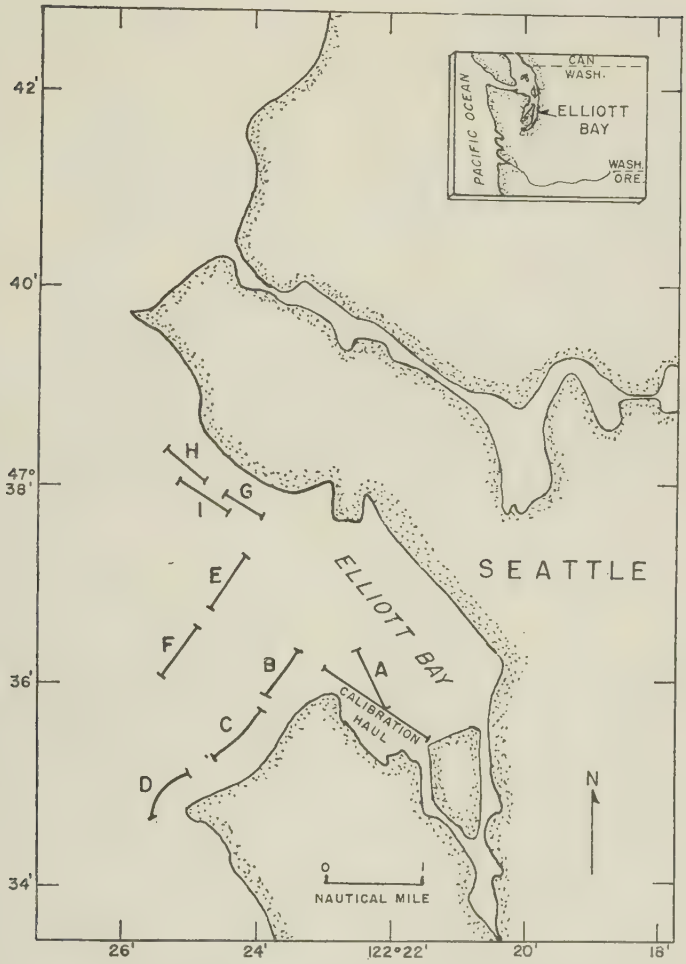

Figure 1. Location of stations in Elliott Bay, Puget Sound, Washington.

HISTORY

The use of pumps as plankton sampling devices is not new to oceanographers and limnologists. Hensen's use of a steam pump in 1887 (Kofoid, 1897) marked the beginning of extensive but scattered attempts to provide a suitable method for pumping plankton. Although early researches were characterized by the use of makeshift equipment operated on a small scale, even these studies were marked with some success, particularly in the study of phytoplankton. Later

TABLE I. Historical summary of plankton pump research

Investigator and year	*Type of pump*	*Capacity*	*How used*	*Where used*
Hensen, 1887	Steam pump	Not given	Not given	Marine
Cleve, 1896	Ship's pump	Not given	Attached silk net to pump when deck was washed	Marine
Giesbrecht, 1896 (describes Kramer's work)	Ship's pump	Not given	Not given	Marine: delivered water to bathtub of steamer
Peck, 1896	Steam pump	2-inch hose	Not given	Marine: Buzzard's Bay, Massachusetts
Kofoid, 1897	Double-acting force pump; hand operated	1 m^3/600 strokes; 2-inch suction hose	20 feet of hose; 1-inch hose for outlet resulted in squeezing animals through No. 20 net; 1½-inch hose used as result	Lakes
Fordyce, 1898	Force pump; hand operated	347.5 $in.^3$/stroke	Net of fine wire gauze	Lakes
Bachmann, 1900	Intermittent pump?	10 l in 15 min. at 70 m depth	No. 20 silk net, 54–70μ mesh opening	Lakes
Juday, 1916	Vane pump; gas powered	300 rpm; 30 l/min.	30 m of 2.5-cm hose	Lake Mendota
Robert, 1922	a. Wing pump	0.1 l/stroke; 1.5-cm hose	20 l samples to depth of 50 m	Lakes
	b. Hany plankton pump	Size not indicated; probably worked by compressed air.	15 l samples	Lakes
Kokubo and Tamura, 1931	Hand pump?	30 l in 2½ min.	23 mm tubing, 30 m long	Aomori Bay, Japan

TABLE I. (CONT.)

Investigator and year	*Type of pump*	*Capacity*	*How used*	*Where used*
Kokubo, 1933	Wing pump	40 l/6 min.	15 mm tubing to depth of 200 m	Not given
Gibbons and Fraser, 1937	Centrifugal pump	2.5 m^3/10 min.	25 feet of 2-inch hose	Marine
Tester and Stevenson, 1949	Portable gasoline-motor pump	Not given	2-inch iron pipe at depth of 3 feet	Marine: British Columbia
Barnes, 1949	Ex-National Fire Service	350 l/min.	170 l/min.; net 200 mesh/inch	Marine
Tonolli, 1951	Suction pump	Not given	Sucking out contents of tow nets	Lakes
Langford, 1953	a. Power pump; vane type b. Semirotary hand pump	30 l/min. through 1-inch hose 5 l/min. through ½-inch garden hose	All samples collected through No. 20 bolting cloth; all samples 10 l each. Compared two pumps against Juday trap	Lakes
Collier, 1957	⅓ H.P. motor and pump	450 gals/hr	8 hr. continuous sample 10 feet below sea surface; ¼ of pump discharge sampled	Marine: Gulf of Mexico

advances in the development of portable gasoline-operated centrifugal pumps allowed large volumes of water to be filtered and made such gear more satisfactory for sampling zooplankton than previous devices. Table I provides an historical summary of plankton-pump research. The paper by Gibbons and Fraser (1937) is especially useful since it covers the early studies and also provides references to related work not covered in this paper.

METHODS AND RESULTS

Of the pumps listed in Table I, that used by Gibbons and Fraser (1937) delivered 270 l/min. Tester and Stevenson (1949) used a 2-inch pump which probably provided greater capacity than that used by Gibbons and Fraser, but the report does not cite its capacity. Other pumps yielded far less than the 200 l/min. set by Wiborg (1948) as a minimum for reliable sampling.

The gasoline-powered centrifugal pump used in the present study delivered 1533 l/min. through a 3-inch outlet. To prevent excessive damage to plankters it was necessary to reduce the velocity of the water by passing it through a special filtering drum (Fig. 2) designed by Dr. Robert Paquette with some help by the author. Water is passed from the pump into the bottom of a 54-gallon drum, in the center of which is a pipe 40 cm in diameter and about two-thirds the height of the drum. The water which enters the drum passes out through this pipe at about 1/25th of the original velocity, and a filtering net installed at the end of the pipe filters the water efficiently at the reduced flow. For the present work a 0.5-meter silk plankton net, with a mesh opening of 0.544 mm, was used for filtering. At the beginning of the study the net was fastened to the pipe by means of large rubber bands, but later, for convenience in handling, it was held tightly between the pipe and a metal hoop made with an inside diameter slightly larger than the outside diameter of the pipe. Fig. 3 is a schematic diagram of the filtering system.

The pump was calibrated by determining the length of time required to fill a 54-gallon drum: 8 seconds with 6.1 meters of 3-inch suction hose.

With the exception of jellyfish and ctenophores, which were badly damaged, the pump catches were in excellent condition; in fact, the one attempt to hatch fish eggs caught with the pump was successful.

The tow collections were taken with a 0.5-meter net equipped with an Atlas meter. This net, made of monofilament nylon with a mesh opening of 0.476 mm, was calibrated by towing it over a known distance and recording the revolutions made by the Atlas meter; thus, the number of liters strained per revolution of the meter was deter-

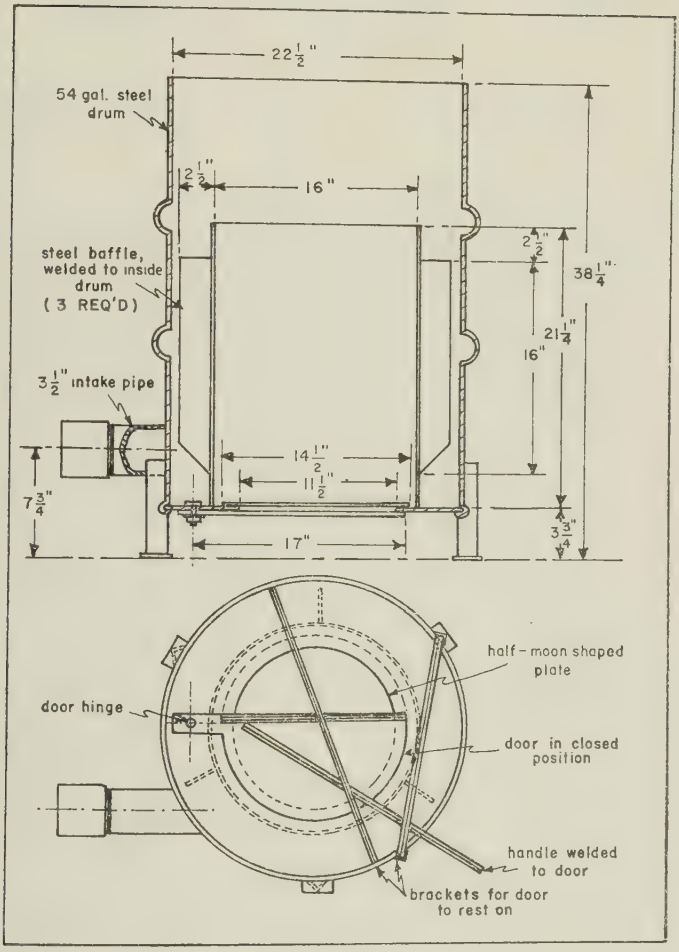

Figure 2. Filtering drum used during experiment.

mined. It is assumed that the tow net fished at 100% efficiency, straining all of the water column through which it passed. The volume of water strained by all tow-net hauls was then based on the number of meter revolutions for the haul. Because of the large mesh size and because of the relatively low plankton abundance, no clogging occurred.

The paired hauls were made as follows: the suction hose was suspended on the port side, close to the ship, while the plankton net was

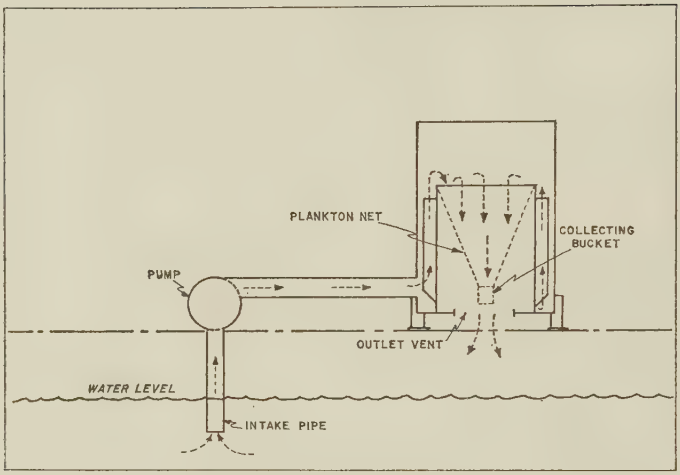

Figure 3. Schematic diagram of filtering equipment.

TABLE II. Comparison of paired net and pump plankton catches, adjusted to number of organisms/100 m^3; figures based on total counts

Date	*Haul; station*	*Time*	*Fish eggs*		*Motile organisms*		*Copepods*		*Motile organisms minus copepods*	
			Net	*Pump*	*Net*	*Pump*	*Net*	*Pump*	*Net*	*Pump*
1-21	1–A	1322	1749	1083	147	436	130	422	17	14
	2–B	1350	139	77	107	102	78	102	29	0
	3–D	1437	40	27	229	7411	177	7373	52	38
	4–F	1503	46	45	220	4311	184	4266	36	45
	5–E	1520	52	13	190	8870	178	7840	12	1030
1-22	6–C	0943	271	96	170	755	137	723	33	32
	7–D	1000	53	77	454	545	429	500	26	45
	8–F	1020	62	91	149	327	109	307	40	20
	9–E	1041	1431	564	578	282	410	199	168	83
	10–C	1149	112	218	392	243	362	122	30	121
	11–A	1258	471	436	254	153	235	141	19	12
	12–B	1318	122	134	150	70	123	58	27	12
	13–C	1335	173	121	232	218	208	141	34	123

TABLE II. (CONT.)

Date	*Haul; station*	*Time*	*Fish eggs*		*Motile organisms*		*Copepods*		*Motile organisms minus copepods*	
			Net	*Pump*	*Net*	*Pump*	*Net*	*Pump*	*Net*	*Pump*
1–22	14–D	1352	37	45	719	429	662	410	57	19
	15–F	1411	54	77	267	122	232	64	35	58
	16–E	1429	110	173	225	211	191	153	34	58
	17–H	1453	2769	4842	294	320	221	224	73	96
	18–G	1511	2979	4265	268	237	212	211	56	26
	19–I	1535	1619	3642	899	1543	846	1531	53	12
1–23	20–A	0915	874	1051	144	461	111	352	33	109
	21–B	0935	381	372	252	250	212	167	40	83
	22–C	0953	377	359	150	404	108	340	42	64
	23–D	1010	208	141	149	160	110	135	39	25
	24–A	1303	1529	1827	156	122	138	58	18	64
	25–B	1321	476	526	137	173	111	128	26	55
	26–C	1337	205	160	150	77	113	70	33	7
	27–F	1403	266	295	138	365	112	340	26	25
	28–E	1420	386	115	130	6	112	6	18	0
1–24	29–A	1644	19	26	113	51	92	51	21	0
	30–B	1706	348	122	196	775	103	743	93	32
	31–C	1722	83	38	165	224	117	173	48	51
	32–D	1739	43	26	387	839	346	800	41	39
	33–F	1756	39	6	335	19	285	19	50	0
	34–C	1814	103	71	447	1255	407	1229	40	26
	35–A	2003	170	64	285	672	261	647	24	25
	36–B	2020	910	475	362	1024	300	992	62	32
	37–C	2036	118	173	391	903	351	890	40	13
	38–D	2052	88	64	613	211	613	211	0	0
1–25	39–A	1700	2600	2135	87	1299	70	1184	17	15
	40–B	1719	524	519	193	813	137	704	56	109
	41–C	1737	320	430	202	596	164	525	38	71
	42–D	1752	80	83	326	973	284	800	42	173
	43–F	1812	34	13	413	1037	333	992	80	45
	44–E	1828	256	231	502	1037	414	986	88	51
	45–Cal	1858	149	29	120	409	105	384	15	25
1–26	46–Cal	1923	84	195	180	1114	144	921	36	193
	47*–B	0701	1692	1417	178	384	152	366	26	18
	48–C	0715	53	51	163	243	139	211	24	32
	49–D	0733	49	77	206	211	174	173	32	38
	50–E	1818	3475	4200	72	231	65	211	7	20

* Pumped only 7 minutes.

towed from an outrigger on the port side, outboard and slightly behind the ship. Both samplers were fished close to the surface, their mouth openings about seven meters apart. At first the mouth of the hose was directed towards the stern, but during most of the study it was directed forward, in the direction of the ship's motion; no difference in catches could be detected between the two positions.

The pump was kept running between hauls as well as during hauls, but the filtering net for the pump system was engaged only while the towing net was in the water. The hauls were made for 10 minutes. At the end of each haul the sides of the nets were rinsed and the contents were collected in identical metal cups at the cod ends. Collections were preserved in 5% formalin and stored in 8-ounce jars.

In the operations outlined above, the 0.5-meter net filtered approximately 200 m^3 whereas the pump delivered about 15 m^3. Table II presents comparative data on the collections taken in each haul and adjusted to obtain the number per 100 m^3. The entire samples of fish eggs, total organisms, and total copepods taken in each haul were counted.

Most of the fish eggs are those of the pleuronectid, *Parophrys vetulus*, probably mixed with some eggs of another pleuronectid, *Platichthys stellatus*, and some eggs of the gadid, *Gadus macrocephalus*. All of these eggs are about 1.0 mm in diameter and are practically indistinguishable. Of the total organisms caught, other than fish eggs, copepods were the most important group; they constituted 84.7% of the tow net catches and 92.0% of the pump catches. Amphipods, crustacean larvae, annelids, chaetognaths, medusae, tunicates, fish larvae, euphausiids, ostracods, and cladocerans also were caught.

Table III gives the number per 100 m^3 as well as maximum and minimum measurements of the six dominant copepod species taken in eight paired hauls: *Calanus finmarchicus*, *Tortanus discaudatus*, *Aetidius armatus*, *Acartia longiremis*, *Metridia lucens*, *Corycaeus affinis*. In the case of 10 of these hauls, the whole catch was counted; for the other six hauls, aliquot samples were counted according to the method described by Frolander (1955).

TABLE III. Counts and size range of selected copepod species/100 m³ of water taken in paired hauls

Haul		*Calanus finmarchicus* 2.6–4.2mm	*Tortanus discaudatus* 1.3–1.7mm	*Aetidius armatus* 1.5–2.3mm	*Acartia longiremis* 0.9–1.5mm	*Metridia lucens* 1.9–2.8mm	*Corycaeus affinis* 0.75–1.1mm
5	Net	0.5	75	0	96	0	4
	*Pump	64	512	0	1024	0	5632
14	*Net	134	158	462	0	0	12
	Pump	13	13	301	51	0	6
19	*Net	150	0	582	75	0	19
	Pump	38	0	1286	0	13	19
22	Net	24	41	15	19	0	0
	Pump	26	122	13	115	0	0
39	*Net	5	14	28	0	32	0
	Pump	96	307	141	141	96	64
43	*Net	72	124	165	0	41	0
	Pump	45	179	224	26	51	0
44	*Net	145	114	103	41	41	0
	Pump	77	102	141	58	32	0
48	Net	18	43	45	12	1	0
	Pump	51	6	45	38	0	0

* Counts based on aliquot sample.

DISCUSSION

Table II shows that the concentration of eggs obtained by both tow net and pump net are similar for most pairs of hauls (see Fig. 4). In only 12 pairs of hauls did the catches of eggs vary by more than a factor of 2. If all hauls are considered, the tow net gave a higher concentration in 29 pairs, the pump in 21 pairs.

Nearly all of the fish eggs were from demersal species. Spawning by these fish apparently takes place close to the bottom and the eggs float to the surface. It is reasonable to assume that their distribution is random over a small area (let us say a square having sides 7 meters in length) unless an oceanographic boundary condition such as a convergence line exists within the square, and it is reasonable to assume further that two sampling devices operating within the area at the same time would catch, on an average, the same number of fish eggs per unit volume of water.

Although the mesh sizes of the nets are slightly different (tow net 0.476; pump net 0.544 mm), the mesh openings in both are sufficiently small to prevent the escape of such eggs as are used in this study. The

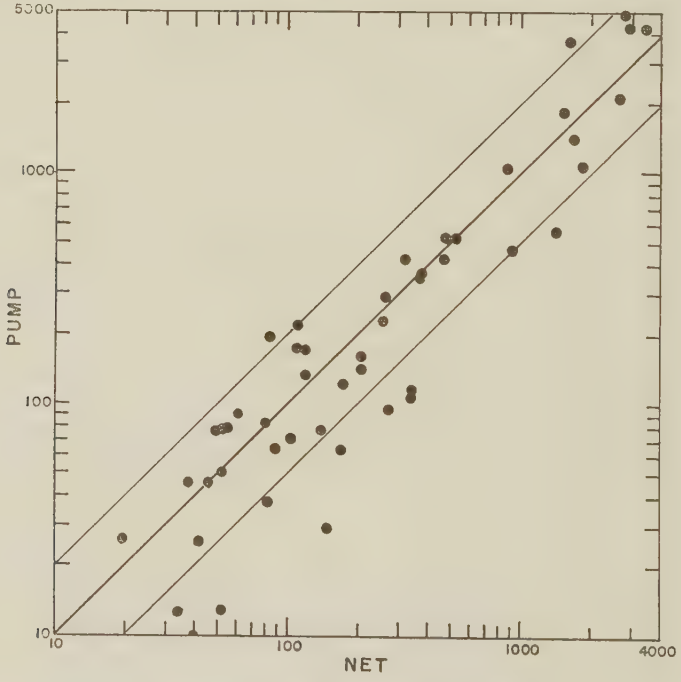

Figure 4. Catch of eggs/100 m³ of water.

close approximation of the fish egg counts for the paired hauls is therefore a good indication of the validity of the assumption that the tow net fishes close to 100% efficiency in the case of these eggs.

Table II shows that for both motile organisms and copepods there are pronounced discrepancies between catches of the two nets; since the total number of motile organisms is strongly influenced by the catch of copepods, the total catch of motile organisms minus copepods is also listed. In the case of total motile organisms as well as copepods the pump outfished the tow net in 23 of the 50 paired hauls; note that the pump exceeded the tow net at the same stations for both categories excepting Sts. 2-B and 49-D; at St. 2-B the net outfished the pump for total motile organisms while the pump exceeded the tow net in the case of copepods; at St. 49-D it was vice versa. In both of these exceptions, however, the discrepancies were very slight. Regarding motile organisms minus copepods, the tow net outfished the pump in only 26 of the 50 paired hauls; in 21 pairs of hauls the catch of motile organisms minus copepods varied by more than a factor of 2 between the two types of gear. The tow-net and pump catches of copepods and of total motile organisms minus copepods are plotted in Figs. 5 and 6.

There are two possible explanations for the wide variations found in the counts of the motile organisms: gear selectivity and/or plankton patchiness.

The data in Table III give counts of the major copepod species in eight pairs of hauls as well as the size range of the copepods examined. If one sampling device were more selective than the other, then the results obtained by sampling a random population with the two devices would, on an average, be consistently different. For example, if *Calanus* were randomly distributed and if the pump were more selective for this species than the tow net, then the pump, on an average, would outfish the tow net by a factor directly related to the selectivity. The wide variations in the counts of copepods, with the possible exception of *Aetidius*, provide favorable evidence against gear selectivity. For hauls 5, 39, and 48 the pump markedly outfished the net for *Calanus*, whereas the exact opposite happened in hauls 14 and 19; for the remaining three pairs of hauls which were examined, the pump and tow net yielded similar values. For *Acartia*, the pump outfished the tow net in hauls 5, 14, 22, 39, 43, and 48, the reverse holding true for only haul 19; similar counts were obtained for haul 44. For *Corycaeus*, where the widest discrepancies occurred, the pump outfished the tow net by a factor greater than 1000 in haul 5; however, similar counts for this species were obtained in haul 14.

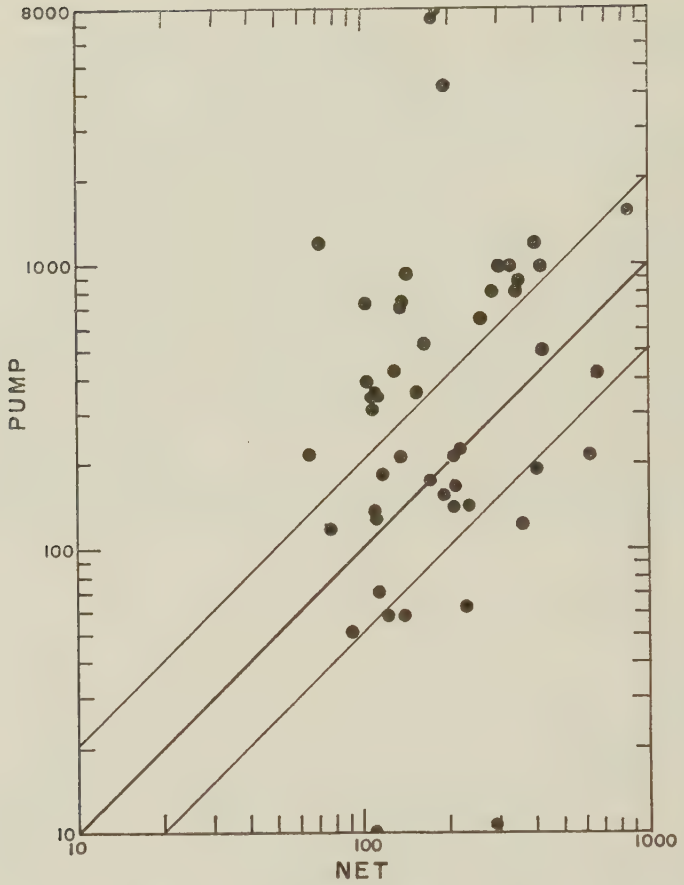

Figure 5. Catch of copepods/100 m³ of water.

Although the data show that, on an average, the pump caught more copepods per unit volume of water than the tow net, the pump is not sufficiently more efficient than the tow net to account for the wide variations which occur in a paired haul.

Another explanation for the large differences is plankton patchiness. It is assumed that such patches would occur on a small scale, much like swarms of aerial insects. Thus plankton of a particular species or group of species would occur in relatively dense concentrations in an area too small to be encountered by both sampling devices, and naturally the gear passing through such a patch would provide the higher catch; hence the counts would vary considerably in each paired haul.

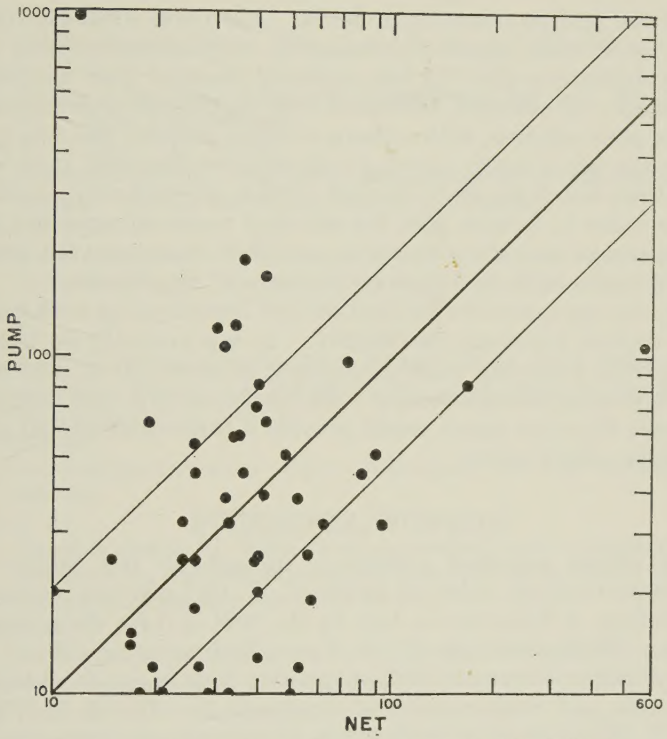

Figure 6. Catch of motile organisms minus copepods/100 m³ of water.

However, for many paired hauls there should be no trend of one net outfishing the other, but if there were such a trend it would indicate that the sampling devices are selective.

The Chi-square values for the hypothesis that the tow net and pump fish equally well (one device outfishing the other 50% of the time) are 1.28 when applied to counts of the fish eggs; 0.08 when applied to counts of motile organisms minus copepods; and 5.12 for copepod counts. If the hypothesis is true, Chi square (with one degree of freedom) has only a 5% chance of being greater than 3.84. It is probable, therefore, that the pump and tow net fish with about equal efficiency for fish eggs and total motile organisms minus copepods whereas the pump outfishes the tow net for copepods.

The wide variations obtained in counts of specific copepods are probably related to a highly nonuniform distribution of these species—in other words, plankton patchiness.

The concept of plankton patchiness is important, particularly in a

study of the feeding behavior of fishes. Allen and Aron (1957) have shown that in some salmon stomachs the contents were highly stratified, thus indicating that the fish suddenly changed their food supply. One stomach, for example, contained both amphipods and euphausiids in almost pure cultures, with a sharp division between the two groups. Possibly the fish actually selected individual euphausiids from among the plankton and then, after a period of time, selected only amphipods. But it is easier to believe that the stomach contents represent actual pure cultures as they occur in nature and that the salmon fed first on a swarm of euphausiids and then on a swarm of amphipods.

The pump appears to be an ideal tool for investigating both horizontal and vertical plankton distribution. It can probably be used successfully from a moving vessel to a depth of about 20 m; and several pumps, operating simultaneously with intakes at different depths and at different distances apart, could provide a three-dimensional picture of plankton distribution.

ACKNOWLEDGMENTS

Many people provided assistance throughout this study. The author is particularly indebted to Dr. A. C. DeLacy and his students in the College of Fisheries for help in the field and for their counts of fish eggs. Phillip Seelinger (U. S. Navy Hydrographic Office), Peter McCrery, Robert Owen and Rene Cuzon du Rest assisted in identifications, counts, and measurements of the copepods. Drs. R. H. Fleming and R. G. Paquette gave advice and encouragement throughout the study and, with Dr. A. C. DeLacy, kindly provided criticisms of the original manuscript.

REFERENCES

Allen, G. H. and William Aron
1957. Food of salmonid fishes of the western North Pacific Ocean. Spec. Sci. Rep. U. S. Fish Wildl. Serv., Fish. No. 237, 11 pp.

Bachmann, Hans
1900. Die Planktonfange mittels der Pumpe. Biol. Zentralbl., *20* (11): 386–400.

Barnes, Harold
1949. On the volume measurement of water filtered by a plankton pump, with some observations on the distribution of planktonic animals. J. Mar. biol. Ass. U. K., *28:* 651–662.

Cleve, P. T.
1896. Microscopic marine organisms in the service of hydrography. Nature, London, *55:* 89–90.

Collier, A. C.
1957. Gulf II semiautomatic plankton sampler for inboard use. Spec. Sci. Rep. U. S. Fish Wildl. Serv., Fish. No. 199, 11 pp.

FORDYCE, CHARLES
1898. A new plankton pump. Proc. Neb. hist. Soc., *2:* 293–296.
FROLANDER, H. F.
1955. Biology of the zooplankton of the Narragansett Bay area. Brown Univ., Ph.D. thesis (unpublished).
GIBBONS, S. G. AND J. H. FRASER
1937. The centrifugal pump and suction hose as a method of collecting plankton samples. J. Cons. int. Explor. Mer, *12* (2): 155–169.
GIESBRECHT, WILHELM
1896. Ueber pelagische Copepoden des Rothen Meeres, gesammelt von Marinestabarzt Dr. Augustin Kramer. Zool. Jb., Syst. *9:* 315–328, Taf. 5, 6.
HENSEN, VICTOR
1887. Ueber die Bestimmung des Planktons, oder des im Meere treibenden Materials and Pflanzen und Thieren. V. Ber. Komm. Wiss. Untersuch. dtsch. Meere Kiel, *12–14:* 1–107.
JUDAY, CHANCEY
1916. Limnological apparatus. Papers Wisc. Acad. Sci. Arts Letters, *18* (2): 566–592.
KOFOID, C. A.
1897. Plankton studies. I. Methods and apparatus in use in plankton investigations at the biological experimental station of the University of Illinois. Bull. Ill. Lab. nat. Hist., *5* (1): 1–25.
KOKUBO, SEIJI
1933. A plankton pump in which the winding of the tow line of suction tubing is made automatically. Bull. Jap. Soc. sci. Fish., *1* (6): 277–280.
KOKUBO, SEIJI AND TADASHI TAMURA
1931. A quantitative investigation of the plankton of Aomori Bay as studied comparatively by pump and net collection. Sendai. Sci. Rep. Tohoku Univ., Biol. *6* (3): 491–531.
LANGFORD, R. R.
1953. Methods of plankton collection and a description of a new sampler. J. Fish. Res. Bd. Canad., *10* (5): 238–252.
PECK, J. I.
1896. The sources of marine food. Bull. U. S. Fish Comm., *15:* 351–368.
ROBERT, HENRI
1922. L'emploi du filet et de la pompe dans les peches de plancton. Ann. Biol. lacust., *11* (1): 208–239.
TESTER, A. L. AND J. C. STEVENSON
1949. Results of the west coast of Vancouver Island Herring investigation, 1947–48. British Columbia Dep. Fish., 45 pp.
TONOLLI, VITTORIO
1951. A new device for continuous quantitative plankton sampling: the plankton bar. Proc. int. Ass. theor. appl. Limnol., *11:* 422–429.
WIBORG, K. F.
1948. Experiments with the Clarke-Bumpus plankton sampler and with a plankton pump in the Lofoten area in northern Norway. Fisk. Skrift., *9* (2), 32 pp.